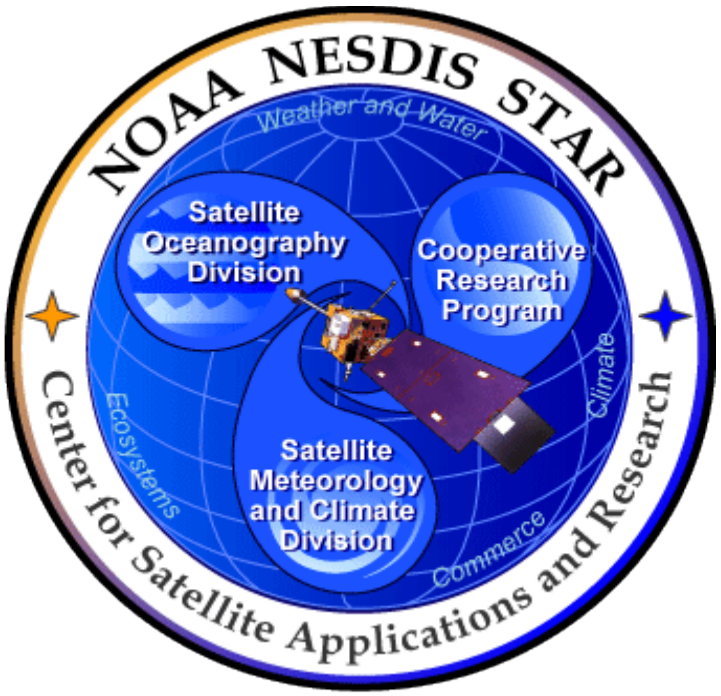

NOAA NESDIS
CENTER FOR SATELLITE APPLICATIONS AND RESEARCH

Visible Infrared Imaging Radiometer Suite (VIIRS) Ocean Color Products

ALGORITHM THEORETICAL BASIS DOCUMENT

Version 1.0

THE VIIRS OCEAN COLOR PRODUCT ALGORITHM THEORETICAL BASIS DOCUMENT VERSION 1.0

AUTHORS:

Menghua Wang (NOAA/NESDIS/STAR)

Xiaoming Liu (NOAA/NESDIS/STAR and CIRA/CSU)

Lide Jiang (NOAA/NESDIS/STAR and CIRA/CSU)

SeungHyun Son (NOAA/NESDIS/STAR and CIRA/CSU)

THE VIIRS OCEAN COLOR PRODUCT ALGORITHM THEORETICAL BASIS DOCUMENT
VERSION HISTORY SUMMARY

Version	**Description**	**Revised Sections**	**Date**
1.0	New Document for VIIRS-OC	New Document	6/5/2017

TABLE OF CONTENTS

LIST OF FIGURES

Page

LIST OF TABLES

Page

LIST OF ACRONYMS

AERONET	Aerosol Robotic Network
AERONET-OC	Aerosol Robotic Network-Ocean Color
AOT	Aerosol Optical Thickness
ATBD	Algorithm Theoretical Basis Document
BMW	Bailey-MUMM-Wang
Cal/Val	Calibration/Validation
CDOM	Colored Dissolved Organic Matter
CF	Climate and Forecast
CI	Color Index
COMS	Communication, Ocean, and Meteorological Satellite
CZCS	Coastal Zone Color Scanner
EDR	Environmental Data Records
EOS	Earth Observing System
GFS	Global Forecast System
GOCI	Geostationary Ocean Color Imager
HAB	Harmful Algal Bloom
HDF	Hierarchical Data Format
HYCOM	Hybrid Coordinate Ocean Model
IDPS	Interface Data Processing System
IOCCG	International Ocean-Colour Coordinating Group
IOP	Inherent Optical Property
JPSS	Joint Polar Satellite System
LUT	Lookup Table
MERIS	Medium Resolution Imaging Spectrometer
MICOM	Miami Isopycnic-Coordinate Ocean Model
MOBY	Marine Optical Buoy
MODIS	Moderate Resolution Imaging Spectroradiometer
MSL12	Multi-Sensor Level-1 to Level-2
MSE	Multiple Scattering Epsilon
MUMM	Management Unit of the North Sea Mathematical Models
NASA	National Aeronautics and Space Administration
NCDC	National Climate Data Center
NESDIS	National Environmental Satellite, Data, and Information Service
NGDC	National Geographic Data Center
NIR	Near-Infrared
NOAA	National Oceanic and Atmospheric Administration
NOCCG	NOAA Ocean Color Coordinating Group
NOS	National Ocean Service
NRT	Near-Real-Time

OBPG	Ocean Biology Processing Group
OC	Ocean Color
OC3V	Ocean Chlorophyll 3-band algorithm for VIIRS
OCI	Ocean Color Index
OMAO	Office of Marine and Air Operations
OSPO	Office of Satellite and Product Operations
PAR	Photosynthetically Available Radiation
PSDI	Product System Development and Implementation
QAA	Quasi-Analytical Algorithm
RDR	Raw Data Records
SeaWiFS	Sea-viewing Wide Field-of-view Sensor
SDR	Sensor Data Records
SeaBASS	SeaWiFS Bio-optical Archive and Storage System
SeaDAS	SeaWiFS Data Analysis System
SNPP	Suomi National Polar-orbiting Partnership
SNR	Signal to Noise Ratio
SSE	Single Scattering Epsilon
STAR	Center for Satellite Applications and Research
STD	Standard Deviation
SWIR	Shortwave Infrared
TOA	Top of Atmosphere
UV	Ultraviolet
VIIRS	Visible Infrared Imaging Radiometer Suite

ABSTRACT

The Ocean Color Team at NOAA Center for Satellite Applications and Research (STAR) has developed the Multi-Sensor Level-1 to Level-2 (MSL12) software package for processing the Visible Infrared Imaging Radiometer Suite (VIIRS) ocean color (OC) Environmental Data Records (EDR or Level-2 data) from Sensor Data Records (SDR or Level-1B data). This document provides the Algorithm Theoretical Basis Document (ATBD) for the algorithms implemented in MSL12 for VIIRS ocean color data processing. The VIIRS ocean color processing algorithms include atmospheric correction algorithm and a suite of algorithms to generate ocean biological and biogeochemical products, such as chlorophyll-a (Chl-a) concentration, the diffuse attenuation coefficient at the wavelength of 490 nm (K_d(490)), and the diffuse attenuation coefficient at the domain associated with the photosynthetically available radiation (PAR) (K_d(PAR)). The main function of the atmospheric correction is to derive the normalized water-leaving radiance spectra $nL_w(\lambda)$ by removing the atmospheric and ocean surface effects from the satellite sensor-measured top-of-atmosphere (TOA) radiances. Since VIIRS has similar spectral bands as the Moderate Resolution Imaging Spectroradiometer (MODIS), both the near-infrared (NIR)- and shortwave infrared (SWIR)-based atmospheric correction algorithms, which have been developed and used for MODIS ocean color data processing, can be directly applied to VIIRS. In addition, there have been some significant algorithms improvements in MSL12 for VIIRS ocean color data processing. Some experimental ocean color products, such as inherent optical properties (IOPs), ocean color index (OCI)-based Chl-a concentration for oligotrophic waters, etc., have also been implemented in MSL12 for evaluation. VIIRS global ocean color products have been routinely produced using the MSL12 with the NIR- and SWIR-based ocean color data processing approaches. Data quality from VIIRS ocean color products are routinely monitored and validated using in situ measurements from the Marine Optical Buoy (MOBY) in waters off Hawaii, various AERONET-OC stations, and from dedicated VIIRS ocean color calibration and validation (Cal/Val) cruises, as well as from in situ data collected in various opportunities.

It is noted that this ATBD will be updated continuously as ocean color data processing algorithms will be improved continuously and new ocean color products will be added into the VIIRS ocean color data product suite as requested from users and scientific research community.

1. INTRODUCTION

Ocean color is the water hue (water-leaving radiance spectra) due to the presence of tiny plants and particles containing the pigment chlorophyll, sediments, and colored dissolved organic matter (CDOM). Ocean color satellite remote sensing was started with the Coastal Zone Color Scanner (CZCS) (*Gordon et al.*, 1980; *Hovis et al.*, 1980) as a proof-of-concept mission in which it demonstrated the feasibility of quantitative retrieval of ocean near-surface optical and biological data. After the CZCS mission, a number of follow-on satellite instruments that are capable of global ocean color measurements have been launched. Particularly, with the successful flight of the Sea-viewing Wide Field-of-view Sensor (SeaWiFS) (*Hooker et al.*, 1992; *McClain et al.*, 2004) (1997–2010), the Moderate Resolution Imaging Spectroradiometer (MODIS) (*Esaias et al.*, 1998; *Salomonson et al.*, 1989) on the Earth Observing System (EOS) Terra (1999–present) and Aqua (2002–present), and the Medium Resolution Imaging Spectrometer (MERIS) (*Rast et al.*, 1999) on the Envisat (2002–2012), the global ocean color data have been used by researchers and scientists worldwide to study and understand ocean physical, optical, biological, and biogeochemical changes and their effects on the climate (*Behrenfeld et al.*, 2006; *Behrenfeld et al.*, 2001; *Chavez et al.*, 1999; *Siegel et al.*, 2002). The Visible Infrared Imaging Radiometer Suite (VIIRS) (*Goldberg et al.*, 2013) onboard the Suomi National Polar-orbiting Partnership (SNPP), which was successfully launched on October 28, 2011, is now continuing to provide global ocean color products (*Wang et al.*, 2013b), with the second VIIRS from the Joint Polar Satellite System (JPSS) platform (JPSS-1) to follow in 2017 and third VIIRS (JPSS-2) several years later after JPSS-1. Table 1 provides characteristics of the ocean color spectral bands for VIIRS-SNPP, VIIRS-JPSS-1, and MODIS. In addition, spectral bands that are designed for the atmosphere and land applications, e.g., the shortwave infrared (SWIR) bands and high spatial resolution image bands (I-band), which can also be useful for the ocean color application in the coastal and inland water regions, are also listed in Table 1 (for both MODIS and VIIRS). Table 1 shows that VIIRS and MODIS have similar ocean color and SWIR spectral bands. Therefore, algorithms developed in MODIS can generally be applied also to VIIRS. It is noted that VIIRS spectral bands are indicated in the nominal center wavelengths.

Satellite ocean color products are important for ocean environment monitoring and forecast. For examples, chlorophyll-a (Chl-a) concentration (*O'Reilly et al.*, 1998) provides an estimate of the live phytoplankton biomass in the ocean surface layer, and the water diffuse attenuation coefficient at the wavelength of 490 nm (K_d(490)) or at the domain associated with the photosynthetically available radiation (PAR) (K_d(PAR)) (*Lee et al.*, 2002; *Morel et al.*, 2007; *Mueller*, 2000; *Son and Wang*, 2015; *Wang et al.*, 2009a) indicates the turbidity of the water column. K_d(490) and K_d(PAR) are important water property data related to light penetration and availability in aquatic systems. Accurate estimation of the water diffuse attenuation coefficient is critical to understand not only physical processes such as the heat transfer in the upper layer of the ocean (*Lewis et al.*, 1990; *Morel and Antoine*, 1994; *Sathyendranath et al.*, 1991; *Wu et al.*, 2007), but also biological processes such as phytoplankton photosynthesis in the ocean euphotic zone (*Platt et al.*, 1988; *Sathyendranath et al.*, 1989). It is noted that these ocean biological and biogeochemical parameters are all derived from satellite-measured normalized water-leaving

TABLE 1. The ocean color and other useful spectral bands for VIIRS and MODIS.

VIIRS (JPSS-1)		VIIRS (SNPP)		MODIS	
Ocean Bands (nm)	Other Bands (nm)	Ocean Bands (nm)	Other Bands (nm)	Ocean Bands (nm)	Other Bands (nm)
411 (M1)	642 (I1)	410 (M1)	638 (I1)	412	645
445 (M2)	867 (I2)	443 (M2)	862 (I2)	443	859
489 (M3)	1603 (I3)	486 (M3)	1600 (I3)	488	469
—		—		531	555
556 (M4)	*SWIR Bands*	551 (M4)	*SWIR Bands*	551	*SWIR Bands*
667 (M5)	1238 (M8)	671 (M5)	1238 (M8)	667	1240
746 (M6)	1604 (M10)	745 (M6)	1601 (M10)	748	1640
868 (M7)	2258 (M11)	862 (M7)	2257 (M11)	869	2130

radiance spectra $nL_w(\lambda)$ (*Gordon*, 2005; *Gordon and Wang*, 1994a; *IOCCG*, 2010; *Morel and Gentili*, 1996; *Wang*, 2006a).

1.1. Purpose

The NOAA Multi-Sensor Level-1 to Level-2 (MSL12) ocean color data processing system has been developed by *Wang and co-workers* of the Ocean Color Team at NOAA Center for Satellite Applications and Research (STAR) for producing VIIRS global ocean color products (*Wang, et al.*, 2013b). MSL12 was developed for the purpose of using a consistent and common data processing system to produce global ocean color products from multiple satellite ocean color sensors, i.e., common algorithms in the data processing for all satellite ocean color sensors (*Wang*, 1999a; *Wang and Franz*, 2000; *Wang et al.*, 2002). In other words, MSL12 is measurement-based (not mission-based) ocean color data processing system. Specifically, NOAA-MSL12 is based on the SeaWiFS Data Analysis System (SeaDAS) version 4.6 with some important modifications and improvements. The improved MSL12 has been used to extensively process ocean color data from MODIS-Aqua (*Wang et al.*, 2009b), VIIRS-SNPP (*Wang et al.*, 2016a; *Wang et al.*, 2014; 2015a; *Wang, et al.*, 2013b), and the Korean Geostationary Ocean Color Imager (GOCI) (*Wang et al.*, 2013a). In fact, since July 2012, MSL12 has been the NOAA operational system to routinely produce MODIS-Aqua ocean color products over the U.S. coastal and some open ocean regions (*Wang and Liu*, 2012). The MSL12 is the official NOAA VIIRS ocean color data processing system. In VIIRS ocean color data processing, VIIRS Sensor Data Records (SDR or Level-1B data) are processed to produce ocean color Environmental Data Records (EDR or Level-2 data).

There are mainly two stages in the satellite ocean color data processing from the SDR to EDR: (1) applying the atmospheric correction algorithm to generate normalized water-leaving radiance spectra $nL_w(\lambda)$ and (2) generate a suite of ocean color products, i.e., biological and biogeochemical parameters, such as Chl-a, $K_d(490)$, $K_d(\text{PAR})$, IOPs, etc., using $nL_w(\lambda)$ spectra data obtained in the first stage.

Atmospheric correction algorithm is a key procedure in the satellite ocean color data processing. The main function of the atmospheric correction is to retrieve the normalized water-leaving radiance spectra $nL_w(\lambda)$ from the satellite-measured TOA radiances by removing the atmospheric and ocean surface effects (*Antoine and Morel*, 1999; *Fukushima et al.*, 1998; *Gordon and Wang*, 1994a; *IOCCG*, 2010; *Wang*, 2007). There are two types of atmospheric correction algorithms used in the ocean color data processing in MSL12. In the *Gordon and Wang* (1994a) algorithm, the aerosol reflectance is estimated using the two VIIRS NIR bands at 745 and 862 nm with the assumption of the black ocean at these two NIR wavelengths. The NIR black ocean assumption is usually valid at the open ocean with generally low Chl-a concentration. However, for highly productive ocean waters and turbid coastal and inland waters, the ocean/water contributions in the NIR bands are no longer negligible and can be very significant (*Shi and Wang*, 2009; *Wang and Shi*, 2005; *Wang et al.*, 2007). In these cases, atmospheric correction often results in significant errors (*Lavender et al.*, 2005; *Ruddick et al.*, 2000; *Siegel et al.*, 2000; *Wang and Shi*, 2005). In fact, some modifications have been made to account for the NIR ocean radiance contributions for non-highly turbid waters (*Bailey et al.*, 2010; *Stumpf et al.*, 2003; *Wang et al.*, 2012). Recently, an improved NIR water-leaving reflection correction algorithm has been developed and implemented in MSL12 for VIIRS ocean color data processing (*Jiang and Wang*, 2014).

As an alternative approach for dealing with turbid waters in coastal and inland water regions, *Wang* (2007) proposed an atmospheric correction algorithm using the SWIR bands, which can be used for both MODIS and VIIRS. At the SWIR wavelengths, ocean water has much stronger absorption than that at the NIR bands (*Hale and Querry*, 1973; *Kou et al.*, 1993). Thus, the black ocean assumption is generally valid at the SWIR bands even for highly turbid waters (*Shi and Wang*, 2009). Furthermore, to address the noise issue for the SWIR bands (*Wang*, 2007; *Wang and Shi*, 2012; *Werdell et al.*, 2010), *Wang and Shi* (2007) proposed a method for ocean color data processing using the combined NIR and SWIR bands for atmospheric correction for global open oceans and turbid coastal and inland waters. With the proposed NIR-SWIR combined atmospheric correction algorithm, satellite ocean color data can be processed using the standard-NIR atmospheric correction for the open ocean, whereas for turbid coastal and inland waters the SWIR-based atmospheric correction algorithm can be executed (*Wang and Shi*, 2007). The NIR-, SWIR-, and NIR-SWIR-combined atmospheric correction algorithms have been implemented in MSL12 and routinely used to produce VIIRS ocean color products (*Wang, et al.*, 2016a; *Wang, et al.*, 2014; 2015a; *Wang, et al.*, 2013b).

The algorithm for calculating ocean Chl-a concentration (*O'Reilly, et al.*, 1998; *O'Reilly et al.*, 2000) using the empirical blue-green reflectance ratio approach from the normalized water-leaving radiance spectra $nL_w(\lambda)$ has been adjusted for VIIRS spectral bands. In addition, the algorithms for the ocean color product K_d(490) (*Wang, et al.*, 2009a), K_d(PAR) (*Son and Wang*, 2015), IOPs from the quasi-analytical algorithm (QAA) (*Lee, et al.*, 2002), and Chl-a from the ocean color index (OCI) method (*Hu et al.*, 2012; *Wang and Son*, 2016) have been implemented in MSL12 for VIIRS global ocean color data processing.

1.2. Scope

This document describes the algorithms implemented in MSL12, which are used to process and produce VIIRS ocean color data from SDR to EDR. MSL12 is an official NOAA VIIRS ocean color data processing system and has been used for routinely producing VIIRS global ocean color products (including global daily, 8-day, monthly, and climatology images) since VIIRS-SNPP launch in October 2011. NOAA/STAR has been focusing on the "end-to-end" production of high quality satellite ocean color products, and has put considerable efforts into sensor calibration by re-examining and fixing errors in the current calibration methods, in particular, adding the effect of lunar calibration, i.e., used both solar and lunar calibration approaches for VIIRS (*Sun and Wang*, 2014; 2015a; b; c; 2016). With the improved sensor calibration, the science quality SDR data have been routinely processed from the Raw Data Records (RDR or Level-0 data) using an efficient data processing method (*Sun et al.*, 2014). In addtion, vicarous calibration for the ocean color data processing system is necessary (*Eplee Jr. et al.*, 2001; *Franz et al.*, 2007; *Gordon*, 1998; *Wang and Gordon*, 2002; *Wang et al.*, 2016c). We have developed a consistent vicarious calibration approach using the Marine Optical Buoy (MOBY) (*Clark et al.*, 1997) in situ data in waters off Hawaii for both the NIR- and SWIR-based atmospheric correction algorithms (*Wang, et al.*, 2016c). In fact, the derived vicarious gains have been applied to VIIRS for routine ocean color data processing using both the NIR- and SWIR-based atmospheric correction algorithms (*Wang, et al.*, 2016c). Furthermore, the vicarous calibration method can also be used to routinely monitor VIIRS sensor performance (*Wang et al.*, 2015b). However, since this document only describes the algorithms used for processing VIIRS data from SDR to ocean color EDR, the algorithms for VIIRS on-orbit sensor calibration and system vicarious calibration are not described because they are out-of-scope of this document.

2. ALGORITHM DESCRIPTION

2.1. Data Processing Outline

The VIIRS ocean color data processing system (MSL12) processes daily global SDR to ocean color EDR data. Specifically, the data processing procedure includes the following steps:

Step 1: Read the input parameter file, SDR file, geolocation file, ancillary data, and required lookup tables (LUTs).
Step 2: Identify clear sky scene (pixels) over waters using the SWIR-based (VIIRS-SNPP SWIR 1238 nm band) cloud masking method (*Wang and Shi*, 2006). All clear pixels over waters will go to the next step; otherwise the data processing is stopped (for cloud or land pixels).
Step 3: Make corrections of ozone and water vapor absorptions to the sensor-measured TOA radiances (SDR). Calculate ozone, water vapor, and polarization corrections.
Step 4: Compute Rayleigh scattering radiances, whitecap radiances, and sun glint masking and correction (if it is needed).
Step 5: Remove Rayleigh radiance contributions, i.e., compute Rayleigh-corrected radiances.
Step 6: Calculate the spectral aerosol radiance contributions using the NIR or SWIR bands.
Step 7: Compute atmospheric diffuse transmittances for solar- and sensor-zenith angles.
Step 8: Remove aerosol spectral radiance contributions to derive normalized water-leaving radiance spectra $nL_w(\lambda)$.
Step 9: Calculate the required ocean color products, including $nL_w(\lambda)$, Chl-a, K_d(490), and K_d(PAR), as well as various experimental products such as IOPs, etc.
Step 10: Write out the ocean color product data into the EDR output file.

2.2. Algorithm Inputs

2.2.1. VIIRS Data

The ocean color data processing takes calibrated TOA radiances at the following wavelengths in the VIIRS SDR files: 410 (M1), 443 (M2), 486 (M3), 551 (M4), 671 (M5), 745 (M6), 862 (M7), 1238 (M8), 1601 (M10), and 2257 nm (M11). In addition, the algorithm also needs the geolocation information such as solar-zenith angle, sensor-zenith angle, and relative azimuth angle, as well as latitude and longitude from the geolocation file.

2.2.2. Ancillary Data

The VIIRS ocean color data processing also takes the following ancillary data as inputs (*Ramachandran and Wang*, 2011):
(a) Ozone concentration: the input is required for the correction of ozone absorption in the sensor-measured TOA radiances.
(b) Surface atmosphere pressure: the input is required to compute the spectral Rayleigh radiances.
(c) Surface wind speed: the input is required to calculate the spectral Rayleigh radiances, whitecap radiances, and sun glint radiance contributions.

(d) Water vapor amount: the input is required for the correction of water vapor absorption in the sensor-measured radiances at the NIR and SWIR bands.

2.2.3. Other Data

Some static (non-dynamic) input data include: various LUTs such as Rayleigh radiance LUTs, aerosol radiance LUTs, atmospheric diffuse transmittance LUTs, and polarization LUTs, as well as solar irradiance, water optical property spectra, and various IOP spectra, etc; climatology data such as $nL_w(551)$, aerosol optical thickness at 865 nm $\tau_a(865)$, aerosol angstrom exponent at 510 nm Å(510), and nitrogen dioxide NO_2 distribution, etc; mask data such as 250 m land mask, 1 km water mask, and 9 km ice mask; and sensor-specific spectral band-averaged data.

2.3. Theoretical descriptions of atmospheric correction algorithms

In this section, we describe the classic NIR-based atmospheric correction algorithm in Section 2.3.1, and the SWIR-based algorithm proposed by *Wang* (2007) in Section 2.3.2. The NIR-SWIR-based algorithm developed by *Wang and Shi* (2007) is described in Section 2.3.3. Some algorithm improvements in MSL12 such as improved Rayleigh radiance computations (*Wang*, 2016), an improved NIR ocean reflectance correction algorithm (*Jiang and Wang*, 2014), the improved stray light and cloud shadow identification algorithm (*Jiang and Wang*, 2013), and destriping algorithm (*Mikelsons et al.*, 2014) are described in Section 2.3.4. It is noted that VIIRS global ocean color products processed using the NIR-, SWIR-, and NIR-SWIR-based atmospheric correction algorithms have been routinely produced now.

2.3.1. The NIR-based atmospheric correction algorithm

In this document, we define the reflectance $\rho(\lambda)$, at a given wavelength λ and for a specific solar-zenith angle of θ_0, to be related to the radiance $L(\lambda)$ through

$$\rho(\lambda) = \frac{\pi L(\lambda)}{\cos\theta_0 F_0(\lambda)}, \tag{1}$$

where $F_0(\lambda)$ is the extraterrestrial solar irradiance (*Thuillier et al.*, 2003). Thus, the radiance and reflectance are interchangeable based on the definition in Eq. (1). For the ocean-atmosphere system, the TOA reflectance $\rho_t(\lambda)$ (or radiance $L_t(\lambda)$ can be linearly partitioned into various distinct physical contributions (*Gordon and Wang*, 1994a):

$$\rho_t(\lambda) = \rho_r(\lambda) + \rho_A(\lambda) + t(\lambda)\rho_{wc}(\lambda) + T(\lambda)\rho_g(\lambda) + t(\lambda)t_0(\lambda)\rho_{wN}(\lambda), \text{ or}$$
$$L_t(\lambda) = L_r(\lambda) + L_A(\lambda) + t(\lambda)L_{wc}(\lambda) + T(\lambda)L_g(\lambda) + t(\lambda)t_0(\lambda)\cos\theta_0 nL_w(\lambda), \tag{2}$$

where $\rho_r(\lambda)$ and $\rho_A(\lambda)$ (or $L_r(\lambda)$ and $L_A(\lambda)$) are, respectively, the reflectance (or radiance) due to multiple scattering by air molecules (Rayleigh scattering) (*Gordon et al.*, 1988a; *Gordon and Wang*, 1992; *Wang*, 2002; 2005; 2016) and aerosols (including Rayleigh-aerosol interactions) (*Deschamps et al.*, 1983; *Gordon and Wang*, 1994a; *Wang*, 1991), respectively. $\rho_{wc}(\lambda)$ and $\rho_g(\lambda)$ (or $L_{wc}(\lambda)$ and $L_g(\lambda)$) are the components of reflectance (or radiance) due to whitecaps on the sea

surface (*Frouin et al.*, 1996; *Gordon and Wang*, 1994b; *Moore et al.*, 2000) and the specular reflection of direct sunlight off the sea surface (sun glitter) (*Wang and Bailey*, 2001; *Zhang and Wang*, 2010), respectively, and $\rho_{wN}(\lambda)$ (or $nL_w(\lambda)$) is the normalized water-leaving reflectance (or radiance) due to photons that penetrate the sea surface and are backscattered out of the water, which is the desired quantity in the ocean color remote sensing. The quantities $t_0(\lambda)$ and $t(\lambda)$ are the atmospheric diffuse transmittances from the sun to the water surface and from the water surface to the sensor (*Wang*, 1999b; *Yang and Gordon*, 1997), respectively. $T(\lambda)$ is the direct transmittance from the water surface to the sensor (*Wang and Bailey*, 2001). The objective of the atmospheric correction is to retrieve the normalized water-leaving reflectance $\rho_{wN}(\lambda)$ (or normalized water-leaving radiance $nL_w(\lambda)$) accurately from the sensor-measured reflectance spectra $\rho_t(\lambda)$ (or radiance spectra $L_t(\lambda)$).

As it is shown, Eq. (2) applies to both reflectance and radiance (note an extra factor of $\cos\theta_0$ in the radiance equation in the last term). It should be noted that Eq. (2) is valid when the target is large spatially, i.e., effects of the target environment within the measurement pixel can be neglected. The relationship between normalized water-leaving reflectance $\rho_{wN}(\lambda)$ and normalized water-leaving radiance $nL_w(\lambda)$ is given by:

$$\rho_{wN}(\lambda) = \pi\, nL_w(\lambda)/F_0(\lambda). \tag{3}$$

It is also common to use the remote-sensing reflectance $R_{rs}(\lambda)$, which can be related to $nL_w(\lambda)$ and $\rho_{wN}(\lambda)$ as:

$$R_{rs}(\lambda) = nL_w(\lambda)/F_0(\lambda) = \rho_{wN}(\lambda)/\pi. \tag{4}$$

We can further define the atmospheric path reflectance $\rho_{path}(\lambda)$ (or radiance $L_{path}(\lambda)$), which is originated along the optical path from scattering in the atmosphere and from specular reflection of scattered light (skylight) by the sea surface, and it can be decomposed into two components as

$$\rho_{path}(\lambda) = \rho_r(\lambda) + \rho_A(\lambda) \text{ or}$$
$$L_{path}(\lambda) = L_r(\lambda) + L_A(\lambda) \tag{5}$$

and then Eq. (2) becomes

$$\rho_t(\lambda) = \rho_{path}(\lambda) + t(\lambda)\rho_{wc}(\lambda) + T(\lambda)\rho_g(\lambda) + t(\lambda)t_0(\lambda)\rho_{wN}(\lambda), \text{ or}$$
$$L_t(\lambda) = L_{path}(\lambda) + t(\lambda)L_{wc}(\lambda) + T(\lambda)L_g(\lambda) + t(\lambda)t_0(\lambda)\cos\theta_0 nL_w(\lambda). \tag{6}$$

From now on, we will use either reflectance or radiance in descriptions and discussions with understanding that these two are interchangeable based on their definitions (Eqs. (1)–(6)).

Again, the purpose of atmosphere correction is to derive normalized water-leaving radiance $nL_w(\lambda)$ from the total radiance measured at the satellite sensor, i.e., retrieving $nL_w(\lambda)$ from sensor-measured $L_t(\lambda)$ in Eq. (6). However, the radiance backscattered from the atmosphere and/or sea surface is typically an order of magnitude larger than the desired radiance scattered out of the water (*IOCCG*, 2010). The principal difficulty and challenge in atmospheric correction

is the estimation and removal of $L_{path}(\lambda)$ from $L_t(\lambda)$. In other words, we have to compute $L_{path}(\lambda)$ accurately. In Case-1 waters, $L_{path}(\lambda)$ contributes about 90% of the TOA radiance in the blue and a higher fraction in the green and red. Removing a large signal and deriving a very small signal accurately from the water is a major challenge of the atmospheric correction over the ocean (*Gordon and Wang*, 1994a; *IOCCG*, 2010; *Wang*, 2007).

Removing the sun glint (*Wang and Bailey*, 2001) and whitecap (*Gordon and Wang*, 1994b) reflectance contributions from the TOA reflectance is straightforward. Sun glint is originated from specular reflection of direct sunlight by the sea surface (sun glitter) (*Cox and Munk*, 1954; *Zhang and Wang*, 2010). Significant sun glint reflectance contributions with certain viewing geometries are mostly masked out, and the residual glint contamination is corrected based on a model of sea surface slope distribution using the input of sea surface wind speed (*Cox and Munk*, 1954; *Wang and Bailey*, 2001). Ocean whitecap (foam) reflectance is originated from reflection of direct sunlight and skylight from ocean whitecaps. The whitecap reflectance contribution for each band is generally small (*Moore, et al.*, 2000) and is calculated as a function of sea surface wind speed and viewing geometry (*Frouin, et al.*, 1996; *Gordon and Wang*, 1994b; *Moore, et al.*, 2000). It is noted that these algorithms have not been changed in the SWIR and NIR-SWIR atmospheric correction algorithms.

With the assumption that normalized water-leaving reflectances $\rho_{wN}(\lambda)$ are negligible in the NIR bands (745 and 862 nm for VIIRS-SNPP) in the open ocean, the aerosol reflectance, $\rho_A(\lambda)$, can be estimated by removing Rayleigh reflectance, sun glint, and whitecap reflectance from the TOA reflectance in the two NIR bands. The aerosol models are used to estimate the aerosol reflectance contributions in visible bands, through using aerosol LUTs. The aerosol LUTs were generated using the vector radiative transfer theory with including polarization effects (*Wang*, 2006b). The algorithm selects from a family of the 12 aerosol models to fit the aerosol radiance contributions in the NIR bands, and the selected two models are then used to extrapolate the aerosol radiances from the NIR to visible bands using aerosol models (*Gordon and Wang*, 1994a; *Wang*, 1999a; 2004; 2007).

The 12 aerosol models derived from the work of *Shettle and Fenn* (1979) are used in the VIIRS ocean color data processing. Specifically, they are the Oceanic model with relative humidity (RH) of 99% (O99), the Maritime models with RH of 50%, 70%, 90%, 99% (M50, M70, M90, and M99), the Coastal models with RH of 50%, 70%, 90%, 99%, (C50, C70, C90, and C99), and the Tropospheric models with RH of 50%, 90%, 99% (T50, T90, and T99) (*Gordon and Wang*, 1994a; *Shettle and Fenn*, 1979; *Wang*, 1999a). These aerosol models are used to generate aerosol LUTs for computing $\rho_A(\lambda)$. Briefly, for each aerosol model radiative transfer computations are carried out to determine $\rho_{path}(\lambda)$ as a function of the aerosol optical thickness (AOT) for a variety of solar-sensor geometries. The computations use complete vector radiative transfer, i.e., including polarization effects (*Wang*, 2006b). The appropriate $\rho_r(\lambda)$ is then subtracted from the $\rho_{path}(\lambda)$ yielding $\rho_A(\lambda)$, which is then fitted to a fourth order polynomial in the single-scattered aerosol reflectance for a given geometry (*Wang*, 2006b; 2007). The aerosol LUTs contain the fitting coefficients for a large number of solar-viewing geometries and for values of the aerosol optical thickness up to 0.8 (see details in Section 2.3.2) (*Wang*, 2007).

The procedure for estimating $\rho_A(\lambda)$ in the visible bands is to estimate this quantity in the NIR bands first, assuming negligible water-leaving reflectance in that region of the spectrum for the open oceans. Using the aerosol LUTs, the sensor-measured spectral variation of $\rho_A(\lambda)$ at the two NIR bands can be used to estimate the single-scattering aerosol reflectance $\rho_{as}(\lambda)$ (*Gordon and Wang*, 1994a; *Wang*, 2004; *Wang and Gordon*, 1994) for the same two bands. As $\rho_{as}(\lambda)$ is related directly to the aerosol inherent properties, i.e., phase function, single-scattering albedo, and aerosol extinction coefficient, it can be computed directly for each aerosol model. It is then possible to select the most appropriate aerosol models for which the computed radiances are best matched with the measured values. This is accomplished by comparing the measured value of the single scattering epsilon (SSE) with those computed for each model (*Gordon and Wang*, 1994a; *Wang*, 2004; 2007; *Wang and Gordon*, 1994). This approach is used because the SSE depends only on the aerosol model (i.e., aerosol inherent properties), and not on the aerosol optical thickness. Based on the derived SSE values in the NIR bands, the two most appropriate aerosol models (from the set of 12 models) are retrieved and used for estimation of the aerosol effects in the visible bands, i.e., $\rho_{as}(\lambda)$ and $\rho_A(\lambda)$. An alternative approach of the aerosol reflectance extrapolation using the NIR multiple-scattering epsilon (MSE) generally shows similar results, compared with those from the SSE method (*Wang*, 2004). However, there are some cases with outliers using the MSE method, in particular, for cases with maritime aerosols (generally over open oceans) (*Wang*, 2004). Therefore, the normalized water-leaving radiance (or reflectance) in the visible wavelengths can be derived. Results show that the *Shettle and Fenn* (1979) aerosol models are sufficient to derive accurate normalized water-leaving radiance (or reflectance) spectra (*Wang, et al.*, 2016a; *Wang, et al.*, 2014; 2015a; *Wang, et al.*, 2013b), compared with results from using more updated aerosol models for atmospheric correction (*Ahmad et al.*, 2010).

2.3.2. The SWIR-based atmospheric correction algorithm

In the NIR-based atmospheric correction algorithm as described in Section 2.3.1, the aerosol reflectances are calculated with assumption of the black ocean in the two NIR bands, i.e., there are no ocean radiance contributions at the NIR bands (*Gordon and Wang*, 1994a). This so called NIR black ocean assumption is usually valid at open oceans where the ocean optical properties are mainly as a function of the pigment concentration with generally low pigment concentration values. However, for highly productive ocean waters and certainly for turbid waters in coastal and inland waters (e.g., waters with high sediment concentration), water-leaving radiances in the NIR bands are no longer negligible and can even be very significant (*Lavender, et al.*, 2005; *Ruddick, et al.*, 2000; *Siegel, et al.*, 2000; *Stumpf, et al.*, 2003; *Wang and Shi*, 2005). In these cases, the NIR atmospheric correction often results in significant errors in the derived $nL_w(\lambda)$ in the visible bands. This is basically because at the NIR wavelengths water absorptions are not large enough to absorb photons backscattered out of waters by particles.

Wang (2007) proposed and evaluated a new atmospheric correction algorithm, which uses the SWIR bands to derive $nL_w(\lambda)$ spectra from the ultraviolet (UV) to the visible and NIR wavelengths. This algorithm was originally proposed for MODIS, but it also can be used for VIIRS SWIR bands as well. For wavelengths longer than the NIR band, water absorption

increases rapidly as the increase of the wavelength. Indeed, for the SWIR wavelengths (> ~1000 nm), water has much stronger absorption than that at the NIR 862 nm. Specifically, from *Hale and Querry* (1973), the water absorption coefficients for wavelengths at VIIRS 862, 1238, 1601, and 2257 nm are about 5, 89, 668, and 1714 m^{-1}, respectively. Therefore, with the black ocean assumption at the SWIR wavelengths, the SWIR bands can be used for detecting turbid waters (*Shi and Wang*, 2007), as well as for atmospheric correction in the coastal and inland water regions (*Wang*, 2007; *Wang and Shi*, 2005; 2007; *Wang, et al.*, 2009b).

Using the same 12 aerosol models as described in Section 2.3.1, the aerosol optical property data for spectral bands were generated for the SWIR wavelengths (1238, 1601, and 2257 nm) in addition to other VIIRS spectral bands at 410, 443, 486, 551, 671, 745, and 862 nm. Similar to the generation of MODIS ocean band aerosol LUTs, the aerosol LUTs for the SWIR bands were generated using the vector radiative transfer simulations (including polarization) (*Wang*, 2006b) that were carried out with the 12 aerosol models for nine aerosol optical thicknesses at 862 nm (0.02, 0.05, 0.1, 0.15, 0.2, 0.3, 0.4, 0.6, and 0.8), 33 solar-zenith angles from 0°–80° at a step of 2.5°, and 35 sensor-zenith angles from 1°–75° at a step of ~2°. The aerosol SSE parameter $\varepsilon(\lambda,\lambda_0)$ is defined as the ratio of the aerosol single-scattering reflectance $\rho_{as}(\lambda)$ between two bands, i.e.,

$$\varepsilon(\lambda,\lambda_0)=\frac{\rho_{as}(\lambda)}{\rho_{as}(\lambda_0)}=\frac{\omega_a(\lambda)c_{ext}(\lambda)p_a(\theta_0,\theta,\Delta\phi,\lambda)}{\omega_a(\lambda_0)c_{ext}(\lambda_0)p_a(\theta_0,\theta,\Delta\phi,\lambda_0)}, \tag{7}$$

where $\omega_a(\lambda)$, $c_{ext}(\lambda)$, and $p_a(\theta_0, \theta, \Delta\phi, \lambda)$ are the aerosol single-scattering albedo, aerosol extinction coefficient, and aerosol effective scattering phase function (*Gordon and Wang*, 1994a; *Wang*, 2004), respectively. The SSE depends mainly on the aerosol model (i.e., aerosol inherent properties) and can be used to characterize the aerosol spectral variation for various aerosol models.

Since VIIRS spectral bands are similar to those of MODIS, the MODIS SWIR results from *Wang* (2007) are used in the following analysis, and they are also valid for VIIRS, e.g., see results from *Wang et al.* (2013b). Figure 1 provides examples of the SSE as a function of the wavelength (from the UV to NIR or to various SWIR bands) for the 12 aerosol models. Figures 1(a)–1(d) show the SSE $\varepsilon(\lambda, \lambda_0)$ at the reference wavelengths λ_0 of 865, 1240, 1640, and 2130 nm, respectively. They are all for the case of a solar-zenith angle θ_0 of 60°, sensor-zenith angle θ of 20°, and relative-azimuth angle $\Delta\phi$ of 90°. As expected, $\varepsilon(\lambda, \lambda_0)$ value has significant variations corresponding to various reference wavelength λ_0 values. Between the O99 and the T50 models (from the lowest to the highest SSE values), Fig. 1 shows that the SSE values at the UV band for $\varepsilon(340, 865)$, $\varepsilon(340, 1240)$, $\varepsilon(340,1640)$, and $\varepsilon(340, 2130)$ are in the range of 0.8–2.6, 0.7–4.8, 0.7–9.2, and 0.7–22.6, respectively. Particularly, the NIR and SWIR SSE values of $\varepsilon(765, 865)$, $\varepsilon(1000, 1240)$, $\varepsilon(1240, 1640)$, $\varepsilon(1240, 2130)$, and $\varepsilon(1640, 2130)$, which can be used for the selection of aerosol models in atmospheric correction, are in the range of 0.96–1.21, 0.93–1.50, 0.95–1.94, 0.98–4.76, and 1.04–2.46, respectively. Obviously, there are significantly

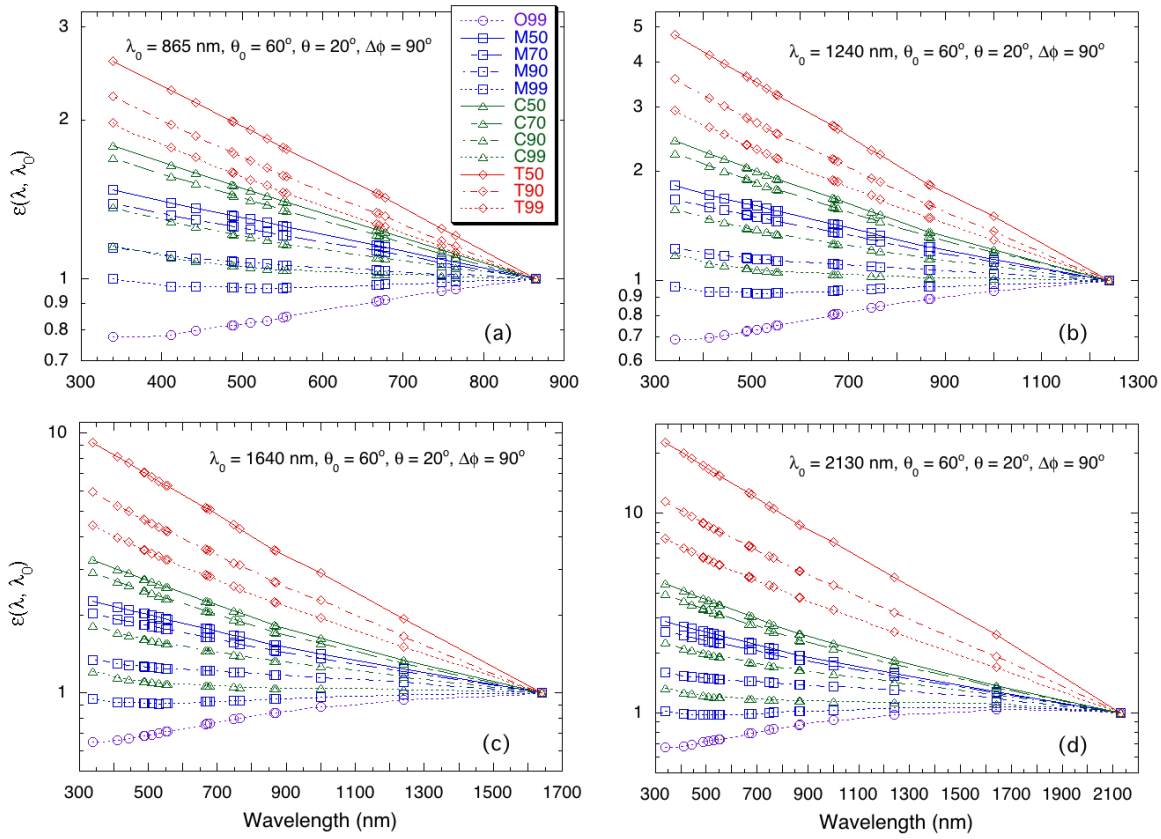

Figure 1. Single-scattering epsilon $\varepsilon(\lambda, \lambda_0)$ as a function of the wavelength λ for the 12 aerosol models and for the reference wavelength λ_0 at (a) 865 nm, (b) 1240 nm, (c) 1640 nm, and (d) 2130 nm. These are reproduced from *Wang* (2007).

higher measurement sensitivities in the SSE with the SWIR bands where there is a substantially larger apart of wavelength distance between two bands, e.g., $\varepsilon(1240, 2130)$.

The implementation of the aerosol LUTs into the MSL12 ocean color data processing system can be achieved by relating the aerosol reflectance $\rho_A(\lambda)$ to its corresponding single-scattering aerosol reflectance $\rho_{as}(\lambda)$, i.e.,

$$\rho_A\left(\lambda_j,\theta_0,\theta,\Delta\phi,\tau_a\right)=\sum_{i=0}^{4} a_i\left(\lambda_j,\theta_0,\theta,\Delta\phi\right)\left[\rho_{as}\left(\lambda_j,\theta_0,\theta,\Delta\phi,\tau_a\right)\right]^i, \tag{8}$$

where $a_i(\lambda_j,\theta_0,\theta,\Delta\phi)$ are coefficients to fit 4th power polynomial for $\rho_A(\lambda_j,\theta_0,\theta,\Delta\phi,\tau_a)$ as a function of $\rho_{as}(\lambda_j,\theta_0,\theta,\Delta\phi,\tau_a)$ in the least-square for all spectral bands λ_j from the UV to SWIR and for the solar-zenith angle θ_0 from 0°–80° at every 2.5°, the sensor-zenith angle θ from 1°–75° at every ~2°, and the relative-azimuth angle $\Delta\phi$ from 0°–180° at every of 10°. Coefficients $a_i(\lambda_j,\theta_0,\theta,\Delta\phi)$ were derived by fitting the curves that were obtained from data simulated with aerosol optical

thicknesses $\tau_a(\lambda)$ of 0.02, 0.05, 0.1, 0.15, 0.2, 0.3, 0.4, 0.6, and 0.8 for the 12 aerosol models. On the other hand, the sensor-measured NIR or SWIR aerosol reflectances need to be converted to the aerosol single-scattering reflectance for atmospheric correction, as well as for retrieval of aerosol optical properties. Therefore, coefficients were also generated for computing the aerosol single-scattering reflectance $\rho_{as}(\lambda)$ as a function of the aerosol reflectance $\rho_A(\lambda)$ at the NIR and SWIR bands (*Wang*, 2007), i.e.,

$$\rho_{as}\left(\lambda_j,\theta_0,\theta,\Delta\phi,\tau_a\right)=\sum_{i=0}^{4} b_i\left(\lambda_j,\theta_0,\theta,\Delta\phi\right)\left[\rho_A\left(\lambda_j,\theta_0,\theta,\Delta\phi,\tau_a\right)\right]^i, \tag{9}$$

where $b_i(\lambda_j,\theta_0,\theta,\Delta\phi)$ are coefficients to fit 4th power polynomial for $\rho_{as}(\lambda_j,\theta_0,\theta,\Delta\phi,\tau_a)$ as a function of $\rho_A(\lambda_j,\theta_0,\theta,\Delta\phi,\tau_a)$ in the least-square for the NIR and SWIR bands, i.e., 765, 865, 1000, 1240, 1640, and 2130 nm (745, 862, 1238, 1601, and 2257 nm for VIIRS-SNPP). By directly calculating $\rho_{as}(\lambda_j,\theta_0,\theta,\Delta\phi,\tau_a)$ using Eq. (9) instead of solving Eq. (8), it eliminates uncertainty and also increases computing efficiency in numerical solution for the high order polynomials (Eq. (8)). These methods (Eqs. (8) and (9)) are accurate and efficient in the data processing. Therefore, the aerosol LUTs are generated as in the forms with which coefficients $a_i(\lambda_j,\theta_0,\theta,\Delta\phi)$ (for all spectral bands from the UV to the SWIR) and $b_i(\lambda_j,\theta_0,\theta,\Delta\phi)$ (for the NIR and SWIR bands) are stored for the solar-zenith angles from 0°–80° at a step of 2.5°, the sensor-zenith angles from 1°–75° at a step of ~2°, and the relative-azimuth angles from 0°–180° at a step of 10°. For any given solar-sensor geometry, a linear interpolation (3-dimension) is carried out to produce the corresponding coefficients $a_i(\lambda_j,\theta_0,\theta,\Delta\phi)$ and $b_i(\lambda_j,\theta_0,\theta,\Delta\phi)$ for computations of $\rho_A(\lambda_j,\theta_0,\theta,\Delta\phi,\tau_a)$ at the UV to the SWIR bands and $\rho_{as}(\lambda_j,\theta_0,\theta,\Delta\phi,\tau_a)$ at the NIR or SWIR bands.

It is noted again that, specifically to the VIIRS-SNPP ocean color data processing, aerosol LUTs were generated and implemented for 10 VIIRS spectral bands at 410, 443, 486, 551, 671, 745, 862, 1238, 1601, and 2257 nm.

To understand the algorithm performance in retrieval of $nL_w(\lambda)$ spectra using the NIR and various combinations of the SWIR bands, simulations have been carried out using the pseudo TOA reflectance simulated with the M80 and the T80 aerosol models as inputs. It is noted that M80 and T80 models are different from the 12 aerosol models used for generating aerosol LUTs (although they are similar). It should also be noted that the performance of the NIR-based atmospheric correction algorithm has been well established from SeaWiFS and MODIS experiences (*Gordon and Wang*, 1994a; *McClain*, 2009; *McClain, et al.*, 2004; *Wang et al.*, 2005). The outputs from the atmospheric correction algorithm using various combinations of the SWIR bands are compared with results that are derived from the NIR-based algorithm. Figures 2 and 3 provide examples of the error in the retrieved water-leaving reflectance from method performed using various combinations of the NIR and SWIR bands. Figures 2(a)–2(d) are the error in the derived water-leaving reflectance $t\rho_w(\lambda)$, for the M80 model with $\tau_a(865)$ of 0.1, as a function of the solar-zenith angle for algorithm performed using the NIR bands of 765 and 865 nm, SWIR bands 1240 and 1640 nm, 1240 and 2130 nm, and 1640 and 2130 nm, respectively, while Figs. 3(a)–3(d) are the corresponding results for the T80 aerosol model. These are all for a

case of the sensor-zenith angle of 45° and the relative-azimuth angle of 90°. Results in Fig. 2 show that, for the M80 model, the atmospheric correction performed using the SWIR band sets of 1000 and 1240 nm, 1240 and 1640 nm, and 1240 and 2130 nm has comparable results as from algorithm using the two NIR (765 and 865 nm) bands. Errors in the derived $t\rho_w(\lambda)$ are all within 0.001 (usually within ~0.0005) for the UV (340 nm) and visible wavelengths (412, 443, 490, and 555 nm). We can draw similar conclusions for the T80 model for cases with which the solar-zenith angles ≤ 70° (Fig. 3).

Using combinations of the SWIR band sets for atmospheric correction, the water-leaving reflectances at the NIR bands can also be derived. In fact, the NIR $nL_w(\lambda)$ data are quite important and useful for turbid coastal and inland waters (*Shi and Wang*, 2014). Figure 4 gives examples of the accuracy in the derived water-leaving reflectances $\Delta[t\rho_w(\lambda)]$ at the NIR bands for the M80 and the T80 aerosol models with $\tau_a(865)$ of 0.1. Figures 4(a) and 4(b) are errors in the derived water-leaving reflectance $\Delta[t\rho_w(\lambda)]$ for the M80 aerosols as a function of the solar-

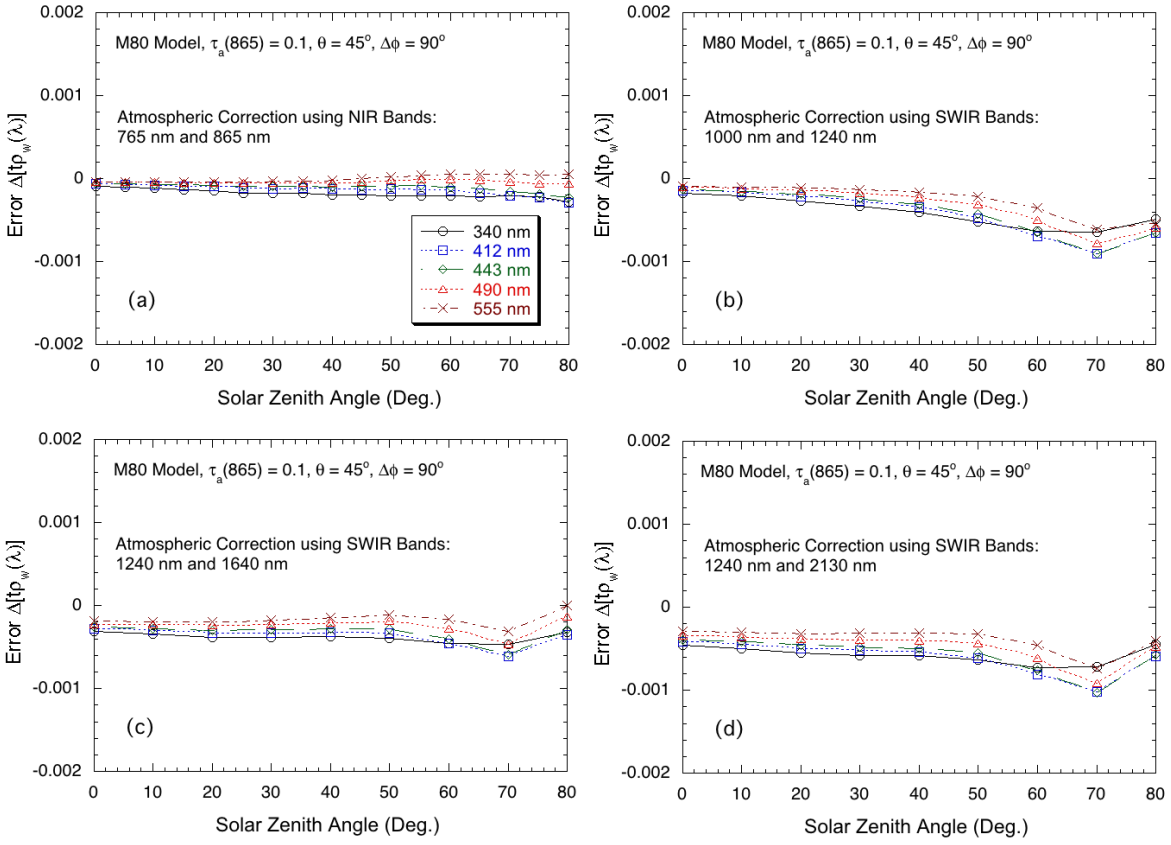

Figure 2. Error in the derived water-leaving reflectance at wavelengths of 340, 412, 443, 490, and 555 nm as a function of the solar-zenith angle for the M80 aerosol model with $\tau_a(865)$ of 0.1 and for algorithm performed using band combinations of (a) 765 and 865 nm, (b) 1000 and 1240 nm, (c) 1240 and 1640, and (d) 1240 and 2130 nm. This is for the case of sensor-zenith angle of 45° and relative-azimuth angle of 90°. These are reproduced from *Wang* (2007).

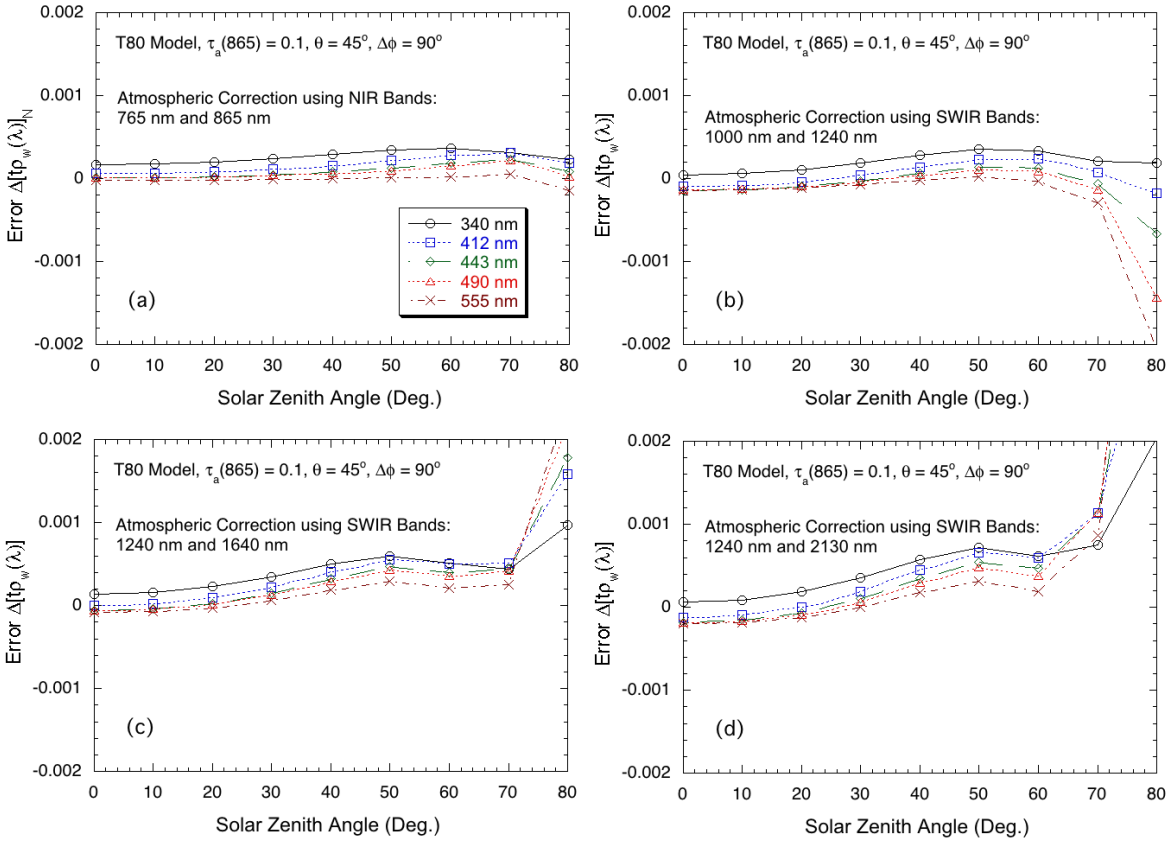

Figure 3. Same as in Fig. 2 except that they are for the T80 aerosol model. These are reproduced from *Wang* (2007).

zenith angle for the NIR wavelengths at 765 and 865 nm, respectively, while Figs. 4(c) and 4(d) are results in $\Delta[t\rho_w(\lambda)]$ for the T80 model for the NIR wavelengths at 765 and 865 nm, respectively. In addition to the three combinations of the SWIR bands presented in Figs. 2 and 3, method using the SWIR bands of 1640 and 2130 nm has also been included in Fig. 4. Figure 4 shows that, except for the method using 1640 and 2130 nm, errors $\Delta[t\rho_w(\lambda)]$ in the NIR bands are almost all within uncertainty of ~10^{-4} for cases with which the solar-zenith angles ≤ 70°.

To further assess the algorithm performance and quantify uncertainty using various combinations of the SWIR bands, simulations have been carried out for all applicable solar-sensor geometry with various aerosol optical properties. Simulations have been carried out for cases with the solar-zenith angles from 0°–80° at a step of 5°, the sensor-zenith angles from 0°–65° at a step of 5°, and the relative-azimuth angles from 0°–180° at a step of 10°, and for the M80 and T80 aerosol models with aerosol optical thicknesses of 0.05, 0.1, and 0.2 at 865 nm. This is total of about 12000 cases (excluding sun glint cases) for each aerosol model (M80 or T80).

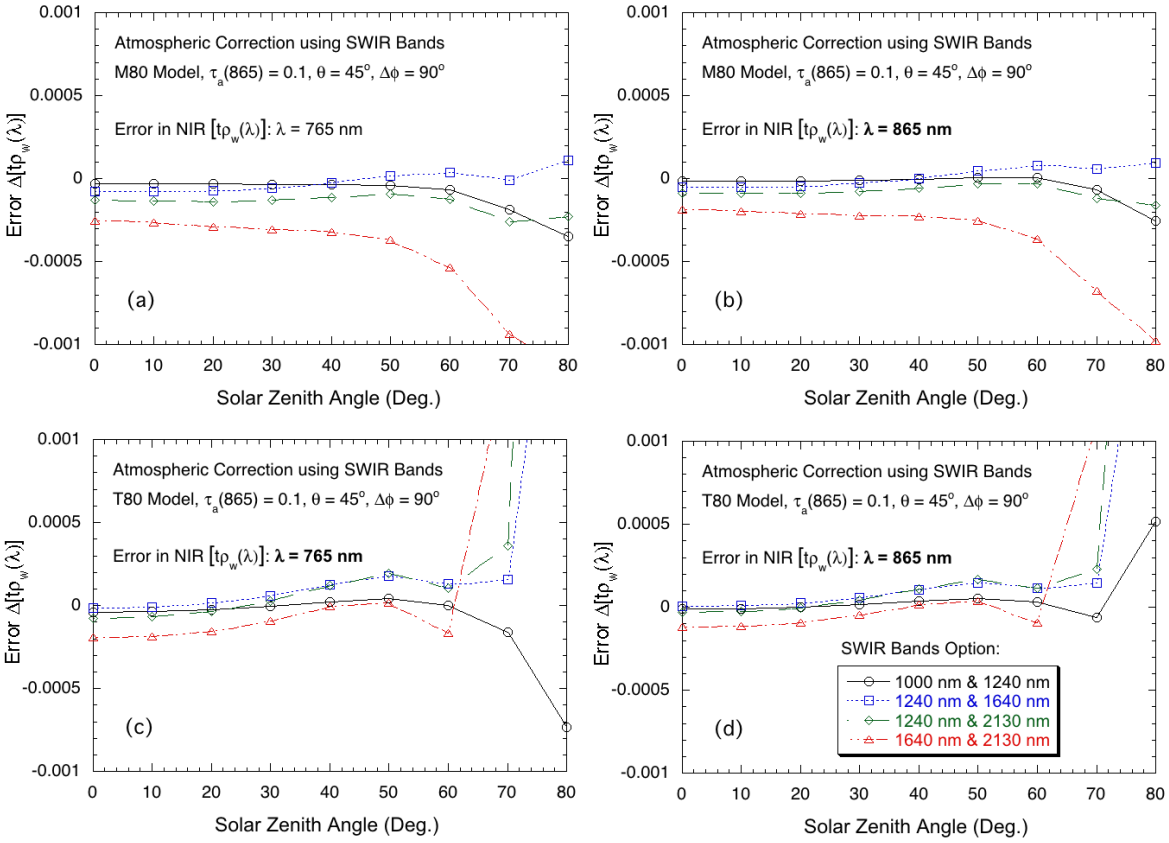

Figure 4. Error in the derived NIR water-leaving reflectance as a function of the solar-zenith angle for algorithm performed using the SWIR band combinations of 1000 and 1240 nm, 1240 and 1640 nm, 1240 and 2130 nm, and 1640 and 2130 nm and for $\Delta[t\rho_w(\lambda)]$ derived at the NIR wavelength with aerosol model of (a) and (b) 765 and 865 nm with the M80 model and (c) and (d) 765 and 865 nm with the T80 model. These are reproduced from *Wang* (2007).

Histogram results and statistics for algorithm performance using the NIR bands and various combinations of the SWIR bands are generated and analyzed. Table 2 summarizes all the results that compare algorithm performance with various bands options for atmospheric correction. In Table 2, percentage of cases for a given error range in the derived water-leaving reflectance for various options in atmospheric correction is provided for the M80 and T80 models. For example, for the UV (340 nm) water-leaving reflectance derived using the NIR bands (765 and 865 nm) method, there are 87.0%, 94.4%, and 98.4% of cases having uncertainty $\Delta[t\rho_w(\lambda)]$ within 5×10^{-4}, 1×10^{-3}, and 2×10^{-3} for the M80 model, respectively, while these percentages are 92.9%, 95.5%, and 97.6% for the T80 model. Comparing with results derived from the NIR bands, however, results from various SWIR band options for atmospheric correction show lower percentage values for the case with the M80 model, while for the T80 model the band option of 1000 and

1240 nm combination provides comparable results as those from the option of the two NIR bands. It is striking to note that algorithms with various band combination options performed as well for the short visible bands as for the UV band (340 nm). Indeed, the water-leaving reflectance at the UV wavelengths (e.g., 340 nm) can be derived accurately due to significantly less aerosol reflectance contributions in the UV bands.

There are apparently two main factors affecting the performances of atmospheric correction using various band combination options (Table 2): (a) the wavelength distance needs to be extrapolated for the aerosol reflectance from the NIR (or SWIR) band and (b) the aerosol reflectance dispersion provided between the two NIR or SWIR bands. Obviously, the aerosol reflectance can usually be more accurately extrapolated for the shorter wavelength distance than for the longer one. Thus, the NIR method generally produces slightly better results than those from the SWIR methods. On the other hand, larger dispersion of the aerosol reflectance between the two NIR (or SWIR) bands with various aerosol models for atmospheric correction has a better sensitivity in deriving aerosol optical properties, leading to a better result in the derived water-leaving reflectances. For example, the SWIR method using bands 1240 and 2130 nm performed much better than that using bands 1640 and 2130 nm because the range of $\varepsilon(1240, 2130)$ for various aerosol models is significantly larger than that of $\varepsilon(1640, 2130)$, e.g., 0.98–4.76 versus 1.04–2.46 in Fig. 1, as well as the extrapolation in the wavelength is shorter from 1240 nm compared with from 1640 nm. It should be noted that for extremely turbid waters the SWIR method using 1640 and 2130 nm bands is required because for such waters the black water assumption for the SWIR 1240 nm band is no longer hold (*Shi and Wang*, 2009).

In summary, except for the method using the SWIR bands of 1640 and 2130 nm, atmospheric correction algorithm using the three SWIR band combinations (1000 and 1240 nm, 1240 and 1640 nm, and 1240 and 2130 nm) can produce comparable results as from the NIR band method for cases of non- and weakly absorbing aerosols, in particular, the SWIR-based atmospheric correction using the band sets of 1240 & 2130 nm and 1240 & 1640 nm for MODIS or 1238 & 2257 nm and 1238 & 1601 nm for VIIRS-SNPP can produce accurate water-leaving radiance spectra data (*Wang*, 2007).

All these analyses can also be applied to the corresponding VIIRS-SNPP (or VIIRS-JPSS-1) NIR and SWIR bands at 745, 862, 1238, 1601, and 2257 nm for atmospheric correction algorithms. In fact, we have been routinely producing VIIRS ocean color products using the VIIRS SWIR bands of 1238 and 1601 nm (M8 and M10) (*Wang et al.*, 2013b).

TABLE 2. Atmospheric correction algorithm performance comparisons using the NIR and various combinations of the SWIR bands (*Wang*, 2007).

λ (nm)	Two Bands for Atmospheric Correction (nm)	**% Cases for Range of** $\|\Delta[t\,\rho_w(\lambda)]\|$ $(\times 10^{-3})$					
		M80 Model			**T80** Model		
		≤ 0.5	≤ 1.0	≤ 2.0	≤ 0.5	≤ 1.0	≤ 2.0
340	765 & 865	87.0	94.4	98.4	92.9	95.5	97.6
	1000 & 1240	64.6	82.8	92.7	93.3	95.6	97.6
	1240 & 1640	70.9	84.6	93.8	86.7	92.1	94.7
	1240 & 2130	48.1	71.3	87.7	76.0	84.3	89.8
	1640 & 2130	23.5	45.5	72.7	75.8	81.4	86.6
412	765 & 865	89.7	95.4	98.4	91.9	94.6	96.6
	1000 & 1240	61.6	79.0	91.3	91.9	94.3	96.2
	1240 & 1640	68.1	81.6	91.7	83.3	88.8	92.1
	1240 & 2130	44.0	66.1	84.2	73.9	80.6	85.8
	1640 & 2130	18.8	38.1	63.0	69.0	77.9	82.7
443	765 & 865	92.9	96.9	98.6	92.4	94.6	96.6
	1000 & 1240	63.0	79.9	91.5	91.3	93.8	95.9
	1240 & 1640	69.9	82.3	91.6	82.8	87.8	91.3
	1240 & 2130	45.1	67.3	84.2	74.7	80.6	85.2
	1640 & 2130	19.0	38.2	62.8	66.7	77.6	82.3
490	765 & 865	93.6	97.1	98.7	92.5	94.6	96.6
	1000 & 1240	69.2	83.0	92.8	90.9	93.3	95.4
	1240 & 1640	74.4	85.0	92.5	82.2	86.6	90.4
	1240 & 2130	50.2	71.1	86.0	75.1	80.1	84.6
	1640 & 2130	22.3	40.3	64.9	66.3	77.3	81.7
510	765 & 865	96.0	97.9	98.8	92.7	94.7	96.7
	1000 & 1240	69.9	83.8	93.2	90.8	93.2	95.4
	1240 & 1640	75.0	85.6	92.6	82.3	86.4	90.2
	1240 & 2130	51.7	71.9	86.2	75.4	80.2	84.5
	1640 & 2130	23.1	40.9	65.4	67.0	77.4	81.7
555	765 & 865	97.7	98.4	98.8	93.6	95.3	96.8
	1000 & 1240	76.3	87.7	95.0	90.4	93.1	95.2
	1240 & 1640	79.5	87.8	93.7	83.1	86.2	89.9
	1240 & 2130	59.9	76.3	88.4	76.8	81.1	84.8
	1640 & 2130	27.0	44.2	68.9	66.5	78.0	82.0

2.3.3. The NIR-SWIR combined atmospheric correction algorithm

Wang and Shi (2007) described and demonstrated a NIR-SWIR combined atmospheric correction method for the MODIS ocean color data processing. This approach can also be directly applied to VIIRS with the corresponding VIIRS bands. In this NIR-SWIR-based atmospheric correction method, pixels in ocean or inland water regions with significant NIR water radiance contributions (i.e., turbid waters) can first be discriminated using MODIS or VIIRS measurements. Turbid waters can be detected using the turbid water index that is computed from the VIIRS-measured radiances at the NIR and SWIR bands. The turbid water index, T_{ind}, can be derived as (*Shi and Wang*, 2007):

$$T_{ind} = 1 + t(748)\,\rho_w(748) / \rho_A(748), \text{ for MODIS or}$$

$$T_{ind} = 1 + t(745)\,\rho_w(745) / \rho_A(745), \text{ for VIIRS,} \quad (10)$$

where $t(748)\rho_w(748)$ and $\rho_A(748)$ (or $t(745)\rho_w(745)$ and $\rho_A(745)$ for VIIRS) are the TOA water-leaving reflectance and aerosol reflectance (including Rayleigh-aerosol interactions) at the wavelength of 748 nm for MODIS or 745 nm for VIIRS (*Shi and Wang*, 2007), respectively.

The turbid water detection can be operated prior to the atmospheric correction procedure. Thus, different atmospheric correction algorithms can be used for turbid water cases. In the NIR-SWIR combined atmospheric correction approach, the SWIR atmospheric correction algorithm can be applied for the identified turbid water pixels (*Wang*, 2007; *Wang and Shi*, 2007). For the most other pixels (non-turbid ocean waters), the standard NIR atmospheric correction algorithm (*Gordon and Wang*, 1994a) can be employed. Thus, while the ocean color products in the coastal regions can be improved using the SWIR-based method, high quality ocean color data in open oceans can still be routinely produced. In the MSL12 ocean color data processing system for VIIRS, the NIR-SWIR algorithm is switched on in the input parameter file, and the threshold for detecting the turbid water is set to 1.1, i.e., the SWIR-based atmospheric correction can be operated for cases with $T_{ind} \geq 1.1$. Otherwise, for cases with $T_{ind} < 1.1$, the NIR-based atmospheric correction algorithm is used. All details (and results) for the NIR-SWIR combined atmospheric correction algorithm can be found in (*Shi and Wang*, 2007; *Wang*, 2007; *Wang and Shi*, 2007; *Wang, et al.*, 2009b).

Alternatively, the NIR-SWIR switching can be done after the NIR water-leaving reflectance correction (*Jiang and Wang*, 2014), i.e., using the derived NIR water-leaving reflectance value as a threshold. If the NIR-based atmospheric correction results in VIIRS-derived $nL_w(862) > 0.3$ mW cm^{-2} μm^{-1} sr^{-1}, the atmospheric correction algorithm can switch to the SWIR-based method (*Wang*, 2007). For cases with $nL_w(862) < 0.1$ mW cm^{-2} μm^{-1} sr^{-1}, the NIR-based $nL_w(\lambda)$ results from the *Jiang and Wang* (2014) algorithm are kept. If the NIR-based atmospheric correction results in $0.1 \leq nL_w(862) \leq 0.3$ mW cm^{-2} μm^{-1} sr^{-1}, all $nL_w(\lambda)$ values are interpolated between the NIR-based and SWIR-based atmospheric correction results. This method makes sure that the switching between the NIR- and SWIR-based methods is smooth and renders better $nL_w(\lambda)$ results. In the most current version of MSL12, because of much improved NIR reflectance correction algorithm (i.e., with reliable NIR $nL_w(\lambda)$ data) (*Jiang and Wang*, 2014), this switching method is used in place of the original turbid-index-based NIR-SWIR switching method.

2.3.4. Algorithms improvements

There have been some considerable efforts for improving algorithms (or adding new algorithms) in MSL12 for satellite ocean color data processing. With these algorithms improvements, VIIRS ocean color products have been significantly improved. Some specific algorithm improvements for VIIRS ocean color data processing are briefly described in the following sub-sections.

2.3.4.1. New Rayleigh radiance computations for all satellite sensors

In the satellite ocean color data processing, it is essential to compute precisely the TOA Rayleigh-scattering radiance or reflectance (i.e., $L_r(\lambda)$ or $\rho_r(\lambda)$ in Eq. (2)) in order to derive accurate ocean color products (*Gordon and Wang*, 1994a; *IOCCG*, 2010). In a series of works for improving the satellite ocean color data processing (atmospheric correction), the TOA Rayleigh-scattering radiance computation using the radiative transfer simulation has included the polarization effect (*Gordon, et al.*, 1988a), the sea surface roughness (wind speed) effect (*Gordon and Wang*, 1992; *Wang*, 1991; 2002), and the effect of surface atmospheric pressure variation (*Gordon, et al.*, 1988a; *Wang*, 2005). In a recent work (*Wang*, 2016), the VIIRS spectral response function (SRF) effect on the accuracy of the TOA Rayleigh radiance computations is evaluated for all applicable solar-sensor geometries and for the VIIRS visible and NIR bands for both SNPP and JPSS-1. To understand and assess the effect of the sensor SRF on the accuracy of the TOA Rayleigh-scattering radiance computation, new TOA Rayleigh radiance LUTs over global oceans and inland waters have been generated. The new Rayleigh LUTs include spectral coverage of 335–2555 nm, all possible solar-sensor geometries, and surface wind speeds of 0–30 m/s. Using the new Rayleigh LUTs, the effect of VIIRS SRFs on the accuracy of the VIIRS TOA Rayleigh radiance computations is assessed and analyzed, showing some important errors associated with the large solar- and/or sensor-zenith angles, as well as for the large Rayleigh optical thicknesses (i.e., short wavelengths), bands with broad spectral bandwidths, and large sensor out-of-band (OOB) effects (*Wang et al.*, 2001; *Wang et al.*, 2016b). To accurately account for the sensor SRF effect, a new correction algorithm has been developed for VIIRS spectral bands, which improves the TOA Rayleigh radiance accuracy to ~0.01% even for the large solar-zenith angles of 70°–80°, compared with the error of ~0.7% without applying the correction for the VIIRS-SNPP 410 nm band. The same methodology that accounts for the sensor SRF effect on the Rayleigh radiance computation can be used for other satellite sensors. In addition, with the new Rayleigh LUTs, the effect of surface atmospheric pressure variation on the TOA Rayleigh radiance computation can be done precisely, and no specific atmospheric pressure correction algorithm is needed. There are some other important applications and advantages to use the new Rayleigh LUTs for satellite remote sensing, including an efficient and accurate TOA Rayleigh radiance computation for hyperspectral satellite remote sensing, detector-based TOA Rayleigh radiance computation, Rayleigh radiance calculations for high altitude lakes, and the same Rayleigh LUTs are applicable for all satellite sensors over the global ocean and inland waters. The new Rayleigh LUTs have been implemented in the MSL12 for VIIRS ocean color data processing for routine production of global ocean color and inland water products (*Wang*, 2016).

2.3.4.2. Improved NIR ocean reflectance correction algorithm

The NIR-SWIR method described in Section 2.3.3 has been shown to have good performance in both open oceans and turbid coastal and inland waters for the MODIS ocean color data processing, in particular, significantly improved ocean color products using the SWIR atmospheric correction over turbid coastal and inland waters. However, as in the MODIS SWIR noise issue (*Wang and Shi*, 2012), VIIRS SWIR bands also have significant noise issue and may still have some calibration issues. For not very turbid waters, the NIR-based ocean reflectance correction algorithms can be used (*Bailey, et al.*, 2010; *Jiang and Wang*, 2014; *Ruddick, et al.*, 2000; *Stumpf, et al.*, 2003; *Wang, et al.*, 2012). *Stumpf et al.* (2003) and *Bailey et al.* (2010) proposed iterative algorithms to estimate the $nL_w(\lambda)$ of the two NIR bands from visible $nL_w(\lambda)$ and derived Chl-a by exploiting the relationship between non-water absorption at the red band and Chl-a concentration, as well as the wavelength dependence on the non-water backscattering coefficients at red and NIR bands. However, *Bailey et al.* (2010) and *Stumpf et al.* (2003) algorithms may not work well for highly turbid coastal and inland waters, such as sediment-dominated or CDOM-dominated waters. In an effort to deal with the highly turbid waters in China's east coastal region, *Wang et al.* (2012) developed a NIR water reflectance correction algorithm for the Korean GOCI onboard the Communication, Ocean, and Meteorological Satellite (COMS) (*Wang, et al.*, 2013a). Based on regional empirical relationships between the NIR-$nL_w(\lambda)$ and the water diffuse attenuation coefficient at the wavelength of 490 nm $K_d(490)$, an iterative scheme with the NIR-based atmospheric correction algorithm has been developed and used for processing GOCI data for producing ocean color products (*Wang, et al.*, 2013a). The iterative method used in *Stumpf et al.* (2003), *Bailey et al.* (2010), and *Wang et al.* (2012) is generally a typical approach to estimate $nL_w(\lambda)$ of the two NIR bands. On the other hand, *Ruddick et al.* (2000) proposed a non-iterative approach for SeaWiFS atmospheric correction for ocean color data processing over coastal and inland waters. *Ruddick et al.* (2000) model is also often referred to as MUMM model, with MUMM standing for the Management Unit of the North Sea Mathematical Models, which is the institute the authors are affiliated.

All these NIR $nL_w(\lambda)$ estimation approaches for atmospheric correction discussed above, in particular, the *Bailey et al.* (2010), MUMM (or *Ruddick et al.* (2000)), and *Wang et al.* (2012 algorithms, have advantages and disadvantages. Based on the three methods, *Jiang and Wang* (2014) proposed a new approach that combines *Bailey et al.* (2010), MUMM (or *Ruddick et al.* (2000)), and *Wang et al.* (2012) algorithms into a single algorithm, named as the BMW algorithm, while trying to overcome their disadvantages. It has been shown that the BMW algorithm produces most consistent results with the SWIR atmospheric correction approach in turbid water regions among all NIR ocean reflectance correction algorithms (*Jiang and Wang*, 2014). Therefore, the improved BMW NIR ocean reflectance correction algorithm has been implemented in the MSL12 software package, and has been used for the routine VIIRS global ocean color data processing.

2.3.4.3. Stray light and cloud shadow algorithm

For satellite ocean color products, there are mainly four types of cloudy-related contaminations: cloud itself, stray light due to the spreading of the light source, stray light due to

reflection and scattering of photons in nearby pixels of high TOA radiance, and cloud shadow effect. The first two types of contamination can be detected and masked using cloud masking algorithm (*Wang and Shi*, 2006). But, to detect pixels with cloud stray light contamination from the scattering effect and cloud shadow, some special algorithms are needed. *Jiang and Wang* (2013) proposed a new method for detecting the stray light and cloud shadow pixels for VIIRS. Basically, the method is based on the climatology data of $nL_w(551)$: the VIIRS-derived $nL_w(551)$ of a given pixel is compared with the climatology data of the pixel and its surrounding pixels (*Jiang and Wang*, 2013). For a pixel with the VIIRS-derived $nL_w(551)$ out of the reference range set by the climatology $nL_w(551)$ data, a flag for the corresponding pixel is set to indicate the pixel is contaminated by stray light or cloud shadow effects. The algorithm to identify pixels contaminated by the stray light and cloud shadowing has been implemented in the MSL12 for VIIRS global ocean color processing (*Jiang and Wang*, 2013). The output is a flag (a 0-1 bit) to indicate if the stray light/cloud shadow status for a given pixel.

2.3.4.4. Destriping algorithm

Similar to MODIS, the multi-detector arrangement of VIIRS gives rise to stripping noise in the solar reflective bands and thermal infrared bands. This is mainly due to the calibration or performance differences among the detectors of VIIRS. The pattern of striping noise exhibits periodicity in the along-track direction with the period equal to the number of detectors, and should be removed from the normalized water-leaving radiance $nL_w(\lambda)$ before further deriving other ocean color products (*Mikelsons, et al.*, 2014). *Mikelsons et al.* (2014) developed a destriping algorithm for the VIIRS solar reflective bands. Specifically, the destriping algorithm is applied to remove striping from VIIRS-derived normalized water-leaving radiance spectra $nL_w(\lambda)$ obtained from solar reflective bands (*Mikelsons, et al.*, 2014). It is important that the destriping approach not be applied to the TOA radiances because some TOA "stripping" features are real (not artifacts) (*Mikelsons, et al.*, 2014). Although the striping has a large variance in the solar reflective bands, *Mikelsons et al.* (2014) have demonstrated that, with appropriately chosen parameters and adjustments, the striping noise in the solar reflective band data can be successfully removed. The sensor destriping algorithm has been implemented in MSL12 for VIIRS ocean color data processing, and shown to have a significantly improvement in imagery quality for VIIRS-derived ocean and inland water optical, biological, an biogeochemical products (*Mikelsons, et al.*, 2014).

2.4. Ocean color products derived from $nL_w(\lambda)$ spectra

After $nL_w(\lambda)$ spectra are obtained using the algorithm described in Section 2.3, ocean biological and biogeochemical products such as Chl-a concentration, $K_d(490)$, and $K_d(\text{PAR})$, as well as IOPs, etc., can be derived from satellite-measured $nL_w(\lambda)$ spectra data. In this section, a suite of satellite algorithms for ocean biological and biogeochemical products is described.

2.4.1. Chl-a algorithm

For satellite ocean color remote sensing, phytoplankton Chl-a concentrations have been measured from space using empirical regressions of spectral ratios of normalized water-leaving

reflectance $\rho_{wN}(\lambda)$ (*Gordon et al.*, 1988b; *Gordon and Morel*, 1983; *O'Reilly, et al.*, 1998; *O'Reilly, et al.*, 2000). The widely used satellite Chl-a algorithm is based on the blue-green reflectance ratio empirical algorithm, i.e., ocean chlorophyll-type (OCx) algorithm (*O'Reilly, et al.*, 1998; *O'Reilly, et al.*, 2000). The empirical blue-green reflectance ratio algorithm (*O'Reilly, et al.*, 1998) has also been implemented in MSL12 and used for generating VIIRS global Chl-a data. In particular, the reflectance ratio algorithm has been adjusted for VIIRS spectral bands. Specifically, the 3-band VIIRS Chl-a algorithm (named OC3V—Ocean Chlorophyll 3-band algorithm for VIIRS) uses three VIIRS-derived $\rho_{wN}(\lambda)$ at wavelengths of 443, 486, and 551 nm. The OC3V Chl-a algorithm for VIIRS is given as follows:

$$\log_{10}\left[Chl\text{-}a\right] = c_0 + c_1 r + c_2 r^2 + c_3 r^3 + c_4 r^4, \tag{11}$$

where $r = max\ [\rho_{wN}(443)/\rho_{wN}(551),\ \rho_{wN}(486)/\rho_{wN}(551)]$ (i.e., the value with a larger reflectance ratio from the two reflectance ratio values) and fitting coefficients for c_0, c_1, c_2, c_3, and c_4 are 0.2228, –2.4683, 1.5867, –0.4275, and –0.7768, respectively. Using Eq. (11), VIIRS global Chl-a data have been routinely produced since the launch of VIIRS-SNPP.

2.4.2. K_d(490) algorithm

The diffuse attenuation coefficient at the wavelength of 490 nm, $K_d(490)$, is an important water property related to light penetration and availability in aquatic systems. Accurate estimation of the diffuse attenuation coefficient is critical to understand not only physical processes such as the heat transfer in the upper layer of the ocean (*Morel and Antoine*, 1994; *Sathyendranath, et al.*, 1991), but also biological processes such as phytoplankton photosynthesis in the ocean euphotic zone (*Platt, et al.*, 1988; *Sathyendranath, et al.*, 1989). The VIIRS $K_d(490)$ algorithm is from *Wang et al.* (2009a) (implemented in MSL12), which is a combination of a clear open ocean $K_d(490)$ algorithm (*Mueller*, 2000) and a turbid water $K_d(490)$ algorithm (*Wang, et al.*, 2009a). In particular, for turbid coastal and inland waters, the backscattering coefficient at the wavelength 490 nm can be more accurately correlated to the irradiance reflectance at the red bands (*Wang, et al.*, 2009a). In fact, the *Wang et al.* (2009a) $K_d(490)$ algorithm was developed using the MODIS-Aqua data. Specifically, VIIRS $K_d(490)$ algorithm can be expressed as (*Wang, et al.*, 2009a):

$$K_d(490) = (1 - W)\,K_d^{Clear}(490) + W\,K_d^{Turbid}(490) \tag{12}$$

and for clear open ocean waters $K_d^{Clear}(490)$ can be written as (*Mueller*, 2000)

$$K_d^{Clear}(490) = 0.1853\left(\frac{nL_w(486)}{nL_w(551)}\right)^{-1.349}, \tag{13}$$

while for turbid waters $K_d^{Turbid}(490)$ is given by (*Wang, et al.*, 2009a)

$$K_d^{Turbid}(490) = \frac{2.697\times10^{-4}}{R(486)} + 1.045\frac{R(671)}{R(486)} + 4.18\left[7\times10^{-4} + 2.7135\,R(671)\right]\left[1 - 0.52\exp\left(-\frac{2.533\times10^{-3}}{R(486)} - 9.817\frac{R(671)}{R(486)}\right)\right] \quad (14)$$

with $R(\lambda)$ computed from the VIIRS-derived $nL_w(\lambda)$ (*Gordon, et al.*, 1988b; *Lee, et al.*, 2002; *Mobley*, 1994) with assuming the *Q* factor of 4 for Case-2 waters (*Loisel and Morel*, 2001):

$$R(\lambda) = \frac{4\,nL_w(\lambda)}{0.52\,F_0(\lambda) + 1.7\,nL_w(\lambda)}, \quad (15)$$

where $F_0(\lambda)$ is the extraterrestrial solar irradiance (*Thuillier, et al.*, 2003) at a given wavelength λ. The weighting function W in Eq. (12) is given by

$$W = -1.175 + 4.512\frac{R_{rs}(671)}{R_{rs}(486)}, \text{ for } 0.2604 \le \frac{R_{rs}(671)}{R_{rs}(486)} \le 0.4821, \quad (16)$$

with $W = 0$ for $W \le 0$ and $W = 1$ for $W \ge 1$ from Eq. (16). It is noted that the weighting function in Eq. (16) is applied to $K_d(490)$ between ~0.3–0.6 m^{-1} (*Wang, et al.*, 2009a). In fact, in Eq. (12) $K_d^{Clear}(490)$ is the model for open oceans, i.e., from *Mueller* (2000) (Eq. (13)), and $K_d^{Turbid}(490)$ is the model for turbid coastal and inland waters, i.e., from *Wang et al.* (2009a) (Eq. (14)). Thus, for values of $K_d(490) \le$ ~0.3 m^{-1}, $K_d(490)$ in Eq. (12) produces diffuse attenuation coefficient using the $K_d^{Clear}(490)$ model, while for values of $K_d(490) \ge$ ~0.6 m^{-1} the $K_d^{Turbid}(490)$ model is used in Eq. (12). For values of $K_d(490)$ between ~0.3–0.6 m^{-1}, a weight according to Eq. (16) is used to combine values produced from models of $K_d^{Clear}(490)$ and $K_d^{Turbid}(490)$ (*Wang, et al.*, 2009a). Therefore, VIIRS $K_d(490)$ data have been routinely produced using the *Wang et al.* (2009a) algorithm (Eqs. (12)–(16)) for global open oceans and coastal/inland waters (*Wang, et al.*, 2016a; *Wang, et al.*, 2014; 2015a; *Wang, et al.*, 2013b).

2.4.3. K_d(PAR) algorithm

Although $K_d(490)$ is generally used for the clarity of the water column, there is a need for a satellite-derived diffuse attenuation coefficient for the photosynthetically available radiation (PAR), K_d(PAR), to estimate heat flux within the upper water column in oceanic and atmospheric circulation models (*Gnanadesikan et al.*, 2010; *Rochford et al.*, 2001). For example, K_d(PAR) is one of the required inputs to the Hybrid Coordinate Ocean Model (HYCOM) (*Chassignet et al.*, 2007; *Chassignet et al.*, 2003) used in the NOAA National Centers for Environmental Prediction (NCEP). HYCOM is a primitive-equation for the ocean general circulation model that evolved from the Miami Isopycnic-Coordinate Ocean Model (MICOM) (*Bleck*, 2002).

In general, $K_d(490)$ can be used as a surrogate for K_d(PAR) for phytoplankton primary production models (*IOCCG*, 2004). Studies have shown that there are robust correlations between $K_d(490)$ and K_d(PAR) in various ocean waters (*Kratzer et al.*, 2003; *Morel, et al.*, 2007; *Pierson et al.*, 2008; *Wang, et al.*, 2009a), but the relationship generally varies regionally with a

wide range. Using the similar approach of *Wang et al.* (2009a) for $K_d(490)$, *Son and Wang* (2015) developed a new $K_d(\mathrm{PAR})$ algorithm which combines the $K_d(\mathrm{PAR})$ for clear open oceans and turbid coastal/inland waters as follows:

$$K_d(\mathrm{PAR}) = (1-W)K_d^{Clear}(\mathrm{PAR}) + WK_d^{Turbid}(\mathrm{PAR}) \tag{17}$$

where $K_d^{Clear}(\mathrm{PAR})$ (*Morel, et al.*, 2007), $K_d^{Turbid}(\mathrm{PAR})$ (*Wang, et al.*, 2009a), and weight W are defined as (*Son and Wang*, 2015):

$$K_d^{Clear}(\mathrm{PAR}) = 0.0864 + 0.8K_d(490) - 0.00137\left[K_d(490)\right]^{-1}, \tag{18}$$

$$K_d^{Turbid}(\mathrm{PAR}) = 0.8045\left[K_d(490)\right]^{0.917}, \tag{19}$$

and

$$\begin{aligned} &W = 0, \text{ for } \rho_{wN}(671)/\rho_{wN}(486) < 0.2604, \\ &W = -1.175 + 4.512\,\rho_{wN}(671)/\rho_{wN}(486), \text{ for } 0.2604 \le \rho_{wN}(671)/\rho_{wN}(486) \le 0.4821, \\ &W = 1, \text{ for } \rho_{wN}(671)/\rho_{wN}(486) > 0.4821. \end{aligned} \tag{20}$$

As shown in Eqs. (17)–(20), $K_d(\mathrm{PAR})$ is actually converted from $K_d(490)$, which is derived from *Wang et al.* (2009a) as described in the previous section. In fact, for clear waters (with low reflectance ratio values), $K_d(\mathrm{PAR})$ data are derived from the *Morel et al.* (2007) model (Eq. (18)), while for turbid coastal and inland waters (with high reflectance ratio values) the *Wang et al.* (2009a) algorithm (Eq. (19)) is used for $K_d(\mathrm{PAR})$ computation. Between these two $K_d(\mathrm{PAR})$ models, there are transition values using Eqs. (17)–(20) to have smooth $K_d(\mathrm{PAR})$ product across all $K_d(\mathrm{PAR})$ values (*Son and Wang*, 2015).

2.4.4. Inherent Optical Properties (IOPs) algorithm

IOPs, i.e., absorption and backscattering coefficients, are directly linked to the constituents in the water, and their values can be used to determine the type of water, subsurface light intensity, solar heat flux with depth, turbidity, pigment concentration, and sediment loading to name a few applications. Methods to accurately retrieve these optical properties remotely have been under investigation for several decades, and algorithms from empirical to full-spectral optimization have been proposed. In MSL12, the quasi-analytical algorithm (QAA) developed by *Lee et al.* (2002) has been implemented for generating the IOP products from VIIRS measurements. QAA is based on remote-sensing reflectance models derived from the radiative transfer equation, and values of total absorption and backscattering coefficients are analytically calculated from values of remote-sensing reflectance (*Lee, et al.*, 2002). In the calculation of total absorption coefficient, no spectral models for phytoplankton pigment and CDOM absorption coefficients are used. Actually, those absorption coefficients are spectrally decomposed from the derived total absorption coefficient in a separate calculation. The output products of the QAA include the total absorption and backscattering coefficients ($a(\lambda)$ and $b_b(\lambda)$), the decomposed absorption coefficients of phytoplankton pigment ($a_{ph}(\lambda)$) and CDOM

($a_{dg}(\lambda)$), and backscattering coefficient of suspended particles ($b_{bp}(\lambda)$) for the five VIIRS visible M-bands at 410, 443, 486, 551, and 671 nm. Thus, MSL12 can produce total IOP products from VIIRS measurements as 5 (IOPs) × 5 (spectral bands) = 25 parameters. However, it should be noted that VIIRS-derived IOPs are experimental products.

2.4.5. Chl-a derived from the OCI algorithm

Recent studies have been reported that the empirical estimation of Chl-a from the ocean color satellites using the blue-green reflectance ratio can have considerable noise errors for oligotrophic waters over cases such as patchiness, speckle noises, and spatial incoherence (*Dierssen*, 2010; *Hu, et al.*, 2012; *Wang and Son*, 2016). A new Chl-a algorithm based on the color index (CI), which is defined as remote sensing reflectance ($R_{rs}(\lambda)$) at the green band and a reference formed linearly by $R_{rs}(\lambda)$ at the blue and red bands, has been developed for the ocean color remote sensing (*Hu, et al.*, 2012). The CI-based Chl-a algorithm has also been implemented in MSL12 for deriving VIIRS Chl-a data over oligotrophic waters (*Wang and Son*, 2016). In fact, *Hu et al.* (2012) and *Wang and Son* (2016) show that over oligotrophic ocean waters the CI-based Chl-a algorithm significantly reduces Chl-a data errors, which are induced by instrument noise and calibration errors, as well as from imperfect atmospheric correction such as contamination from sun glint, whitecap correction, aerosol correction, and some other errors.

Since the CI-based Chl-a algorithm (reflectance difference-based) is only applicable to the oligotrophic waters with Chl-a < ~0.3 mg m^{-3}, the reflectance ratio-based OC3V algorithm for VIIRS is still needed for Chl-a > ~0.3 mg m^{-3}. This new Chl-a algorithm that combines two types of Chl-a algorithms (OCx-based and CI-based) is called ocean color index (OCI) algorithm (*Hu, et al.*, 2012). *Wang and Son* (2016) proposed a new approach that utilizes both OC3V and CI-based algorithms, and improved the two algorithms merging method using the blue-green reflectance ratio values. Specifically, the new OCI Chl-a algorithm for VIIRS (i.e., using VIIRS bands at 443, 551, and 671 nm) can be written as:

$$\begin{aligned} CI &= R_{rs}(551) - 0.526\,R_{rs}(443) - 0.474\,R_{rs}(671) \\ [Chl\text{-}a]_{\mathrm{CI}} &= 10^{216.76CI - 0.4093} \end{aligned} \quad . \tag{21}$$

We define Chl-a data derived from OC3V and CI as $[Chl\text{-}a]_{\mathrm{OC3V}}$ and $[Chl\text{-}a]_{\mathrm{CI}}$, respectively, and follow *Hu et al.* (2012) to define the merged Chl-a algorithm based on OC3V and CI as OCI. The OCI Chl-a algorithm for VIIRS can then be written as

$$\begin{aligned} [Chl\text{-}a]_{\mathrm{OCI}} &= [Chl\text{-}a]_{\mathrm{CI}} \text{ for } r > 4, \\ [Chl\text{-}a]_{\mathrm{OCI}} &= w[Chl\text{-}a]_{\mathrm{CI}} + (1-w)[Chl\text{-}a]_{\mathrm{CI}} \text{ for } 2 < r \le 4, \text{ and} \\ [Chl\text{-}a]_{\mathrm{OCI}} &= [Chl\text{-}a]_{\mathrm{OC3V}} \text{ for } r \le 2 \end{aligned} \tag{22}$$

with the weight of

$$w = 0.5(r-2) \text{ for } 2 < r \le 4,$$
$$w = 0 \text{ for } r \le 2, \text{ and} \quad , \tag{23}$$
$$w = 1 \text{ for } r > 4$$

and $r = R_{rs}(443)/R_{rs}(551)$ (blue-green reflectance ratio). VIIRS-OCI Chl-a algorithm as described in Eqs. (21)–(23) has been implemented into the MSL12 ocean color data processing system for deriving VIIRS global Chl-a data (*Wang and Son*, 2016).

Advantages to use the CI-based Chl-a algorithm over oligotrophic waters have been well demonstrated (*Hu, et al.*, 2012; *Wang and Son*, 2016). In fact, using the MOBY in situ optics data, *Wang and Son* (2016) have conclusively shown that the OCI-based Chl-a algorithm can produce much improved VIIRS Chl-a data. Figure 5 shows VIIRS-derived Chl-a data compared with those derived from MOBY in situ reflectance data. It should be noted that results from Fig. 5 essentially show the effect of errors in satellite-measured $nL_w(\lambda)$ data on the Chl-a algorithm. Figures 5a and 5b are Chl-a comparison results derived using the OC3V and the original OCI-based algorithm by *Hu et al.* (2012) with both using the IDPS-SDR, while Figs. 5c and 5d are Chl-a results using the OC3V and the new OCI algorithm by *Wang and Son* (2016) with both using the improved OC-SDR. Figure 5 shows that using the OCI-based algorithms Chl-a data are significantly improved with considerably reduced sensor noise and calibration errors (i.e., Fig. 5a versus Fig. 5b), as well as atmospheric correction errors (i.e., Fig. 5c versus Fig. 5d). It should be noted that differences between Figs 5a and 5c (or Figs 5b and 5d) are due to different sensor calibrations, showing that instrument calibration has been significantly improved with the OC-SDR. Results also show that the OCI-based Chl-a algorithm is quite effective to remove instrument noise and calibration errors (Fig. 5a versus Fig. 5b) for oligotrophic waters. Therefore, from these algorithm performance evaluation results, it shows that the new OCI-based Chl-a algorithm can produce improved VIIRS Chl-a data particularly over oligotrophic waters.

It should be particularly noted that, although the OCI-based VIIRS Chl-a product is still as experimental data, the product will soon be standard one in replace the OC3V-based Chl-a data.

2.4.6. Photosynthetically available radiation (PAR)

Photosynthetically available radiation (PAR) is defined as solar radiation in spectral range from 400–700 nm that photosynthetic organisms are able to use in the process of photosynthesis. For ocean color applications, PAR is estimated daily (i.e., 24-hour averaged) for PAR value reaching ocean surface (expressed in Einstein/m^2/d) (*Frouin et al.*, 2003). In fact, PAR is an important parameter for ocean phytoplankton primary productivity computations. VIIRS PAR product has been generated using the same PAR algorithm for SeaWiFS and MODIS (*Frouin, et al.*, 2003; *Frouin et al.*, 2012), which has been implemented in MSL12 using the input of the VIIRS TOA radiance data at M1–M5 bands (410–671 nm).

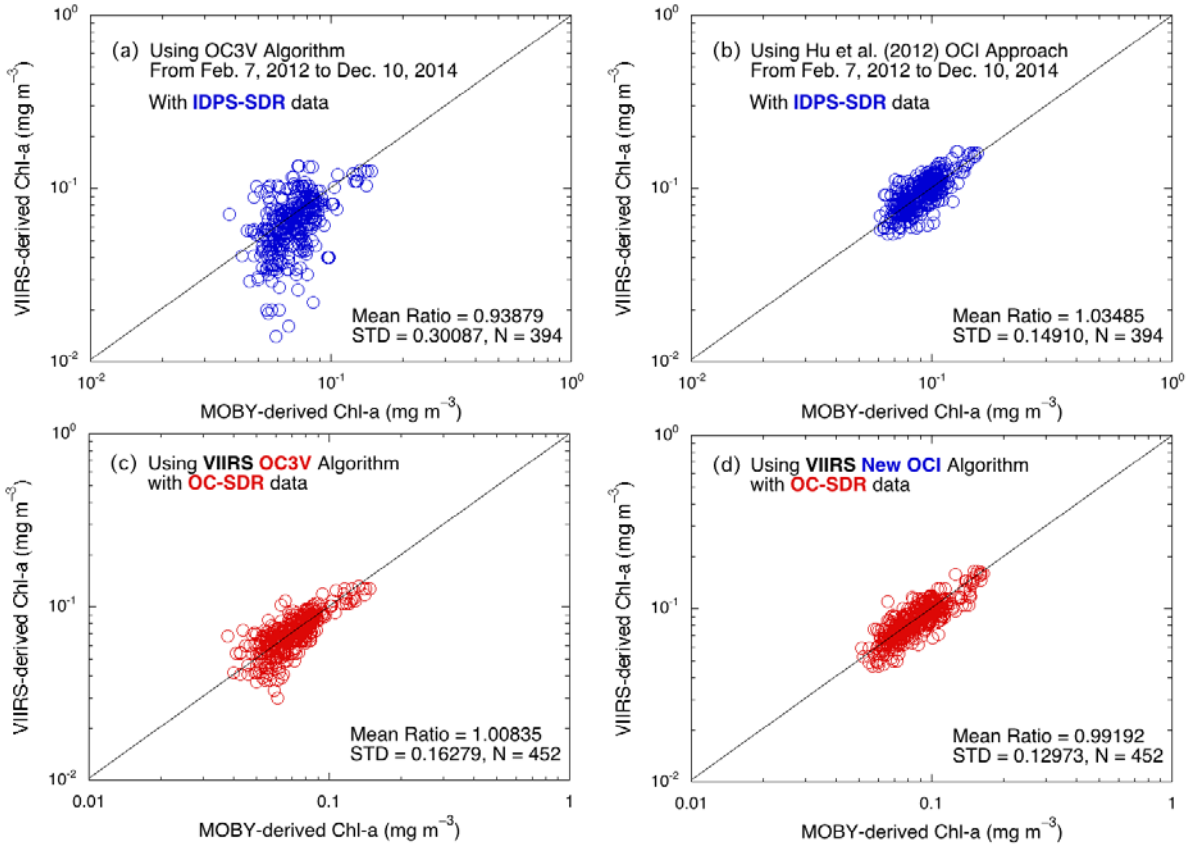

Figure 5. VIIRS-derived Chl-a data compared with those derived from the in situ MOBY optics data using the same Chl-a algorithm of (a) the OC3V with IDPS-SDR, (b) the original CI-based algorithm by *Hu et al.* (2012) with IDPS-SDR, (c) the OC3V with OC-SDR, and (d) the new OCI algorithm of *Wang and Son* (2016) with OC-SDR. Note that differences between results in (a) and (c) and between (b) and (d) are due to using different SDR, i.e., IDPS-SDR for (a) and (c) versus OC-SDR for (b) and (d). These are reproduced from *Wang and Son* (2016).

2.5. Algorithm Outputs

The MSL12 generates VIIRS EDR data file in NetCDF-4 format, which also complies with the Climate and Forecast (CF) Conventions as international standards. Specifically, the output EDR file contains the following standard data products: $nL_w(\lambda)$ for VIIRS M1–M5 bands at 410, 443, 486, 551, and 671 nm, Chl-a using the OC3V algorithm, K_d(490), and K_d(PAR), with total of eight products. In addition, the following experimental products can be optionally generated: Chl-a using the OCI algorithm, IOPs at VIIRS M1–M5 bands, and PAR, with currently total of 27 parameters. It should be noted that experimental products would be promoted to standard ones as they become matures and validated. New experimental products will also be added when

they are deemed to be useful. A list of the current standard and experimental products from MSL12 ocean color data processing system is summarized in Table 3. Details of the L2 Flags in Table 3 are described in Table 4 with noted default masks used in Level-2 and Level-3 ocean color data processing using MSL12. In Table 4, the current default thresholds for solar-zenith angle, sensor-zenith angle, and Chl-a range are 70°, 60°, and 0–100 mg m^{-3}, respectively. The default values for high AOT at 862 nm, very low $nL_w(\lambda)$ at the green band, and the maximum iteration for the NIR iteration are 0.3, 0.15 mW cm^{-2} μm^{-1} sr^{-1}, and 10, respectively.

TABLE 3. List of VIIRS ocean color products.

Name	Description	Product Type
$nL_w(\lambda)$	Normalized water-leaving radiances at VIIRS M1–M5 bands	Standard
Chl-a (OC3V)	Chl-a concentration using the OC3V algorithm	Standard
$K_d(490)$	Diffuse attenuation coefficient at the wavelength of 490 nm	Standard
K_d(PAR)	Diffuse attenuation coefficient at the domain associated with the PAR	Standard
L2 Flags	Level-2 data quality flags	Standard
Chl-a (OCI)	Chl-a concentration using the OCI algorithm	Experimental
$a(\lambda)$	Total absorption coefficient at VIIRS M1–M5 bands	Experimental
$a_{ph}(\lambda)$	Absorption coefficient of phytoplankton pigments at VIIRS M1–M5 bands	Experimental
$a_{dg}(\lambda)$	Absorption coefficient of gelbstoff and detritus at VIIRS M1–M5 bands	Experimental
$b_b(\lambda)$	Total backscattering coefficient at VIIRS M1–M5 bands	Experimental
$b_{bp}(\lambda)$	Backscattering coefficient of suspended particles at VIIRS M1–M5 bands	Experimental
PAR	Photosynthetically available radiation at ocean surface	Experimental

2.6. VIIRS Ocean Color Data Processing Streams

NOAA Ocean Color Team has been focusing on the "end-to-end" production of high quality satellite ocean color products. It has been shown that the operational IDPS-SDR has some considerable calibration issues (*Sun and Wang*, 2015c; 2016), which have significantly impacted the VIIRS ocean color data quality (*Wang, et al.*, 2016a; *Wang, et al.*, 2014; 2015a). Therefore, Ocean Color Team has put considerable efforts into on-orbit sensor calibration by re-examining and fixing errors in the current calibration methods, in particular, adding the effect of lunar

TABLE 4. List of VIIRS ocean color Level-2 flags. The flag bits used for default masking for Level-2 and Level-3 ocean color data processing are labeled "On" in the "L2 Mask Default" and "L3 Mask Default" column, respectively.

Bit	Name	Brief Description	L2 Mask Default	L3 Mask Default
00	ATMFAIL	Atmospheric correction failure		On
01	LAND	Pixel is over land	On	On
03	HIGLINT	Strong sun glint contamination		On
05	HITSATZEN	Sensor-zenith angle exceeds threshold		On
06	COASTZ	Pixel is over shallow water		
07	LANDADJ	Probable land-adjacent effect contamination		
09	CLOUD	Probable cloud contamination	On	On
11	TURBIDW	Turbid water detected		
12	HISOLZEN	Solar-zenith angle exceeds threshold		On
13	HITAU	High aerosol optical thickness		
14	LOWLW	Very low water-leaving radiance at green band		On
15	CHLFAIL	Chl-a algorithm failure		On
16	NAVWARN	Navigation quality is suspect		On
17	ABSAER	Absorbing aerosols detected		
18	CLDSHDSTL	Cloud straylight or shadow contamination		On
19	MAXAERITER	Maximum iterations reached for the NIR iteration		On
20	MODGLINT	Moderate sun glint contamination		
21	CHLWARN	Chl-a is out of range		On
22	ATMWARN	Atmospheric correction is suspect		
23	ALGICE	Sea ice pixel identified from $nL_w(\lambda)$ spectrum		
24	SEAICE	Sea ice pixel identified from ancillary files		
25	NAVFAIL	Navigation failure		On
29	FROMSWIR	Derived from the SWIR atmospheric correction		
31	OCEAN	Pixel is over ocean/water		

calibration (*Sun and Wang*, 2014; 2015a; b; c; 2016). With the improved sensor calibration using both the solar and lunar approaches, the science quality SDR data have been routinely processed from the RDR (or Level-0 data). The NOAA Ocean Color Team has successfully carried out global mission-long VIIRS ocean color data reprocessing from the RDR to SDR, and SDR to ocean color EDR.

For routine forwarding global data processing, in order to meet requirements from all users (e.g., operational, research, modeling, etc.), VIIRS ocean color data are processed in two types data streams as described below.

(1) The near-real-time (NRT) ocean color data products, which have the characteristics of (a) quick turn around with ~12-24 hours data latency, (b) using the standard/operational VIIRS SDR data (i.e., IDPS-SDR), (c) ancillary data using the Global Forecast System (GFS) model, and (d) global data may not be complete due to various issues.

(2) The science quality ocean color data products, which have the characteristics of (a) delayed about one-two weeks, (b) might using the improved SDR (science quality SDR), (c) science quality (assimilated) ancillary data from NCEP, (d) complete global coverage, and (e) reprocessed mission-long ocean color data and continue-forward data stream for consistency.

Therefore, the major advantage from the NRT data stream is a quick turn around in data latency that is useful for timely applications (e.g., ocean spatial variation and anomaly monitoring and characterization), while for the science quality data stream the important feature is its high accuracy and consistency that are necessary for scientific research and applications. It is noted that differences of ancillary data used in the NRT and science quality data streams are described in detail in *Ramachandran and Wang* (2011).

In the NRT data stream, the NIR atmospheric correction algorithm (Section 2.3.1) with the BMW NIR ocean reflectance correction algorithm (Section 2.3.4.2) is used. For the science quality data processing, three independent data streams are running with the NIR-BMW, SWIR (Section 2.3.2), and NIR-SWIR (Section 2.3.3) atmospheric correction algorithms, respectively. Since VIIRS SWIR bands still have sensor calibration issues, the SWIR and NIR-SWIR data streams are still experimental and for evaluation only. Therefore, the VIIRS ocean color product validations are mainly performed on the science quality NIR-BMW data stream. Figure 6 shows the VIIRS climatology (2012–2016) $nL_w(\lambda)$ at bands M1 to M5 (Figs. 6a–6e), Chl-a (Fig. 6f), K_d(490) (Fig. 6g), and K_d(PAR) (Fig. 6h) images of the global ocean in the science quality NIR-BMW data stream.

2.7. Algorithm Validation

In this section, we provide some algorithm evaluation and validation results, which mainly compared satellite results with those from in situ measurements. Some detailed data analysis (e.g., from statistics comparison and analysis) is also provided. Evaluation and validation results are mostly focused on the VIIRS standard ocean color products. In addition, for effective evaluations of VIIRS ocean color data quality, global Level-3 VIIRS 8-day ocean color data over oligotrophic and deep waters are compared with those from MODIS-Aqua, showing the two data sets are generally consistent. MODIS-Aqua data are downloaded directly from the NASA Ocean Biology Processing Group (OBPG) website. As discussed before, algorithm validation results from MODIS can generally also be applied to VIIRS.

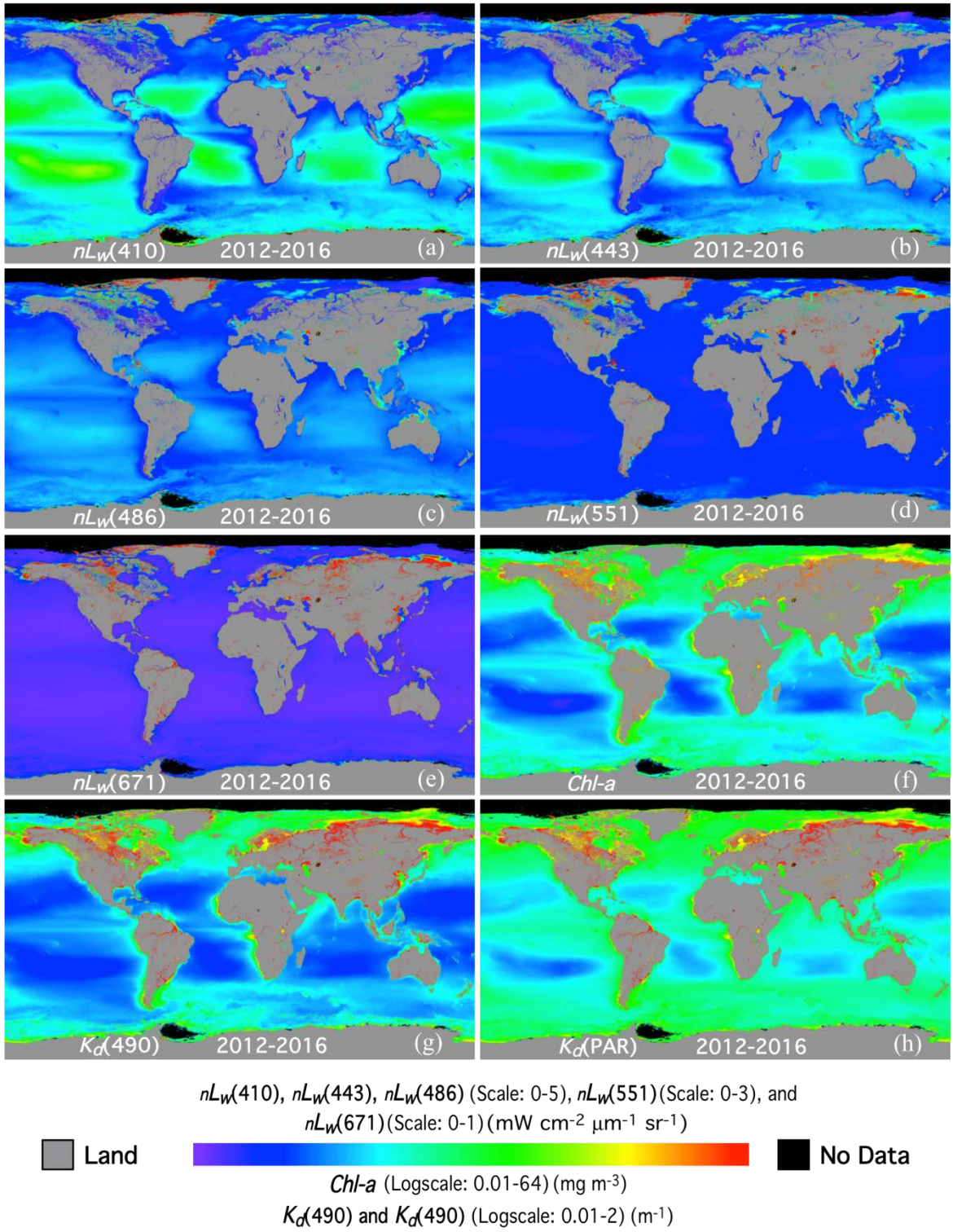

Figure 6. VIIRS climatology (2012–2016) $nL_w(\lambda)$ at M1–M5 bands, Chl-a, $K_d(490)$, and $K_d(PAR)$ images of the global ocean of the NIR-based (BMW) science quality data stream.

2.7.1. Routine data monitoring using MOBY in situ data

In situ hyperspectral radiometric data measured at the MOBY site (*Clark, et al.*, 1997) moored off the island of Lanai in Hawaii (http://moby.mlml.calstate.edu/MOBY-data) are routinely used to monitor VIIRS ocean color EDR products (*Wang, et al.*, 2015b). The MOBY program (currently funded by NOAA) has been providing consistently high-quality clear-ocean hyperspectral optics data since 1997, supporting the vicarious calibration for various satellite ocean color missions (*Eplee Jr., et al.*, 2001; *Franz, et al.*, 2007; *Gordon*, 1998; *Wang and Gordon*, 2002; *Wang, et al.*, 2016c), e.g., SeaWiFS, MODIS, MERIS, VIIRS, etc. To monitor, evaluate, and assess VIIRS SDR and ocean color EDR products, in situ $nL_w(\lambda)$ measurements at the VIIRS-spectrally-weighted bands, i.e., at VIIRS nominal center wavelengths of 410, 443, 486, 551, and 671 nm from January 2012 to the present are routinely obtained from the NOAA CoastWatch website (http://coastwatch.noaa.gov/moby/). In addition to the vicarious calibration, it is particularly useful to monitor and evaluate the VIIRS on-orbit calibration performance and stability of the SDR and OC EDR by comparing VIIRS-derived $nL_w(\lambda)$ with those from MOBY in situ measurements (*Wang, et al.*, 2016a; *Wang, et al.*, 2014; 2015a; *Wang, et al.*, 2013b; *Wang, et al.*, 2015b).

For matchup comparison, VIIRS-measured $nL_w(\lambda)$, Chl-a, and $K_d(490)$ data were extracted from Level-2 data files using an 5×5 box centered at the location of in situ measurements, following the matchup procedure outlined by *Wang et al.* (2009b). For Chl-a and $K_d(490)$ comparisons, MOBY in situ $nL_w(\lambda)$ data were used to derive Chl-a and $K_d(490)$ data using the same VIIRS OC3V Chl-a and $K_d(490)$ algorithms in the MSL12 ocean color data processing. Time series of the MSL12-derived VIIRS $nL_w(\lambda)$, Chl-a, and $K_d(490)$ data, corresponding to MOBY in situ measurements, are constructed and compared with those from in situ data for assessments of the VIIRS observations. Figure 7 provides time series of MSL12-derived Chl-a, $K_d(490)$, and $nL_w(\lambda)$ at wavelengths of 410 nm (M1), 443 nm (M2), 486 nm (M3), 551 nm (M4), and 671 nm (M5) compared with those from MOBY in situ measurements (from the top to the bottom rows) for the VIIRS-SNPP period of January 1, 2012 to April 24, 2017. It is noted that, for MOBY in situ data, both quality-I (Q1, high quality data) and quality-II (Q2, data may have some quality issues) are used. MOBY high quality optics data (Q1 data with red dots) are used for vicarious calibration, but Q2 data (black dots) can also be used for product monitoring purpose as shown in Fig. 7. It is noted again that MOBY Chl-a and $K_d(490)$ data are derived from MOBY in situ optics data using the same VIIRS Chl-a and $K_d(490)$ algorithms. Results in Fig. 7 show that the MSL12-derived VIIRS $nL_w(\lambda)$ data generally correspond well to MOBY in situ values in most of wavelengths. The recently reprocessed (April 2017) science quality ocean color EDR data are compared with MOBY in situ measurements, and the results are provided in Table 5. Table 5 shows VIIRS-derived ocean color products compared with MOBY in situ data for both ratio values and difference values, showing that comparisons are excellent. For relatively high values (e.g., $nL_w(\lambda)$ at the blue bands), the ratio values can provide valid comparisons, while for low values (e.g., $nL_w(\lambda)$ at the red band) the difference comparisons should be used. It should be particularly noted that MOBY in situ data are used for data variation monitoring and assessment, and not for the ocean color data validation.

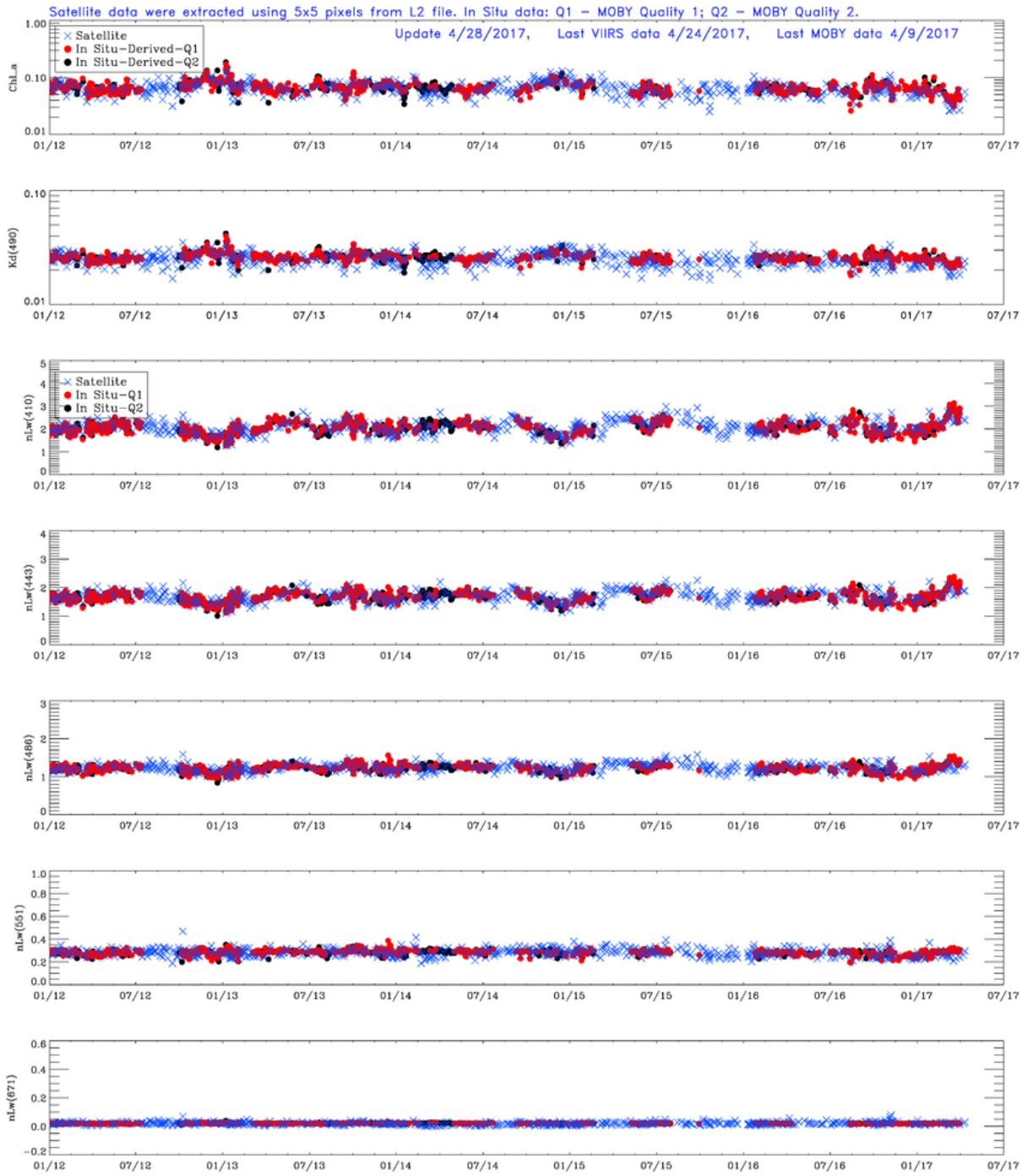

Figure 7. Comparisons of VIIRS-derived ocean color products (blue crosses) with MOBY in situ data (derived routinely), with the red and black dots in MOBY data corresponding to quality-I (Q1) and quality-II (Q2), respectively.

TABLE 5. Average (AVG), standard deviation (STD), and number of data (Num) for the ratio and difference between VIIRS ocean color data (science quality) and MOBY in situ data for $nL_w(\lambda)$ at VIIRS M1–M5 bands, as well as derived Chl-a and $K_d(490)$. Difference in percent (Diff (%)) is also provided. VIIRS ocean color products are from the latest data reprocessing in April 2017.

Product	Ratio (VIIRS/In Situ)				Difference (VIIRS–In Situ)			
	AVE	MED	STD	Num	AVE	MED	STD	Diff (%)
$nL_w(410)$	1.0179	1.0153	0.096	557	0.0264	0.0329	0.190	1.29
$nL_w(443)$	1.0159	1.0119	0.092	557	0.0196	0.0181	0.150	1.18
$nL_w(486)$	1.0164	1.0124	0.088	557	0.0151	0.0153	0.105	1.24
$nL_w(551)$	1.0276	1.0098	0.135	557	0.0062	0.0029	0.037	2.17
$nL_w(671)$	1.1219	1.0045	0.498	527	0.0021	0.0001	0.010	10.04
Chl-a	1.0265	1.0036	0.168	557	0.0013	0.0002	0.011	1.86
$K_d(490)$	0.9941	0.9846	0.101	557	–0.0002	–0.0004	0.003	–0.77

2.7.2. Routine data monitoring and evaluation using AERONET-OC in situ data

Aerosol Robotic Network (AERONET) program is a federation of ground-based remote sensing aerosol networks, which is developed to sustain atmospheric studies at various scales with measurements from worldwide distributed autonomous sun-photometers (*Holben et al.*, 1998). AERONET–Ocean Color (AERONET-OC) is an extension to the AERONET program to support marine applications (*Zibordi et al.*, 2009). AERONET-OC provides the additional capability of measuring the radiance emerging from the sea/water (i.e., water-leaving radiance) with modified sun-photometers installed on offshore platforms like lighthouses, oceanographic and oil towers. AERONET-OC is instrumental in satellite ocean color validation activities through standardized measurements of (a) performed at different sites with a single measuring system and protocol, (b) calibrated with an identical reference source and method, and (c) processed with the same code.

NOAA has been supporting operations of three AERONET-OC stations for VIIRS ocean color product validation: Wave-Current Information System (CSI), Long Island Sound Coastal Observatory (LISCO), and University of Southern California (USC). Recently, NOAA has also supported to establish a new AERONET-OC site in Lake Erie. In situ $nL_w(\lambda)$ measurements from the three AERONET-OC sites at about the VIIRS bands, i.e., at wavelengths of 410, 443, 486, 551, and 671 nm from January 2012 to the present are used to evaluate and validate VIIRS-measured $nL_w(\lambda)$ spectra data. Same as MOBY matchup comparison, VIIRS-measured $nL_w(\lambda)$ data were extracted from OC EDR data files using an 5×5 box centered at the location of AERONET-OC stations, following the matchup procedure outlined by *Wang et al.* (2009b). Table 6 provides quantitative comparison between VIIRS and AERONET-OC in situ data. It can be seen that the VIIRS-derived $nL_w(\lambda)$ are almost perfect matches to the in situ measurements at the USC station, while they are somewhat overestimated for the short blue bands at the CSI and

LISCO sites. It is noted that the three AERONET-OC stations are all close to the coast, thus the ocean color measurements at these stations represent coastal or Case-2 waters.

TABLE 6. Average (AVG), standard deviation (STD), and number of data (Num) for the ratio and difference between VIIRS ocean color data (science quality) and in situ data from the three AERONET-OC sites (CSI, LISCO, and USC) for $nL_w(\lambda)$ at VIIRS M1–M5 bands. Difference in percent (Diff (%)) is also provided. VIIRS ocean color products are from the latest data reprocessing in April 2017.

Site	OC Product	Ratio (VIIRS/In Situ)				Difference (VIIRS–In Situ)			
		AVE	MED	STD	Num	AVE	MED	STD	Diff (%)
CSI	$nL_w(410)$	1.291	1.107	0.891	248	0.072	0.027	0.256	19.32
	$nL_w(443)$	1.222	1.099	0.516	248	0.077	0.044	0.218	15.05
	$nL_w(486)$	1.101	1.065	0.302	248	0.039	0.035	0.217	4.82
	$nL_w(551)$	1.064	1.031	0.227	248	0.023	0.027	0.218	2.36
	$nL_w(671)$	1.264	1.209	0.387	248	0.037	0.031	0.070	17.47
LISCO	$nL_w(410)$	1.445	0.872	1.734	318	0.044	–0.030	0.279	20.22
	$nL_w(443)$	1.010	0.834	0.640	325	–0.009	–0.053	0.211	–2.42
	$nL_w(486)$	0.811	0.757	0.315	325	–0.141	–0.160	0.187	–19.51
	$nL_w(551)$	0.867	0.843	0.235	325	–0.144	–0.158	0.176	–14.10
	$nL_w(671)$	0.708	0.754	0.340	325	–0.075	–0.069	0.088	–26.74
USC	$nL_w(410)$	1.092	1.021	0.398	363	0.045	0.014	0.233	6.07
	$nL_w(443)$	1.042	0.999	0.276	363	0.021	–0.001	0.168	2.83
	$nL_w(486)$	0.979	0.965	0.167	363	–0.018	–0.027	0.115	–2.40
	$nL_w(551)$	0.925	0.909	0.155	363	–0.034	–0.033	0.060	–8.80
	$nL_w(671)$	0.640	0.578	0.470	360	–0.017	–0.016	0.019	–40.25

2.7.3. Validation of the SWIR and NIR-SWIR atmosphere correction algorithms

Figure 8 shows a sample image along the U.S. east coast region generated by *Wang and Shi* (2007) using three algorithms: NIR-, SWIR-, and NIR-SWIR-based atmospheric correction algorithms. Results in the top panel of Figs. 8(a)–8(d) are MODIS-Aqua-derived Chl-a and $nL_w(\lambda)$ at wavelengths of 443 nm ($nL_w(443)$), 531 nm ($nL_w(531)$), and 667 nm ($nL_w(667)$), respectively, which were obtained using the standard-NIR data processing approach. Figures 8(e)–8(h) (the middle panel) are results corresponding to the same parameters derived using the SWIR atmospheric correction method, while images in Figs. 8(i)–8(l) (the bottom panel) are the corresponding results using the NIR-SWIR combined data processing approach. Judging the results by examining overall image quality (e.g., data smoothness, number of missing data, etc.), Fig. 8 shows that, while the standard-NIR method produces good quality ocean color products further offshore, the standard data processing outputs results with noticeable noise and significant missing data in the coastal regions, e.g., regions in and/or around the Chesapeake

Bay, Outer Banks, and Delaware Bay. Alternatively, results in Figs. 8(e)–8(h) show that the SWIR algorithm can significantly improve ocean color products in coastal near-shore regions, but further offshore there is substantial noise and data dropout in the derived products, e.g., results from regions around the northern Delaware Bay. Thus, the advantages of using the NIR-SWIR combined method for the MODIS-Aqua ocean color data processing are readily demonstrated in Figs. 8(i)–8(l). The NIR-SWIR method has not only produced improved ocean color products in near-shore coastal regions, it has also preserved the high quality data products in further offshore. Similar results are routinely obtained from VIIRS-SNPP measurements using the NIR-, SWIR-, and NIR-SWIR-based atmospheric correction algorithms.

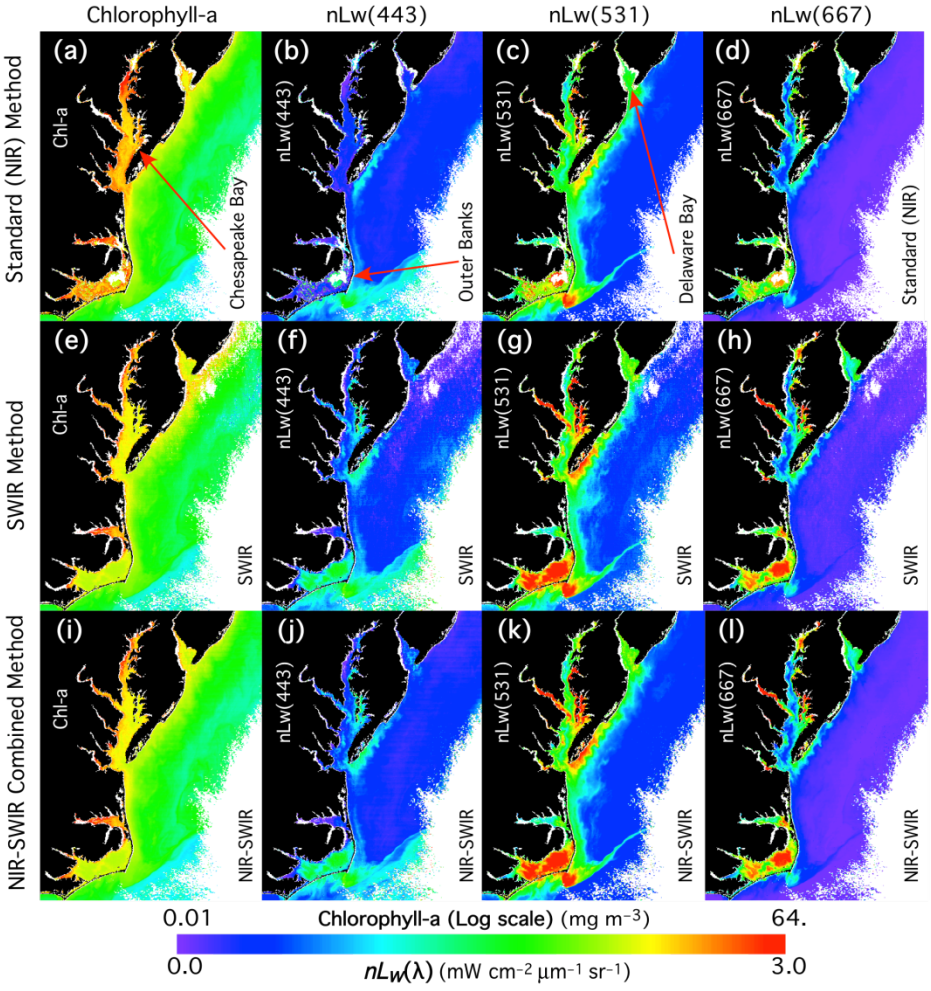

Figure 8. MODIS-Aqua measurements acquired along the U.S. east coast region on April 5, 2004 for the images of Chl-a, $nL_w(443)$, $nL_w(531)$, and $nL_w(667)$, respectively. Panels (a)–(d) are results from the standard-NIR method; panels (e)–(h) are results from the SWIR method; and panels (i)–(l) are results from the NIR-SWIR combined method. These are reproduced from *Wang and Shi* (2007).

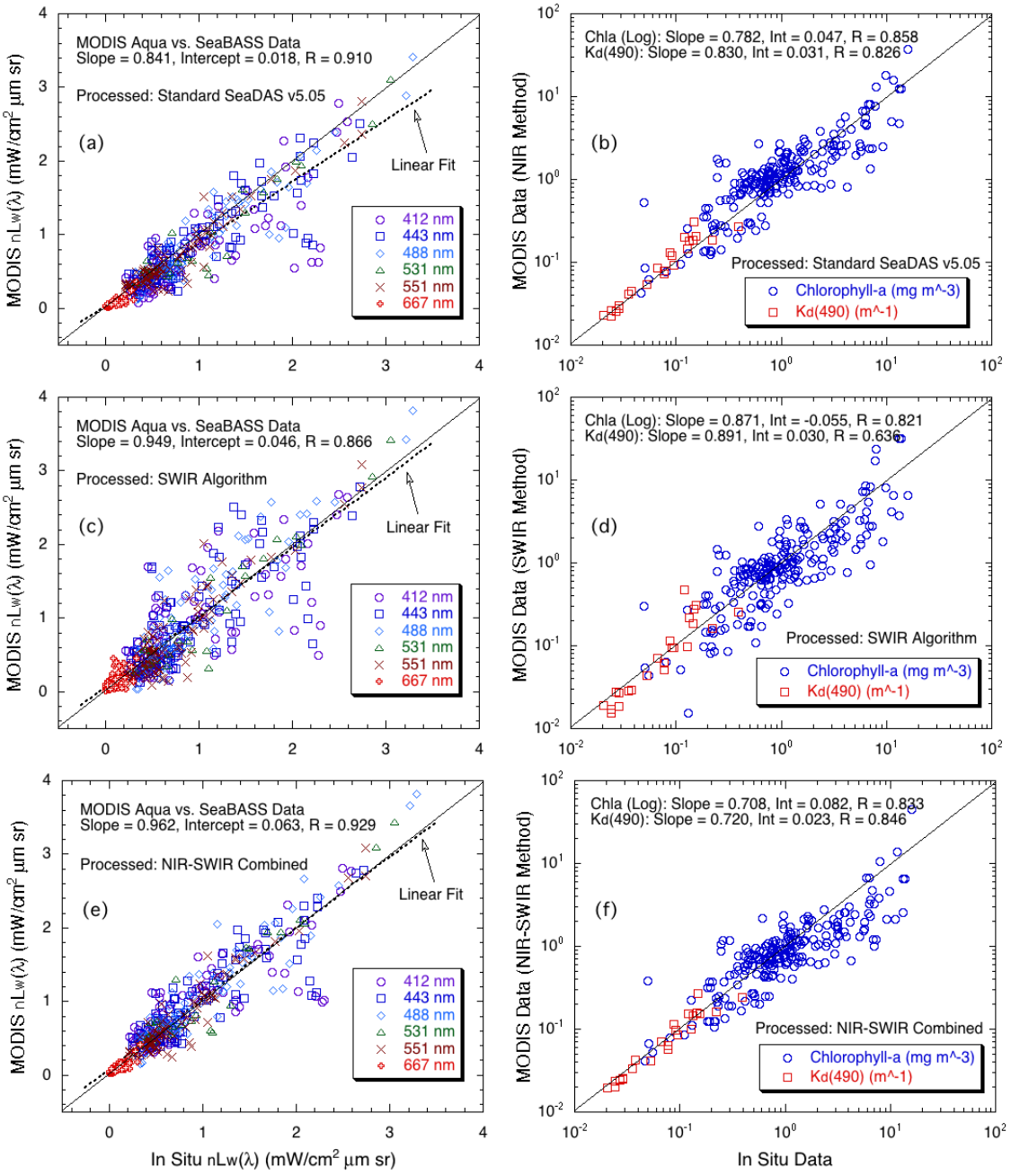

Figure 9. MODIS-Aqua-derived $nL_w(\lambda)$, Chl-a, and $K_d(490)$ data compared with in situ measurements using (a) and (b) the NIR algorithm, (c) and (d) the SWIR algorithm, and (e) and (f) the NIR-SWIR combined method. They are reproduced from *Wang et al.* (2009b).

Using the NASA maintained ocean optical and biological in situ data that were collected during 2002–2005 (*Werdell and Bailey*, 2005), *Wang et al.* (2009b) evaluated the performance of atmospheric correction algorithms for the ocean color products from MODIS-Aqua. Specifically, algorithms using the SWIR bands and NIR-SWIR combined method are evaluated, compared to the matchup results from the standard NIR-based algorithm. Figure 9 shows the comparison between the MODIS-Aqua-derived and in situ measured ocean color products for various cases. The ocean color products included in these results are $nL_w(\lambda)$ at MODIS wavelengths of 412, 443, 488, 531, 551, and 667 nm, Chl-a, and $K_d(490)$. Figures 9(a), 9(c), and 9(e) show $nL_w(\lambda)$ comparisons, while Figs. 9(b), 9(d), and 9(f) are evaluations for Chl-a and $K_d(490)$. Figures 9(a), 9(c), and 9(e) are MODIS-Aqua-derived $nL_w(\lambda)$ results compared with the in situ measurements, corresponding to cases for which MODIS-Aqua data are processed using the standard-NIR, SWIR, and NIR-SWIR combined atmospheric correction algorithm, respectively. Figures 9(b), 9(d), and 9(f) are results of the Chl-a and $K_d(490)$ matchups corresponding to MODIS-Aqua data processed with the three different algorithms.

For $nL_w(\lambda)$ results, the slopes of the overall match-ups using the SWIR and NIR-SWIR methods (Figs. 9(c) and 9(e)) have been improved compared with those using the standard-NIR method (Fig. 9(a)). However, the SWIR method produced increased product noise (*Wang and Shi*, 2012), which can be seen in Fig. 9 and is also indicated from the reduced correlation coefficient for the match-ups. The slopes in the overall $nL_w(\lambda)$ match-ups for the standard-NIR, SWIR, and NIR-SWIR methods are 0.841, 0.949, and 0.962 with their corresponding correlation coefficients of 0.910, 0.866, and 0.929, respectively. The data noise produced by the SWIR method is due mainly to the substantially lower sensor signal-to-noise ratio (SNR) values for the MODIS SWIR bands (*Wang and Shi*, 2012) and also because of SWIR algorithm performance errors (*Wang*, 2007). Similar results are also shown for Chl-a and $K_d(490)$ matchup comparisons (Figs. 9(b), 9(d), and 9(f)); in particular, results from the SWIR method show lower correlation coefficient values.

The standard-NIR, SWIR, and NIR–SWIR algorithm performances are further evaluated with the MODIS-Aqua global ocean color product data. Figure 10 provides color images for global composite distributions of MODIS-Aqua Chl-a and $nL_w(443)$ for the month of July 2005, which were derived using the NIR-, SWIR-, and NIR-SWIR-based atmospheric correction algorithms from MODIS-Aqua global measurements. Figures 10(a), 10(c), and 10(d) are color images of Chl-a for MODIS-Aqua data that were processed using the NIR, SWIR, and NIR-SWIR method, respectively, while Figs. 10(b), 10(d), and 10(f) are the corresponding $nL_w(443)$ images from the three different data processing methods. The product images for the NIR method (Figs. 10(a) and 10(b)) were downloaded directly from the NASA ocean color website, while results of the SWIR and NIR-SWIR combined methods (Figs. 10(c)–10(f)) were generated from the MODIS-Aqua Level-1B data (July of 2005) using the SWIR and NIR-SWIR method, respectively. These images compare the global spatial variations of the ocean color products (Chl-a and $nL_w(443)$) that were derived from three different methods. It is noted that there is a solar-zenith angle cut off at 70° for all three data processing methods. Results in Fig. 10 show that, for the most of ocean regions, all three methods produced similar monthly Chl-a and $nL_w(443)$ data distributions. However, Fig. 10 shows some obvious differences in MODIS-Aqua-

derived Chl-a and $nL_w(443)$ from three methods. Both SWIR and NIR-SWIR methods show some improved data coverage, e.g., along the China east coastal region, while the SWIR method produced some obvious different results in some open ocean regions, e.g., in the southern ocean. Judging data quality by their coverage, spatial continuity, and image smoothness, it appears that the NIR-SWIR method produced the best Chl-a and $nL_w(443)$ results.

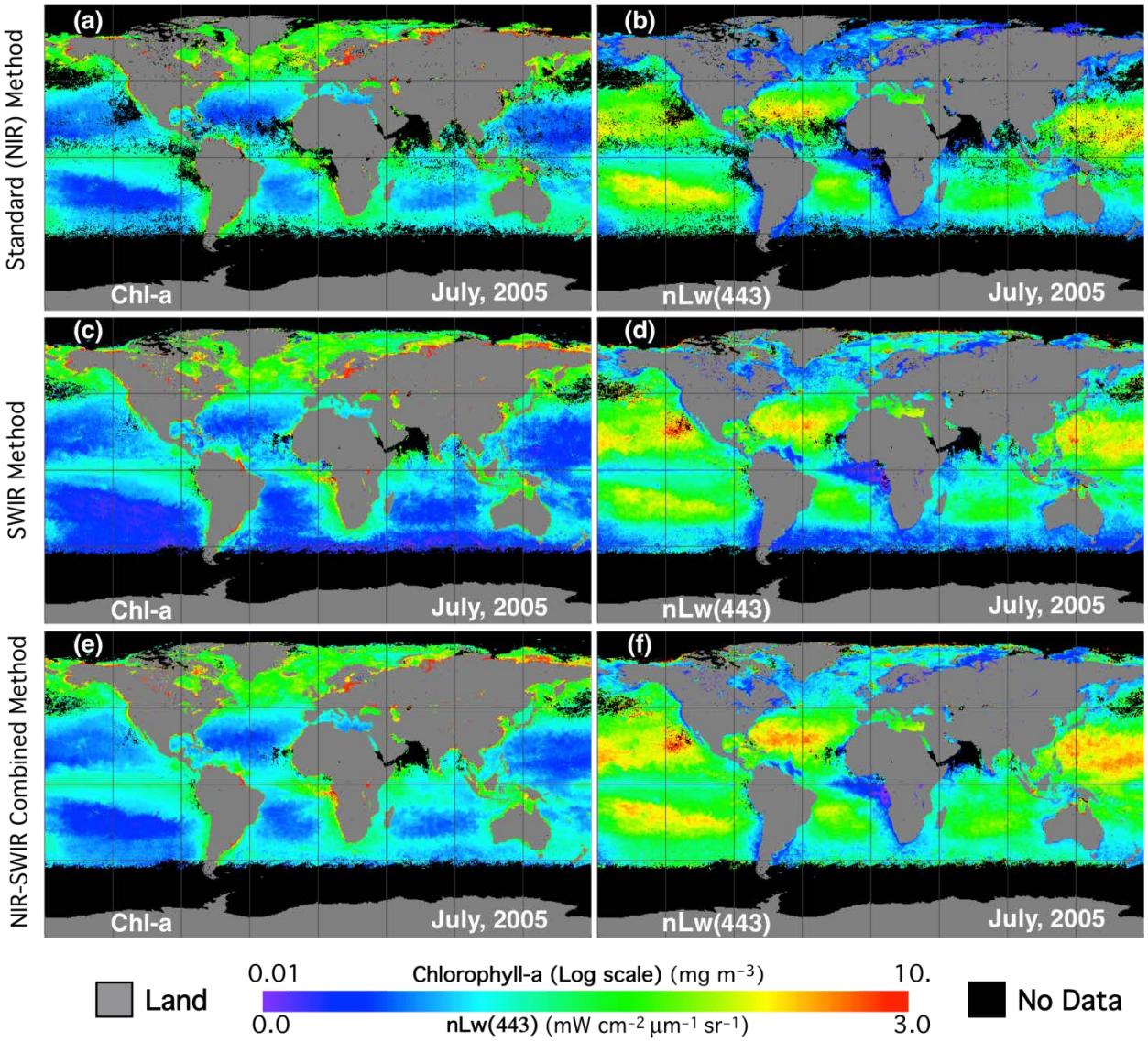

Figure 10. Color images for the global composite distribution of the MODIS-Aqua-derived Chl-a and $nL_w(443)$ for the month of July 2005, which were retrieved using (a) and (b) the NIR algorithm, (c) and (d) the SWIR method, and (e) and (f) the NIR-SWIR combined method. These are reproduced from *Wang et al.* (2009b).

2.7.4. Evaluation of the BMW algorithm

The BMW algorithm for the NIR ocean reflectance correction was implemented in the MSL12 ocean color data processing package to improve the ocean color data quality over coastal and inland waters (*Jiang and Wang*, 2014). The BMW algorithm combines the advantages of the three NIR ocean reflectance correction algorithms, i.e., *Bailey et al.* (2010) algorithm, *Ruddick et al.* (2000) algorithm, and *Wang et al.* (2012) algorithm. Detailed algorithm evaluation results are reported in *Jiang and Wang* (2014). Essentially, ocean color results from several NIR ocean reflectance correction algorithms (*Bailey, et al.*, 2010; *Jiang and Wang*, 2014; *Ruddick, et al.*, 2000; *Stumpf, et al.*, 2003; *Wang, et al.*, 2012) are compared with those from the SWIR-based atmospheric correction algorithms from both MODIS-Aqua and VIIRS-SNPP measurements over turbid coastal and inland regions, including the U.S. east coast region, China east coast region, La Plata River estuary, and Lake Taihu (*Jiang and Wang*, 2014). In fact, evaluation results show that the BMW NIR reflectance correction algorithm can produce the most consistent results with those from the SWIR-based algorithms in turbid coastal and inland waters. In less turbid waters, e.g., over the U.S. east coast region, the BMW has produced results with the data quality comparable to the NASA operational algorithm, i.e., *Bailey et al.* (2010). Specifically, the BMW algorithm may be applicable to waters with the VIIRS NIR $nL_w(862)$ up to ~1.5–2.0 mW cm^{-2} μm^{-1} sr^{-1}, and the SWIR algorithm with the SWIR 1240 nm band can be used in regions with $nL_w(862)$ up to ~2.0–2.5 mW cm^{-2} μm^{-1} sr^{-1}. For extremely turbid waters with $nL_w(862)$ > ~2.5 mW cm^{-2} μm^{-1} sr^{-1}, the SWIR atmospheric correction algorithm must be used with the combination of the atmospheric correction bands at two longer SWIR wavelengths, i.e., 1601 and 2257 nm for VIIRS (*Jiang and Wang*, 2014).

2.7.5. Validation of Chl-a algorithm

VIIRS Chl-a data are derived using the OC3V algorithm (Eq. (11), which is tuned to the VIIRS spectral bands using the empirical blue-green reflectance ratio algorithms developed for SeaWiFS and MODIS (*O'Reilly, et al.*, 1998; *O'Reilly, et al.*, 2000). Figure 11 compares the VIIRS-SNPP-derived Chl-a values using Eq. (11) to the in situ-measured data, which are obtained from the NASA SeaWiFS Bio-optical Archive and Storage System (SeaBASS) database. Chl-a comparison results include VIIRS/in situ matchup time differences within 3-hour (Fig. 11(a)) and 1-day (Fig. 11(b)). Results of the VIIRS/in situ matchup time difference within 1-day are included in order to have more matchup points. Matchup statistics values (mean, median, STD, and number of data) are indicated in each plot. It should be noted that in situ SeaBASS Chl-a data are acquired during the VIIRS-SNPP period (2012–present) from various regions, including the California Coast, Gulf of Maine, Massachusetts Coast, Chesapeake Bay, and Florida Coast. In fact, in situ Chl-a value ranges from ~0.09 to ~40 mg m^{-3} (Fig. 11), covering relatively clear oceans to highly productive coastal waters. Results in Fig. 11 show that VIIRS-derived Chl-a data are compared quite well with the in situ measurements. The mean and median ratios of VIIRS-derived Chl-a versus in situ data are 1.299 and 1.142 with STD of 0.624 for matchup time difference within 3-hour (Fig. 11(a)), while mean and median ratios are 1.180 and 0.982 with SDT of 0.674 for matchup time difference within 1-day (Fig. 11(b)). Results in Fig. 11 show that VIIRS-derived Chl-a data are quite reasonable compared with the in situ

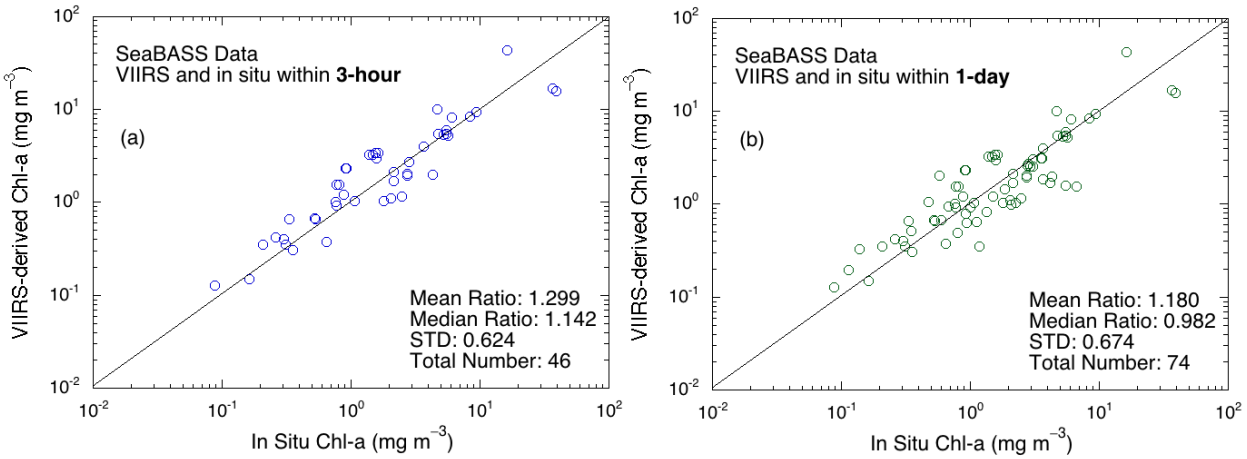

Figure 11. Comparison results of VIIRS-derived Chl-a data with the in situ measurements from the SeaBASS database using the OC3V Chl-a algorithm (Eq. (11)) for cases of the time difference between VIIRS and in situ measurements within (a) 3-hour and (b) 1-day.

measurements. Errors in VIIRS-derived Chl-a data are all within 30%, and most of Chl-a data are much more accurate, e.g., median ratios of 0.982–1.142 or median errors within ~2–14%. However, it should be particularly noted that, for the CDOM-dominated waters (e.g., along the west coast of Florida), satellite Chl-a algorithm (the blue-green reflectance ratio algorithm) still have some significant issues, i.e., deriving biased high Chl-a data (*Le et al.*, 2013).

2.7.6. Validation of $K_d(490)$ algorithm

VIIRS $K_d(490)$ data are derived using the *Wang et al.* (2009a) algorithm, which was developed using MODIS-Aqua and in situ data. Figure 12 compares the model-derived $K_d(490)$ values using Eq. (12) and in situ-measured data (*Wang, et al.*, 2009a). Note that the model $K_d(490)$ data were derived using Eq. (12) with the in situ-measured reflectance data from the NASA SeaBASS data set. In Fig. 12, two sets of the in situ $K_d(490)$ data (all from SeaBASS), one from the Chesapeake Bay region and another from global non-Chesapeake Bay data, are used. The Chesapeake Bay $K_d(490)$ data have generally high values ranging from 0.4–5 m^{-1}, while the non-Chesapeake Bay in situ data have $K_d(490)$ values ranging from 0.02–3.7 m^{-1} covering deep clear oceans (e.g., oligotrophic waters) to some coastal turbid waters. Results in Fig. 12 show that satellite-derived $K_d(490)$ data are quite reasonable compared with the in situ measurements, with mean ratio of 1.037. To understand VIIRS $K_d(490)$ performance, Figs. 13(a), 13(b), 13(e), and 13(f) compare VIIRS-derived $K_d(490)$ with those from MODIS-Aqua in the U.S. east coast regions for both summer 2012 (June–August 2012) and winter 2013 (December 2012–February 2013), showing both VIIRS and MODIS producing almost identical $K_d(490)$ results. Thus, VIIRS-SNPP and MODIS-Aqua are producing consistent $K_d(490)$ data. Some detailed validation results for MODIS-Aqua can also be found in *Wang et al.* (2009a).

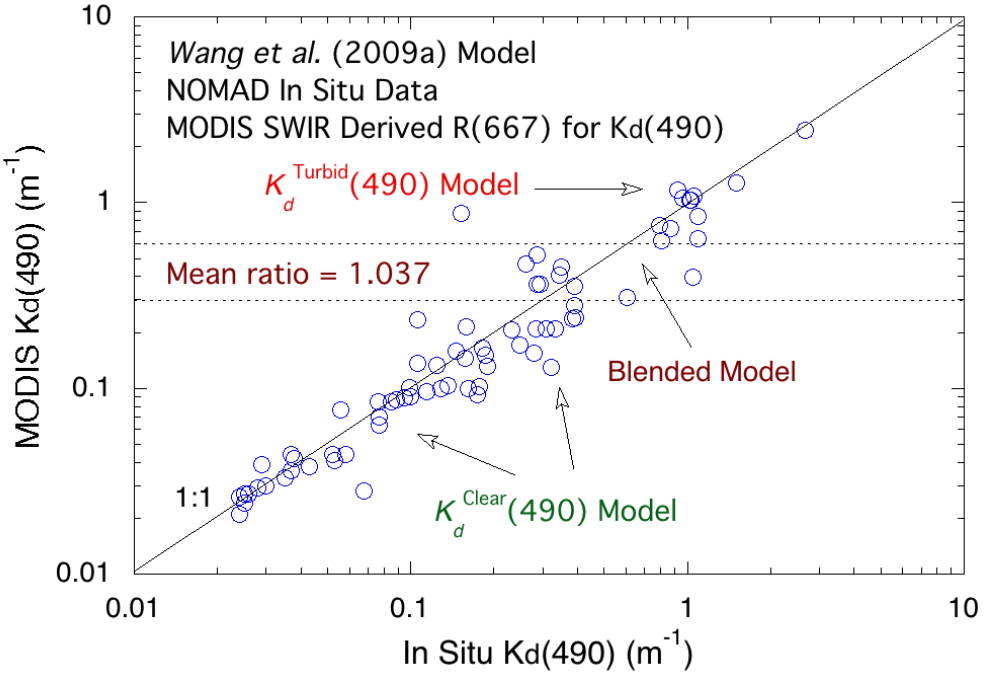

Figure 12. Comparisons of MODIS-Aqua-derived K_d(490) data with the in situ measurements from the global SeaBASS data (excluding the Chesapeake Bay) using the *Wang et al.* (2009a) K_d(490) algorithm (Eq. (12)). Note that MODIS data were processed using MSL12. These are reproduced from *Wang et al.* (2009a).

2.7.7. Validation of K_d(PAR) algorithm

Son and Wang (2015) compared the MODIS-Aqua-derived K_d(PAR) values using Eq. (17) and in situ measured data from SeaBASS data set and the Chesapeake Bay Program Water Quality database from 2002–2009. Figure 14 provides the MODIS-Aqua-derived K_d(PAR) data using the combined K_d(PAR) model (Eq. (17)) with in situ K_d(PAR) measurements covering various water properties from the global ocean (including coastal regions) (*Son and Wang*, 2015). The comparison results show that MODIS-Aqua-derived K_d(PAR) data are well matched to the in situ K_d(PAR) measurements with mean ratio, median ratio, and STD of 1.132, 1.044, and 0.496, respectively. Indeed, satellite derived K_d(PAR) data compare well with in situ data (mean and median ratios of 1.044 and 1.132 between these two or errors ~4–13%) for the in situ data range of 0.04–3.27 m^{-1} (Fig. 14). Again, in order to show VIIRS K_d(PAR) performance, VIIRS-derived K_d(PAR) data (Figs. 13(c) and 13(d)) are compared with those from MODIS-Aqua (Figs. 13(g) and 13(h)) in the U.S. east coast regions for both summer 2012 (June–August 2012) and winter 2013 (December 2012–February 2013). Both VIIRS and MODIS produce almost identical K_d(PAR) results over the U.S. east coastal region for two different seasons. Therefore, VIIRS can produce consistent K_d(PAR) data as those from MODIS-Aqua. Some detailed validation results can also be found in *Son and Wang* (2015).

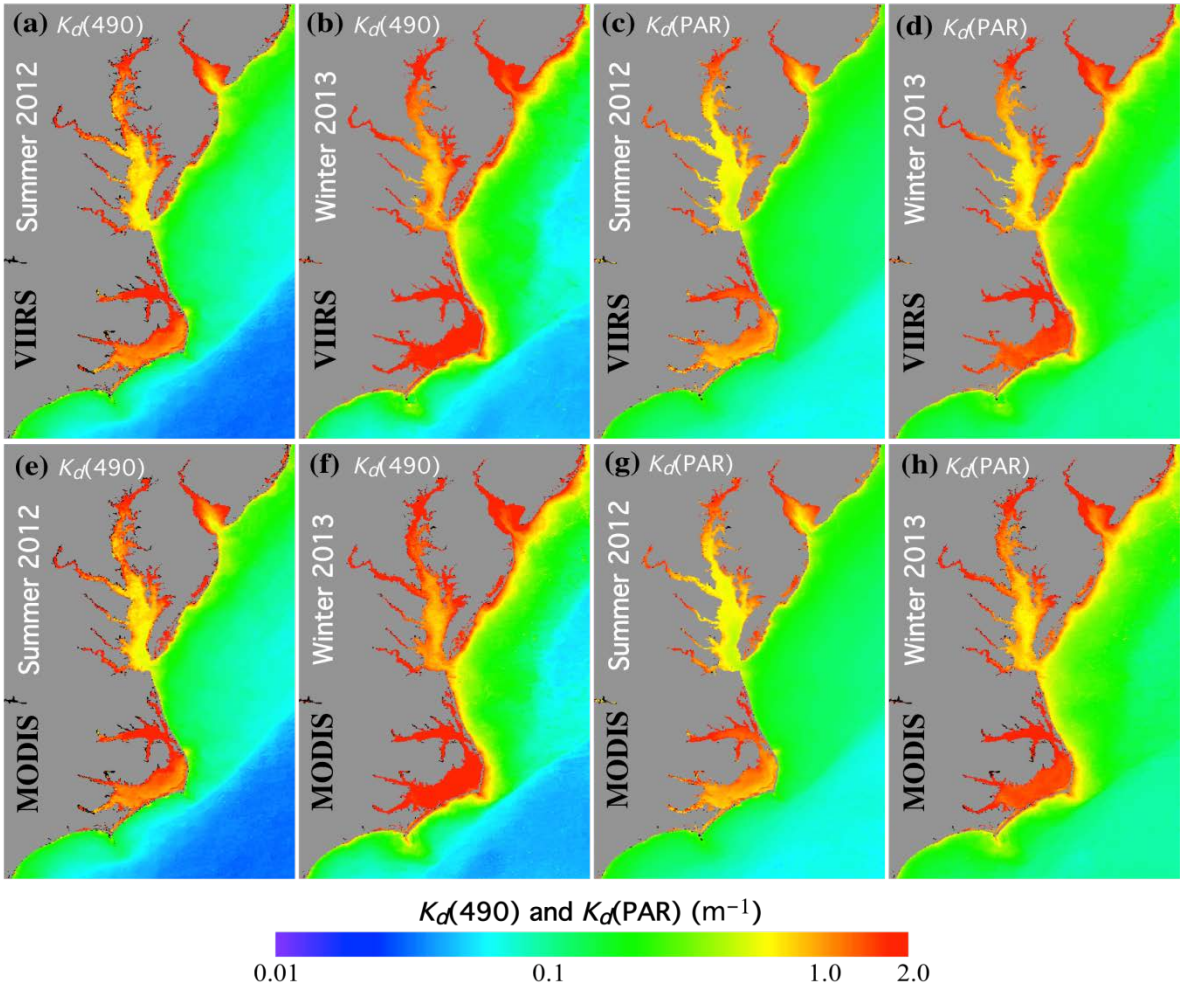

Figure 13. Seasonal composite images of VIIRS-derived K_d(490) and K_d(PAR) compared with those from MODIS-Aqua over the U.S. east coast region. Panels (a) and (b) are VIIRS-derived K_d(490) for summer 2012 and winter 2013, (c) and (d) VIIRS-derived K_d(PAR) for summer 2012 and winter 2013, (e) and (f) MODIS-derived K_d(490) for summer 2012 and winter 2013, and (g) and (h) MODIS-derived K_d(PAR) for summer 2012 and winter 2013. The summer 2012 is for June–August 2012 and winter 2013 is for December 2012–February 2013. Note that VIIRS and MODIS data are both derived using MSL12.

2.7.8. Implementation of the OCI algorithm for VIIRS Chl-a data

Performance of the OCI-based Chl-a algorithm has been well established, in particular, over oligotrophic waters (*Hu, et al.*, 2012; *Wang and Son*, 2016). In fact, results in Fig. 5 have conclusively shown that the OCI-based Chl-a algorithm performed much better than that from OC3V Chl-a algorithm over oligotrophic waters. *Wang and Son* (2016) have developed an effective implementation approach using the OCI-based Chl-a algorithm for VIIRS-SNPP. Specifically, using the VIIRS-SNPP-measured global Chl-a data derived from the MSL12 ocean color data processing system, *Wang and Son* (2016) have developed the CI-based algorithm

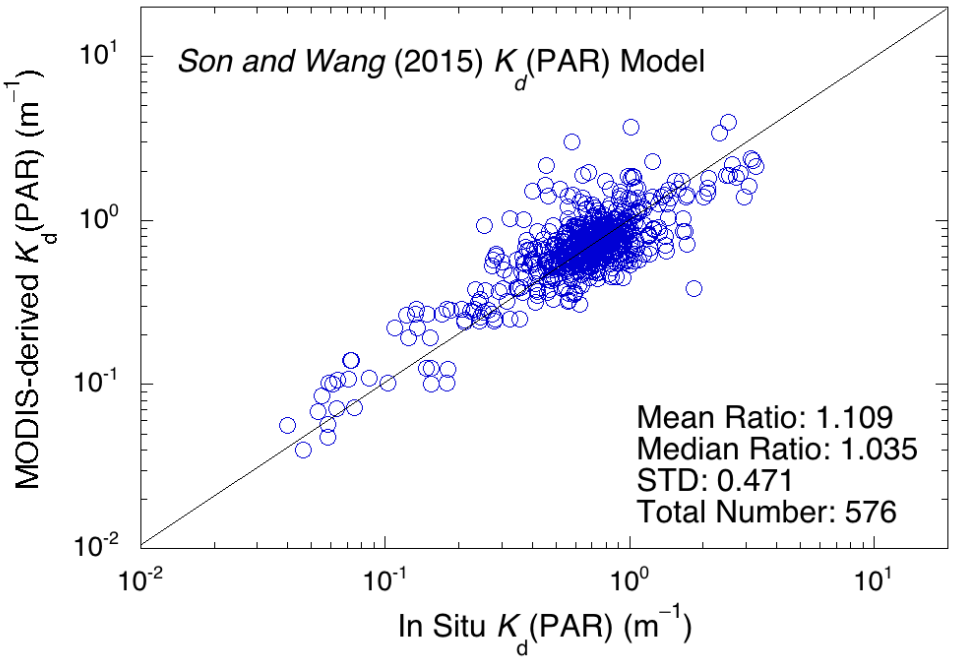

Figure 14. Matchup comparison results of MODIS-Aqua-derived K_d(PAR) data with the in situ measurements from the SeaBASS and the Chesapeake Bay Program Office Database using the *Son and Wang* (2015) K_d(PAR) algorithm (Eq. (17)). Note that MODIS data were processed using MSL12. These are reproduced from *Son and Wang* (2015).

specifically for VIIRS, and further improved the two Chl-a algorithms merging method using the blue-green reflectance ratio values. Extensive evaluation results show that the new OCI Chl-a algorithm for VIIRS can produce consistent Chl-a data compared with those from the OC3V algorithm. In particular, the data transition between the CI-based and OC3V-based Chl-a algorithm is quite smooth, and there are no obvious discontinuities in VIIRS-derived Chl-a data. The new OCI-based Chl-a algorithm has been implemented in MSL12 for routine production of VIIRS global Chl-a data (*Wang and Son*, 2016).

2.7.9. Other validation efforts

In situ validation of satellite data is essential to produce high-quality remotely sensed ocean color products. NOAA/STAR scientists have been collecting in situ data throughout all the ocean color satellite missions. Since the launch of the VIIRS-SNPP in October 2011, as part of the U.S. Joint Polar Satellite System (JPSS) program, the NOAA/STAR Ocean Color Team has been making in situ measurements continuously in support of calibration/validation (Cal/Val) and algorithm development activities. Supported by NOAA Office of Marine and Air Operations (OMAO), VIIRS Ocean Color Cal/Val team has successfully conducted three dedicated VIIRS Ocean Color Cal/Val cruises (with NOAA *Nancy Forster*) in November 2014 (*Ondrusek et al.*, 2015), December 2015 (*Ondrusek et al.*, 2016), and October 2016, respectively. VIIRS ocean color Cal/Val team from various organizations (various agencies and Universities, as well as

international partners) has successfully participated these cruises. The in situ data collected in the cruises have been used to evaluate and validate ocean color products derived from VIIRS-SNPP. NOAA/STAR scientists look forward to continuing these dedicated ocean color Cal/Val campaigns on NOAA vessels annually. Some detailed VIIRS dedicated Cal/Val cruise measurements can be found in the two NOAA reports (*Ondrusek, et al.*, 2016; *Ondrusek, et al.*, 2015), and the third cruise report will also be published soon.

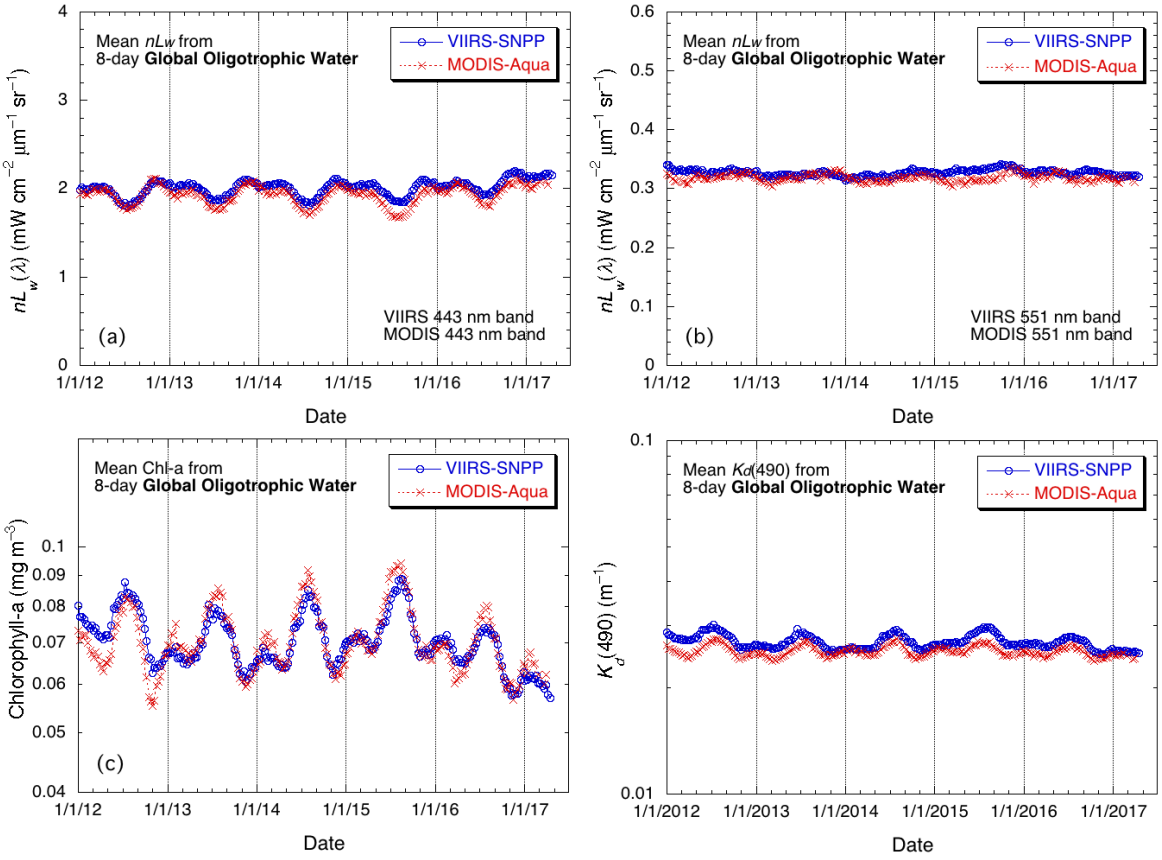

Figure 15. Time series of VIIRS ocean color products (blue) compared with those from MODIS-Aqua (red) over global oligotrophic waters with 8-day mean values for ocean color products of (a) $nL_w(443)$, (b) $nL_w(551)$, (c) Chl-a, and (d) $K_d(490)$. Note that MODIS-Aqua data were directly downloaded from the NASA OBPG website.

In addition to the dedicated VIIRS Ocean Color Cal/Val cruises, NOAA/STAR scientists have also been participating various ship opportunities to collect in situ data over various ocean and coastal regions. Furthermore, VIIRS Ocean Color Cal/Val team members (PIs) have been collecting in situ data in support of VIIRS ocean color validation. We have been also working with international partners to obtain useful in situ data. All in situ data collected from various sources will be used to evaluate and validate VIIRS ocean color products. For some extensive

VIIRS ocean color product evaluation and validation, please visit the NOAA/STAR OC Cal/Val webpage online at: https://www.star.nesdis.noaa.gov/sod/mecb/color/CalVal.php.

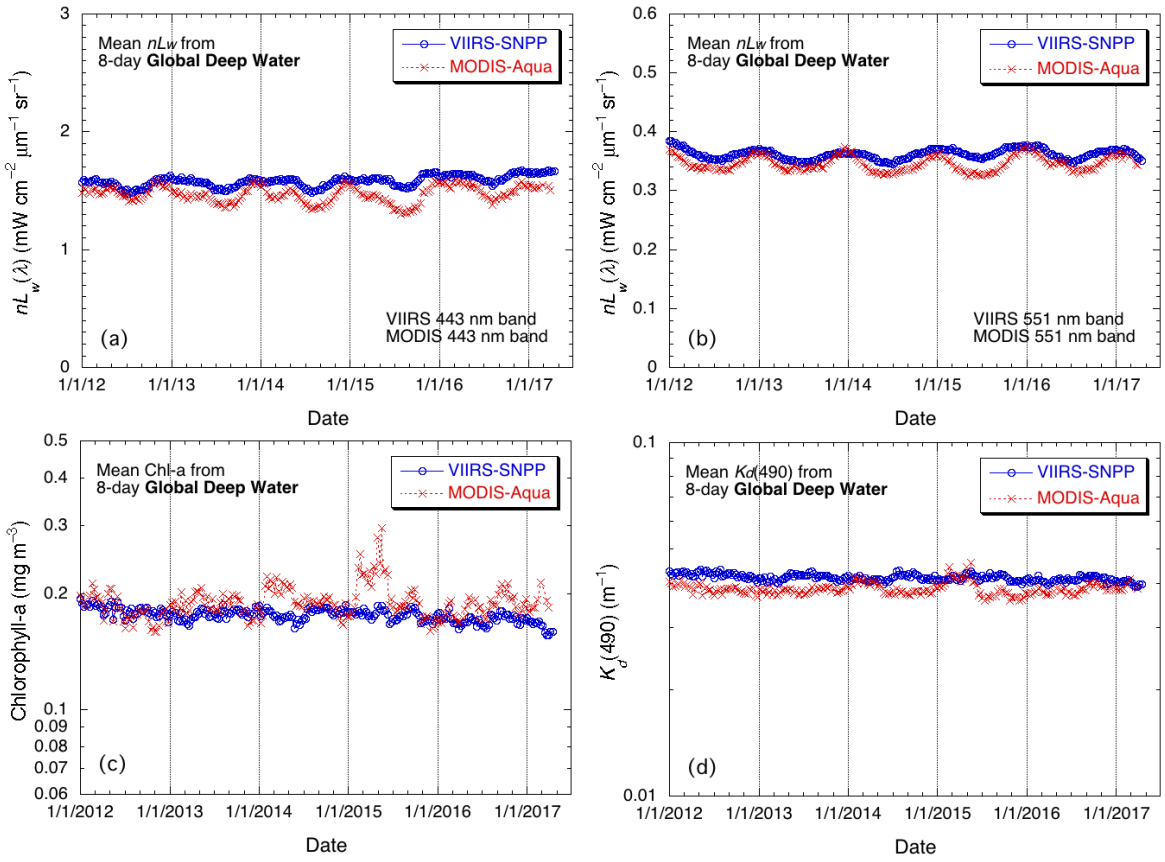

Figure 16. Time series of VIIRS ocean color products (blue) compared with those from MODIS-Aqua (red) over global deep oceans (depth > 1 km) with 8-day mean values for ocean color products of (a) $nL_w(443)$, (b) $nL_w(551)$, (c) Chl-a, and (d) $K_d(490)$. Note that MODIS-Aqua data were directly downloaded from the NASA OBPG website.

2.7.10. VIIRS and MODIS global Level-3 data comparisons

For effective evaluations of VIIRS ocean color data quality, global VIIRS ocean color Level-3 data products are necessary for overall ocean color product evaluations. The VIIRS Level-3 data processing algorithm is essentially the same as the one used for producing SeaWiFS and MODIS global Level-3 ocean color products (*Campbell et al.*, 1995). Specifically, in the VIIRS Level-3 data processing, pixels containing valid Level-2 data are mapped to a fixed spatial grid with resolution of 9 km. The grid elements or bins are arranged in rows beginning at the South Pole. Each row begins at 180° longitude and circumscribes the Earth at a given latitude. It is noted that in here the MODIS-Aqua Level-3 data were directly downloaded from the NASA OBPG website (oceancolor.gsfc.nasa.gov).

Figure 15 shows the time series of VIIRS ocean color products (blue) compared with those from MODIS-Aqua (red) over global oligotrophic waters using the 8-day global 9-km Level-3 file from 2012 to 2016. Figures 15(a)–15(d) are VIIRS-MODIS comparisons for ocean color products of $nL_w(443)$, $nL_w(551)$, Chl-a, and $K_d(490)$, respectively, over global oligotrophic waters. It is particularly noted that VIIRS-SNPP and MODIS-Aqua have very close spectral bands for 443 nm and 551 nm, and thus both $nL_w(443)$ and $nL_w(551)$ should be comparable for VIIRS and MODIS. In general, VIIRS ocean color products are in good agreement with those of MODIS in the global oligotrophic waters. For $nL_w(443)$, VIIRS and MODIS have produced quite consistent and stable data up to about mid-2016. However, there is slightly upward trending in $nL_w(443)$ from mid-2016 over oligotrophic waters (Fig. 15(a)). $nL_w(551)$ times series are very flat for both VIIRS and MODIS. Chl-a and $K_d(490)$ time series are consistent in seasonal variations, and are very stable from 2012 to 2015 for both VIIRS and MODIS, but they both drop significantly in 2016 (corresponding to the upward trending in $nL_w(443)$), for which the cause needs to be further investigated.

Similarly, Fig. 16 shows the time series of VIIRS (blue) and MODIS (red) ocean color products comparisons over global deep waters (ocean regions with depth > 1 km) using the 8-day Level-3 file from 2012 to 2016. Again, Figs. 16(a)–16(d) are VIIRS-MODIS comparisons for ocean color products of $nL_w(443)$, $nL_w(551)$, Chl-a, and $K_d(490)$, respectively, over global deep waters. Results in Fig. 16 show that ocean color products from MODS and VIIRS are generally consistent and compared well. However, there are some differences. MODIS-Aqua-derived Chl-a and $K_d(490)$ times series show some significant anomalies in the early 2015, while VIIRS-measured Chl-a and $K_d(490)$ data are quite stable and consistent in that time period. Some slight difference in $nL_w(443)$ between VIIRS and MODIS (VIIRS very slightly higher) over global deep waters can be seen, with also slightly upward trending from mid-2016 (Fig. 16(a)). For $nL_w(551)$, VIIRS and MODIS are very close to each other, and show same seasonal variations. Overall, VIIRS global ocean color products are consistent with those from MODIS-Aqua.

3. ASSUMPTIONS AND LIMITATIONS

3.1. Assumptions

There are mainly two assumptions in the MSL12 ocean color data processing:

1. In the proposed NIR-, SWIR-, and NIR-SWIR-based atmospheric correction algorithms for ocean color data processing, the black ocean (i.e., no water-leaving radiance contribution) is assumed in the NIR and SWIR bands. Specifically, for open oceans, the black ocean at the NIR bands is assumed for the NIR-based atmospheric correction, while over coastal and inland waters the NIR ocean reflectance correction is applied (assuming non-black ocean at the NIR bands). For the SWIR-based atmospheric correction, the black ocean at the SWIR bands is assumed for both open oceans and turbid coastal and inland waters.
2. Non- or weakly absorbing aerosols are assumed in the atmosphere correction algorithms (NIR-, SWIR-, and NIR-SWIR-based) and ocean color data processing.

3.2. Limitations

3.2.1. Noise issue for the VIIRS SWIR bands

The matchup analysis demonstrates that using the MODIS (or VIIRS) SWIR bands for ocean color data processing has reduced the bias errors in $nL_w(\lambda)$. However, the noise errors are increased (*Wang and Shi*, 2012; *Wang, et al.*, 2009b; *Werdell, et al.*, 2010), possibly leading to some negative $nL_w(\lambda)$ cases for which true $nL_w(\lambda)$ values are very low. Comparing to the results from the NIR method, however, the SWIR method improves the MODIS-derived $nL_w(\lambda)$ products in the coastal and inland water regions, where true $nL_w(\lambda)$ values at the blue (412 and 443 nm) are often quite low. In these cases, we found that using the SWIR method the MODIS $nL_w(\lambda)$ values at the blue are elevated (*Wang and Shi*, 2007; *Wang, et al.*, 2007) and cases with the negative $nL_w(\lambda)$ are indeed reduced significantly. Therefore, in the coastal and inland water regions, the SWIR method is usually superior to the NIR method, particularly over highly turbid waters. It is important to note that, for both the SWIR and NIR-SWIR algorithms, bias errors in $nL_w(\lambda)$ from the matchup analysis are reduced, indicating improved algorithm performance also related to the improved aerosol LUTs with the vicarious calibration.

The data product noise errors from the SWIR-based method are mainly from two sources: (1) considerably lower SNR values for the MODIS (or VIIRS) SWIR bands that are used for the data processing (atmospheric correction) (*Wang and Shi*, 2012) and (2) a little more uncertainty introduced by using the SWIR bands (1240 and 2130 nm) for atmospheric correction (*Wang and Shi*, 2012), particularly for short visible bands. *Wang* (2007) shows that atmospheric correction using the SWIR bands at 1240 and 2130 nm for deriving $nL_w(\lambda)$ often produces a little larger uncertainty than results from using the NIR bands (748 and 869 nm). This is particularly true for cases of the maritime aerosols, which are often dominated in the open oceans. In addition, with the current VIIRS or MODIS SNR characteristics for the SWIR bands, there may be significant noise error in the derived $nL_w(\lambda)$ using the SWIR algorithm (*Wang*, 2007). Therefore, it is proposed that VIIRS ocean color products be processed using the NIR-SWIR combined method for which the non-turbid and turbid ocean waters are processed using the standard-NIR and SWIR method, respectively.

For turbid coastal and inland waters, the use of the VIIRS SWIR algorithm versus the standard-NIR algorithm with the NIR ocean contribution correction is somewhat a tradeoff between using a noised measurement with little or no bias versus a high quality radiance measurement with a correction algorithm that is in error. However, it is generally desired to use the satellite-measured data instead of modeling for the NIR ocean contribution correction because of model limitations, particularly over highly turbid waters. Thus, the SWIR algorithm is preferred for deriving water properties in turbid coastal and inland waters.

3.2.2. Issues with extremely turbid waters

In extremely turbid waters, such as along the China east coast region with high concentration of suspended sediment, the value of $nL_w(862)$ can sometimes reach beyond ~3 mW cm^{-2} μm^{-1} sr^{-1} (*Jiang and Wang*, 2014; *Shi and Wang*, 2014). In such cases, the NIR-based algorithms (with the NIR ocean reflectance correction) do not work anymore (*Shi and Wang*,

2014). In fact, *Shi and Wang* (2014) shows that estimation of the NIR ocean reflectance contribution can only work for cases with $nL_w(862) < \sim 1.5$ mW cm^{-2} μm^{-1} sr^{-1}. Thus, the SWIR atmospheric correction algorithm for satellite ocean color data processing is indispensable to derive accurate $nL_w(\lambda)$ for highly turbid coastal and inland waters (*Shi and Wang*, 2014).

3.2.3. Issues with strongly absorbing aerosols

The NIR-, SWIR-, and NIR-SWIR-based ocean color data processing in MSL12 also assumes that aerosols are non- and weakly absorbing. For strongly absorbing aerosols, e.g., dust, smoke, results from the current atmospheric correction algorithm are poor. An essential problem for the strongly absorbing aerosol correction in deriving accurate ocean color products is principally due to aerosol particle absorbing characteristics at the visible bands. Some studies for the effects of the absorbing aerosols on the atmospheric correction for ocean color products have been conducted (*Chomko and Gordon*, 1998; *Chomko et al.*, 2003; *Gordon*, 1997; *Gordon et al.*, 1997). It is now well known that for the strongly absorbing aerosols the sensor-measured TOA radiances depend strongly on aerosol layer vertical profile (*IOCCG*, 2010). Thus, for accurate atmospheric correction for the absorbing aerosols, one will require information of the aerosol layer vertical location (*IOCCG*, 2010). It is generally difficult to obtain accurate aerosol vertical distribution profile from passive radiance measurements, in particular, for a thin aerosol layer. In addition, realistic absorbing aerosol models (e.g., dust model) that are representative regionally are required. These absorbing aerosol models are needed for generating the aerosol LUTs that are used for atmospheric correction. The current NIR-, SWIR-, and NIR-SWIR-based atmospheric correction algorithms have not yet included absorbing aerosol models (LUTs) for dealing with strongly absorbing aerosol cases. In addition, aerosol vertical distribution information for strongly absorbing aerosols is not available. However, absorbing aerosol cases can be identified using VIIRS measurements at the short visible, NIR, and SWIR bands (*Shi and Wang*, 2007), and can be used for data quality assurance purpose.

4. Acknowledgements

The VIIRS ocean color work has been supported by the Joint Polar Satellite System (JPSS) funding. We thank all members of the NOAA Ocean Color Team for their contributions for routinely producing VIIRS ocean color products. We would like also to acknowledge supports in all these year from the NOAA Ocean Color Coordinating Group (NOCCG), which includes representatives from various NOAA line offices (users, scientists, modelers, managers, etc.). We are grateful to the MOBY team and AERONET-OC PIs (particularly for the sites in CSI, LISCO, and USC) for providing in situ optics data in support of VIIRS ocean color Cal/Val effort. We thank VIIRS Cal/Val team (PIs and their associates) in support of VIIRS ocean color Cal/Val activities. We are grateful to the all scientists who have contributed in situ data to NASA SeaBASS database. The views, opinions, and findings contained in this document are those of the authors and should not be construed as an official NOAA or U.S. Government position, policy, or decision.

5. LIST OF REFERENCES

Ahmad, Z., Franz, B. A., McClain, C. R., Kwiatkowska, E. J., Werdell, J., Shettle, E. P., and Holben, B. N. (2010), New aerosol models for the retrieval of aerosol optical thickness and normalized water-leaving radiances from the SeaWiFS and MODIS sensors over coastal regions and open oceans, *Appl. Opt.*, *49*, 5545–5560.

Antoine, D. and Morel, A. (1999), A multiple scattering algorithm for atmospheric correction of remotely sensed ocean colour (MERIS instrument): principle and implementation for atmospheres carrying various aerosols including absorbing ones, *Int. J. Remote Sens.*, *20*, 1875–1916.

Bailey, S. W. Franz, B. A., and Werdell, P. J. (2010), Estimation of near-infrared water-leaving reflectance for satellite ocean color data processing, *Optics Express*, *18*, 7521–7527.

Behrenfeld, M. J., O'Malley, R. T., Siegel, D. A., McClain, C. R., Sarmiento, J. L., Feldman, G. C., Milligan, A. J., Falkowski, P. G., Letelier, R. M., and Boss, E. S. (2006), Climate-driven trends in contemporary ocean productivity, *Nature*, *444*, 752–755.

Behrenfeld, M. J., Randerson, J. T., McClain, C. R., Feldman, G. C., Los, S. O., Tucker, C. J., Falkowski, P. G., Field, C. B., Frouin, R., Esaias, W. E., Kolber, D. D., and Pollack, N. H. (2001), Biospheric primary production during an ENSO transition, *Science*, *291*, 2594–2597.

Bleck, R. (2002), An oceanic general circulation model framed in hybrid isopycnic-Cartesian coordinate, *Ocean Modeling*, *4*, 55–88.

Campbell, J. W., Blaisdell, J. M., and Darzi, M. (1995), Level-3 SeaWiFS Data Products: Spatial and Temporal Binning Algorithms,Vol. 32, NASA Tech. Memo. 104566, S.B. Hooker, E.R. Firestone, and J.G. Acker, Eds., NASA Goddard Space Flight Center, Greenbelt, Maryland.

Chassignet, E. P., Hurlburt, H. E., Smedstad, O. M., Halliwell, G. R., Hogan, P. J., Wallcraft, A. J., Baraille, R., and Bleck, R. (2007), The HYCOM (Hybrid Coordinate Ocean Model) data assimilative system, *J. Marine Systems*, *65*, 60–83.

Chassignet, E. P., Smith, L., Halliwell, G. R., and Bleck, R. (2003), North Atlantic simulations with the Hybrid Coordinate Ocean Model (HYCOM): Impact of coordinate choice, reference pressure, and thermobaricity, *J. Phys. Oceanogr.*, *33*, 2504–2526.

Chavez, F. P., Strutton, P. G., Friederich, G. E., Feely, R. A., Feldman, G. C., Foley, D. G., and McPhaden, M. J. (1999), Biological and Chemical Response of the Equatorial Pacific Ocean to the 1997-98 El Niño, *Science*, *286*, 2126–2131.

Chomko, R. and Gordon, H. R. (1998), Atmospheric correction of ocean color imagery: use of the Junge power-law aerosol size distribution with variable refractive index to handle aerosol absorption, *Appl. Opt.*, *37*, 5560–5572.

Chomko, R. M., Gordon, H. R., Maritorena, S., and Siegel, D. A. (2003), Simultaneous retrieval of oceanic and atmospheric parameters for ocean color imagery by spectral optimization: a validation, *Remote Sens. Environ.*, *84*, 208–220.

Clark, D. K., Gordon, H. R., Voss, K. J., Ge, Y., Broenkow, W., and Trees, C. (1997), Validation of atmospheric correction over the ocean, *J. Geophys. Res.*, *102*, 17209–17217.

Cox, C. and Munk, W. (1954), Measurements of the roughness of the sea surface from photographs of the sun's glitter, *Jour. Opt. Soc. of Am.*, *44*, 838–850.

Deschamps, P. Y., Herman, M., and Tanre, D. (1983), Modeling of the atmospheric effects and its application to the remote sensing of ocean color, *Appl. Opt.*, *22*, 3751–3758.

Dierssen, H. M. (2010), Perspectives on empirical approaches for ocean color remote sensing of chlorophyll in a changing climate, *Proc. Natl. Acad. Sci. U.S.A.*, *107*, 17073–17078, doi:10.1073/pnas.0913800107.

Eplee Jr., R. E., Robinson, W. D., Bailey, S. W., Clark, D. K., Werdell, P. J., Wang, M., Barnes, R. A., and McClain, C. R. (2001), Calibration of SeaWiFS. II: Vicarious techniques, *Appl. Opt.*, *40*, 6701–6718.

Esaias, W. E., Abbott, M. R., Barton, I., Brown, O. B., Campbell, J. W., Carder, K. L., Clark, D. K., Evans, R. L., Hodge, F. E., Gordon, H. R., Balch, W. P., Letelier, R., and Minnet, P. J. (1998), An overview of MODIS capabilities for ocean science observations, *IEEE Trans. Geosci. Remote Sens.*, *36*, 1250–1265.

Franz, B. A., Bailey, S. W., Werdell, P. J., and McClain, C. R. (2007), Sensor-independent approach to the vicarious calibration of satellite ocean color radiometry, *Appl. Opt.*, *46*, 5068–5082.

Frouin, R., Franz, B. A., and Werdell, P. J. (2003), The SeaWiFS PAR product, SeaWiFS Postlaunch Techincal Report Series,Vol. 22, NASA Tech. Memo. 2003-206892, S. B. Hooker and E. R. Firestone, Eds., p46–50, NASA Goddard Space Flight Center, Greenbelt, Maryland.

Frouin, R., McPherson, J., Ueyoshi, K., and Franz, B. A. (2012), A time series of photosynthetically available radiation at the ocean surface from SeaWiFS and MODIS data, *Proc. SPIE 8525, Remote Sensing of the Marine Environment II*, 852519 doi:10.1117/12.981264.

Frouin, R., Schwindling, M., and Deschamps, P. Y. (1996), Spectral reflectance of sea foam in the visible and near infrared: In situ measurements and remote sensing implications, *J. Geophys. Res.*, *101*, 14361–14371.

Fukushima, H., Higurashi, A., Mitomi, Y., Nakajima, T., Noguchi, T., Tanaka, T., and Toratani, M. (1998), Correction of atmospheric effects on ADEOS/OCTS ocean color data: Algorithm description and evaluation of its performance, *J. Oceanogr.*, *54*, 417–430.

Gnanadesikan, A., Emanuel, K., Vecchi, G. A., Anderson, W. G., and Hallberg, R. (2010), How ocean color can steer Pacific tropical cyclones, *Geophy. Res. Lett.*, *37*, L18802, doi: 18810.11029/12010GL044514.

Goldberg, M. D., Kilcoyne, H., Cikanek, H., and Mehta, A. (2013), Joint Polar Satellite System: The United States next generation civilian polar-orbiting environmental satellite system, *J. Geophys. Res. Atmos.*, *118*, 13463–13475, doi: 13410.11002/12013JD020389.

Gordon, H. R. (1997), Atmospheric correction of ocean color imagery in the Earth Observing System era, *J. Geophys. Res.*, *102*, 17081–17106.

Gordon, H. R. (1998), In-orbit calibration strategy for ocean color sensors, *Rem. Sens. Environ.*, *63*, 265–278.

Gordon, H. R. (2005), Normalized water-leaving radiance: revisiting the influence of surface roughness, *Appl. Opt.*, *44*, 241–248.

Gordon, H. R., Brown, J. W., and Evans, R. H. (1988a), Exact Rayleigh scattering calculations for use with the Nimbus-7 Coastal Zone Color Scanner, *Appl. Opt.*, *27*, 862–871.

Gordon, H. R., Brown, O. B., Evans, R. H., Brown, J. W., Smith, R. C., Baker, K. S., and Clark, D. K. (1988b), A semianalytic radiance model of ocean color, *J. Geophys. Res.*, *93*, 10909–10924.

Gordon, H. R., Clark, D. K., Mueller, J. L., and Hovis, W. A. (1980), Phytoplankton Pigments from the Nimbus-7 Coastal Zone Color Scanner: Comparisons with Surface Measurements, *Science*, *210*, 63–66.

Gordon, H. R., Du, T., and Zhang, T. (1997), Remote sensing of ocean color and aerosol properties: resolving the issue of aerosol absorption, *Appl. Opt.*, *36*, 8670–8684.

Gordon, H. R. and Morel, A. (1983), *Remote assessment of ocean color for interpretation of satellite visible imagery: A review*, 114 pp., Springer-Verlag, New York.

Gordon, H. R. and Wang, M. (1992), Surface roughness considerations for atmospheric correction of ocean color sensors. 1: The Rayleigh scattering component, *Appl. Opt.*, *31*, 4247–4260.

Gordon, H. R. and Wang, M. (1994a), Retrieval of water-leaving radiance and aerosol optical thickness over the oceans with SeaWiFS: A preliminary algorithm, *Appl. Opt.*, *33*, 443–452.

Gordon, H. R. and Wang, M. (1994b), Influence of oceanic whitecaps on atmospheric correction of ocean-color sensor, *Appl. Opt.*, *33*, 7754–7763.

Hale, G. M. and Querry, M. R. (1973), Optical constants of water in the 200nm to 200µm wavelength region, *Appl. Opt.*, *12*, 555–563.

Holben, B. N., Eck, T. F., Slutsker, I., Tanre, D., Buis, J. P., Setzer, A., Vermote, A., Reagan, J. A., Kaufman, Y., Nakajima, T., Lavenu, F., Jankowiak, I., and Smirnov, A. (1998), AERONET-A federated instrument network and data archive for aerosol characterization, *Remote Sens. Environ.*, *66*, 1–16.

Hooker, S. B., Esaias, W. E., Feldman, G. C., Gregg, W. W., and McClain, C. R. (1992), An Overview of SeaWiFS and Ocean Color, Vol. 1 of SeaWiFS Technical Report Series,NASA Tech. Memo. 104566, S.B. Hooker and E.R. Firestone, Eds., NASA Goddard Space Flight Center, Greenbelt, Maryland.

Hovis, W. A., Clark, D. K., Anderson, F., Austin, R. W., Wilson, W. H., Baker, E. T., Ball, D., Gordon, H. R., Mueller, J. L., Sayed, S. T. E., Strum, B., Wrigley, R. C., and Yentsch, C. S. (1980), Nimbus 7 Coastal Zone Color Scanner: system description and initial imagery, *Science*, *210*, 60–63.

Hu, C., Lee, Z., and Franz, B. A. (2012), Chlorophyll a algorithms for oligotrophic oceans: A novel approach based on three-band reflectance difference, *J. Geophys. Res.*, *117*, C01011, doi: 01010.01029/02011JC007395.

IOCCG (2004), Guide to the creation and use of ocean-colour, Level-3, binned data products, Antoine, D. (Ed.), *Reports of International Ocean-Color Coordinating Group*, No. 4, IOCCG, Dartmouth, Canada.

IOCCG (2010), Atmospheric Correction for Remotely-Sensed Ocean-Colour Products, Wang, M. (Ed.), *Reports of International Ocean-Color Coordinating Group*, No. 10, IOCCG, Dartmouth, Canada.

Jiang, L. and Wang, M. (2013), Identification of pixels with stray light and cloud shadow contaminations in the satellite ocean color data processing, *Appl. Opt.*, *52*, 6757–6770.

Jiang, L. and Wang, M. (2014), Improved near-infrared ocean reflectance correction algorithm for satellite ocean color data processing, *Opt. Express*, *22*, 21657–21678.

Kou, L., Labrie, D., and Chylek, P. (1993), Refractive indices of water and ice in the 0.65-2.5μm spectral range, *Appl. Opt.*, *32*, 3531–3540.

Kratzer, S., Hakansson, B., and Sahlin, C. (2003), Assessing secchi and photic zone depth in the Baltic Sea from satellite data, *Ambio*, *32*, 577–585.

Lavender, S. J., Pinkerton, M. H., Moore, G. F., Aiken, J., and Blondeau-Patissier, D. (2005), Modification to the atmospheric correction of SeaWiFS ocean color images over turbid waters, *Continental Shelf Research*, *25*, 539–555.

Le, C., Hu, C., Cannizzaro, J., English, D., Muller-Karger, F., and Lee, Z. (2013), Evaluation of chlorophyll-a remote sensing algorithms for an optically complex estuary, *Remote Sens. Environ.*, *129*, 75–89.

Lee, Z. P., Carder, K. L., and Arnone, R. A. (2002), Deriving inherent optical properties from water color: a multiple quasi-analytical algorithm for optically deep waters, *Appl. Opt.*, *41*, 5755–5772.

Lewis, M., Carr, M., Feldman, G., Esaias, W. E., and McClain, C. R. (1990), Influence of penetrating solar radiation on the heat budget of the equatorial Pacific ocean, *Nature*, *347*, 543–545.

Loisel, H. and Morel, A. (2001), Non-isotropy of the upward radiance field in typical coastal (Case 2) waters, *Int. J. Remote Sens.*, *22*, 275–295.

McClain, C. R. (2009), A decade of satellite ocean color observations, *Annual Review of Marine Science*, *1*, 19–42.

McClain, C. R., Feldman, G. C., and Hooker, S. B. (2004), An overview of the SeaWiFS project and strategies for producing a climate research quality global ocean bio-optical time series, *Deep Sea Res. Part II*, *51*, 5–42.

Mikelsons, K., Wang, M., Jiang, L., and Bouali, M. (2014), Destriping algorithm for improved satellite-derived ocean color product imagery, *Opt. Express*, *22*, 28058–28070.

Mobley, C. D. (1994), *Light and Water: Radiative Transfer in Natural Waters*, 592 pp., Academic, New York.

Moore, K. D., Voss, K. J., and Gordon, H. R. (2000), Spectral reflectance of whitecaps: Their contribution to water-leaving radiance, *J. of Geophys. Res.*, *105*, 6493–6499.

Morel, A. and Antoine, D. (1994), Heating rate within the upper ocean in relation to its bio-optical state, *J. Phys. Oceanogr.*, *24*, 1652–1665.

Morel, A. and Gentili, G. (1996), Diffuse reflectance of oceanic waters. III. Implication of bidirectionality for the remote-sensing problem, *Appl. Opt.*, *35*, 4850–4862.

Morel, A., Huot, Y., Gentili, B., Werdell, P. J., Hooker, S. B., and Franz, B. A. (2007), Examining the consistency of products derived from various ocean color sensors in open ocean (Case 1) waters in the perspective of a multi-sensor approach, *Remote Sens. Environ.*, *111*, 69–88.

Mueller, J. L. (2000), SeaWiFS algorithm for the diffuse attenuation coefficient, K(490), using water-leaving radiances at 490 and 555 nm, SeaWiFS Postlaunch Technical Report Series,Vol. 11, NASA Tech. Memo. 2000-206892, S. B. Hooker and E. R. Firestone, Eds., p24–27, NASA Goddard Space Flight Center, Greenbelt, Maryland.

O'Reilly, J. E., Maritorena, S., Mitchell, B. G., Siegel, D. A., Carder, K. L., Garver, S. A., Kahru, M., and McClain, C. R. (1998), Ocean color chlorophyll algorithms for SeaWiFS, *J. Geophys. Res.*, *103*, 24937–24953.

O'Reilly, J. E., Maritorena, S., Siegel, D. A., O'Brien, M. C., Toole, D., Mitchell, B. G., Kahru, M., Chavez, F. P., Strutton, P., Cota, G. F., Hooker, S. B., McClain, C. R., Carder, K. L., Muller-Karger, F., Harding, L., Magnuson, A., Phinney, D., Moore, G. F., Aiken, J., Arrigo, K. R., Letelier, R., and Culver, M. (2000), Ocean Colr Chlorophyll a Algorithms for SeaWiFS, OC2 and OC4: Version 4, SeaWiFS Postlaunch Technical Report Series,NASA Tech. Memo. 2000-206892, p8-22, S.B. Hooker and E.R. Firestone, Eds., NASA Goddard Space Flight Center, Greenbelt, Maryland.

Ondrusek, M., Lance, V. P., Stengel, E., Wang, M., Arnone, R., Ladner, S., Goode, W., Vandermeulen, R., Freeman, S., Chaves, J. E., Mannino, A., Gilerson, A., Ahmed, S., Carrizo, C., El-Habashi, A., Foster, R., Ottaviani, M., Goes, J. I., Gomes, H., McKee, K., Hu, C., Kovach, C., English, D., Cannizzaro, J., Johnson, B. C., Lee, Z. P., Wei, J., Wang, Q., Lin, J., Tufillaro, N., Nahorniak, J., Davis, C. O., and Voss, K. J. (2016), Report for Dedicated JPSS VIIRS Ocean Color Calibration/Validation Cruise December 2015, NOAA Technical Report NESDIS 148, V. P. Lance (ed.), NOAA National Environmental Satellite, Data, and Information Service, Silver Spring, Maryland, doi:10.7289/TR-NESDIS-148.

Ondrusek, M., Stengel, E., Lance, V. P., Wang, M., Voss, K. J., Zibordi, G., Talone, M., Lee, Z. P., Wei, J., Lin, J., Hu, C., English, D., Kovach, C., Cannizzaro, J., Gilerson, A., Ahmed, S., Ibrahim, A., El-Habashi, A., Foster, R., Arnone, R., Vandermeulen, R., Ladner, S., Goode, W., Goes, J. I., Gomes, H., Chekalyuk, A., McKee, K., Freeman, S., Neeley, A., and Johnson, B. C. (2015), Report for Dedicated JPSS VIIRS Ocean Color Calibration/ Validation Cruise, NOAA Technical Report NESDIS 146, V. P. Lance (ed.), NOAA National Environmental Satellite, Data, and Information Service, Silver Spring, Maryland, doi:10.7289/V52B8W0.

Pierson, D. C., Kratzer, S., Strömbeck, N., and Håkansson, B. (2008), Relationship between the attenuation of downwelling irradiance at 490 nm with the attenuation of PAR (400 nm-700 nm) in the Baltic Sea, *Remote Sens. Environ.*, *112*, 668–680.

Platt, T., Sathyendranath, S., Caverhill, C., and Lewis, M. (1988), Ocean primary production and available light: Further algorithms for remote sensing, *Deep-Sea Research Part I*, *35*, 855–879.

Ramachandran, S., and Wang, M. (2011), Near-real-time ocean color data processing using ancillary data from the Global Forecast System model, *IEEE Trans. Geosci. Remote Sens.*, *49*, 1485–1495.

Rast, M., Bezy, J. L., and Bruzzi, S. (1999), The ESA Medium Resolution Imaging Spectrometer MERIS a review of the instrument and its mission, *Int. J. Remote Sens.*, *20*, 1681–1702.

Rochford, P. A., Kara, A. B., Wallcraft, A. J., and Arnone, R. A. (2001), Importance of solar subsurface heating in ocean general circulation models, *J. Geophys. Res.*, *106*, 30923–30938.

Ruddick, K. G., Ovidio, F., and Rijkeboer, M. (2000), Atmospheric correction of SeaWiFS imagery for turbid coastal and inland waters, *Appl. Opt.*, *39*, 897–912.

Salomonson, V. V., Barnes, W. L., Maymon, P. W., Montgomery, H. E., and Ostrow, H. (1989), MODIS: advanced facility instrument for studies of the Earth as a system, *IEEE Trans. Geosci. Remote Sensing*, *27*, 145–153.

Sathyendranath, S., Gouveia, A. D., Shetye, S., Ravindran, P., and Platt, T. (1991), Biological control of surface temperature in the Arabian Sea, *Nature*, *349*, 54–56.

Sathyendranath, S., Platt, T., Caverhill, C. M., Warnock, R., and Lewis, M. (1989), Remote sensing of oceanic primary production: Computations using a spectral model, *Deep-Sea Research*, *36*, 431–453.

Shettle, E. P. and Fenn, R. W. (1979), Models for the Aerosols of the Lower Atmosphere and the Effects of Humidity Variations on Their Optical Properties,AFGL-TR-79-0214, p1–94, U.S. Air Force Geophysics Laboratory, Hanscom Air Force Base, Mass.

Shi, W. and Wang, M. (2007), Detection of turbid waters and absorbing aerosols for the MODIS ocean color data processing, *Remote Sens. Environ.*, *110*, 149–161.

Shi, W. and Wang, M. (2009), An assessment of the black ocean pixel assumption for MODIS SWIR bands, *Remote Sens. Environ.*, *113*, 1587–1597.

Shi, W. and Wang, M. (2014), Ocean reflectance spectra at the red, near-infrared, and shortwave infrared from highly turbid waters: A study in the Bohai Sea, Yellow Sea, and East China Sea, *Limnol. Oceanogr.*, *59*, 427–444.

Siegel, D. A., Doney, S. C., and Yoder, J. A. (2002), The North Atlantic spring phytoplankton bloom and sverdrup's critical depth hypothesis, *Science*, *296*, 730–733.

Siegel, D. A., Wang, M., Maritorena, S., and Robinson, W. (2000), Atmospheric correction of satellite ocean color imagery: the black pixel assumption, *Appl. Opt.*, *39*, 3582–3591.

Son, S. and Wang, M. (2015), Diffuse attenuation coefficient of the photosynthetically available radiation Kd(PAR) for global open ocean and coastal waters, *Remote Sens. Environ.*, *159*, 250–258.

Stumpf, R. P., Arnone, R. A., Gould, R. W., Martinolich, P. M., and Ransibrahmanakul, V. (2003), A partially coupled ocean-atmosphere model for retrieval of water-leaving radiance from SeaWiFS in coastal waters, SeaWiFS Postlaunch Technical Report Series,Vol. 22, NASA Tech. Memo. 2003-206892, S. B. Hooker and E. R. Firestone, Eds., p51–59, NASA Goddard Space Flight Center, Greenbelt, Maryland.

Sun, J. and Wang, M. (2014), Visible Infrared Imaging Radiometer Suite solar diffuser calibration and its challenges using solar diffuser stability monitor, *Appl. Opt.*, *53*, 8571–8584.

Sun, J. and Wang, M. (2015a), On-orbit characterization of the VIIRS solar diffuser and solar diffuser screen, *Appl. Opt.*, *54*, 236–252.

Sun, J. and Wang, M. (2015b), On-orbit calibration of Visible Infrared Imaging Radiometer Suite reflective solar bands and its challengers using a solar diffuser, *Appl. Opt.*, *54*, 7210–7223.

Sun, J. and Wang, M. (2015c), Radiometric calibration of the VIIRS reflective solar bands with robust characterizations and hybrid calibration coefficients, *Appl. Opt.*, *54*, 9331–9342.

Sun, J. and Wang, M. (2016), VIIRS reflective solar bands calibration progress and its impact on ocean color products, *Remote Sens.*, *8*, 194, doi:10.3390/rs8030194.

Sun, J., Wang, M., Tan, L., and Jiang, L. (2014), An efficient approach for VIIRS RDR to SDR data processing, *IEEE Geosci. Remote Sens. Lett.*, *11*, 2037–2041.

Thuillier, G., Herse, M., Labs, D., Foujols, T., Peetermans, W., Gillotay, D., Simon, P. C., and Mandel, H. (2003), The solar spectral irradiance from 200 to 2400 nm as measured by the SOLSPEC spectrometer from the ATLAS and EURECA missions, *Solar Physics*, *214*, 1–22.

Wang, M. (1991), Atmospheric correction of the second generation ocean color sensors, Ph.D. dissertation thesis, 135 pp, University of Miami, Coral Gables, Fla.

Wang, M. (1999a), A sensitivity study of SeaWiFS atmospheric correction algorithm: Effects of spectral band variations, *Remote Sens. Environ.*, *67*, 348–359.

Wang, M. (1999b), Atmospheric correction of ocean color sensors: Computing atmospheric diffuse transmittance, *Appl. Opt.*, *38*, 451–455.

Wang, M. (2002), The Rayleigh lookup tables for the SeaWiFS data processing: Accounting for the effects of ocean surface roughness, *Int. J. Remote Sens.*, *23*, 2693–2702.

Wang, M. (2004), Extrapolation of the aerosol reflectance from the near-infrared to the visible: the single-scattering epsilon vs multiple-scattering epsilon method, *Int. J. Remote Sens.*, *25*, 3637–3650.

Wang, M. (2005), A refinement for the Rayleigh radiance computation with variation of the atmospheric pressure, *Int. J. Remote Sens.*, *26*, 5651–5663.

Wang, M. (2006a), Effects of ocean surface reflectance variation with solar elevation on normalized water-leaving radiance, *Appl. Opt.*, *45*, 4122–4128.

Wang, M. (2006b), Aerosol polarization effects on atmospheric correction and aerosol retrievals in ocean color remote sensing, *Appl. Opt.*, *45*, 8951–8963.

Wang, M. (2007), Remote sensing of the ocean contributions from ultraviolet to near-infrared using the shortwave infrared bands: simulations, *Appl. Opt.*, *46*, 1535–1547.

Wang, M. (2016), Rayleigh radiance computations for satellite remote sensing: Accounting for the effect of sensor spectral response function, *Opt. Express*, *24*, 12414–12429.

Wang, M., Ahn, J. H., Jiang, L., Shi, W., Son, S., Park, Y. J., and Ryu, J. H. (2013a), Ocean color products from the Korean Geostationary Ocean Color Imager (GOCI), *Opt. Express*, *21*, 3835–3849.

Wang, M. and Bailey, S. (2001), Correction of the sun glint contamination on the SeaWiFS ocean and atmosphere products, *Appl. Opt.*, *40*, 4790–4798.

Wang, M. and Franz, B. A. (2000), Comparing the ocean color measurements between MOS and SeaWiFS: A vicarious intercalibration approach for MOS, *IEEE Trans. Geosci. Remote Sens.*, *38*, 184–197.

Wang, M., Franz, B. A., Barnes, R. A., and McClain, C. R. (2001), Effects of spectral bandpass on SeaWiFS-retrieved near-surface optical properties of the ocean, *Appl. Opt.*, *40*, 342–348.

Wang, M. and Gordon, H. R. (1994), A simple, moderately accurate, atmospheric correction algorithm for SeaWiFS, *Remote Sens. Environ.*, *50*, 231–239.

Wang, M. and Gordon, H. R. (2002), Calibration of ocean color scanners: How much error is acceptable in the near-infrared, *Remote Sens. Environ.*, *82*, 497–504.

Wang, M., Isaacman, A., Franz, B. A., and McClain, C. R. (2002), Ocean color optical property data derived from the Japanese Ocean Color and Temperature Scanner and the French Polarization and Directionality of the Earth's Reflectances: A comparison study, *Appl. Opt.*, *41*, 974–990.

Wang, M., Jiang, L., Liu, X., Son, S., Sun, J., Shi, W., Tan, L., Mikelsons, K., Wang, X., and Lance, V. (2016a), VIIRS ocean color products: A progress update, *Proc. the IEEE Int. Geosci. Remote Sens. Symposium (IGARSS)*, 5848–5851, Beijing, China, July, 5810–5815, doi:10.1109/IGARSS.2016.7730528.

Wang, M., Knobelspiesse, K. D., and McClain, C. R. (2005), Study of the Sea-Viewing Wide Field-of-View Sensor (SeaWiFS) aerosol optical property data over ocean in combination with the ocean color products, *J. Geophys. Res.*, *110*, D10S06, doi:10.1029/2004JD004950.

Wang, M. and Liu, X. (2012), MODIS Ocean Color Products Using the SWIR Method, MODIS-SWIR Algorithm Theoretical Basis Document (ATBD), 40 pp., NOAA Product System Development and Implementation (PSDI).

Wang, M., Liu, X., Jiang, L., Son, S., Sun, J., Shi, W., Tan, L., Naik, P., Mikelsons, K., Wang, X., and Lance, V. (2014), Evaluation of VIIRS ocean color products, *Proc. SPIE 9261, Ocean Remote Sensing and Monitoring from Space*, *92610E*, doi:10.1117/1112.2069251.

Wang, M., Liu, X., Jiang, L., Son, S., Sun, J., Shi, W., Tan, L., Naik, P., Mikelsons, K., Wang, X., and Lance, V. (2015a), VIIRS ocean color research and applications, *Proc. the IEEE Int. Geosci. Remote Sens. Symposium (IGARSS)*, 2911–2914, Milan, Italy, July, 2926–2931, doi:10.1109/IGARSS.2015.7326424.

Wang, M., Liu, X., Tan, L., Jiang, L., Son, S., Shi, W., Rausch, K., and Voss, K. (2013b), Impact of VIIRS SDR performance on ocean color products, *J. Geophys. Res. Atmos.*, *118*, 10347–10360, doi:10.1002/jgrd.50793.

Wang, M., Naik, P., and Son, S. (2016b), Out-of-band effects of satellite ocean color sensors, *Appl. Opt.*, *55*, 2312–2323.

Wang, M. and Shi, W. (2005), Estimation of ocean contribution at the MODIS near-infrared wavelengths along the east coast of the U.S.: Two case studies, *Geophys. Res. Lett.*, *32*, L13606, doi:10.1029/2005GL022917.

Wang, M. and Shi, W. (2006), Cloud masking for ocean color data processing in the coastal regions, *IEEE Trans. Geosci. Remote Sens.*, *44*, 3196–3205.

Wang, M. and Shi, W. (2007), The NIR-SWIR combined atmospheric correction approach for MODIS ocean color data processing, *Opt. Express*, *15*, 15722–15733.

Wang, M. and Shi, W. (2012), Sensor noise effects of the SWIR bands on MODIS-derived ocean color products, *IEEE Trans. Geosci. Remote Sens.*, *50*, 3280–3292.

Wang, M., Shi, W., and Jiang, L. (2012), Atmospheric correction using near-infrared bands for satellite ocean color data processing in the turbid western Pacific region, *Opt. Express*, *20*, 741–753.

Wang, M., Shi, W., Jiang, L., Liu, X., Son, S., and Voss, K. (2015b), Technique for monitoring performance of VIIRS reflective solar bands for ocean color data processing, *Opt. Express*, *23*, 14446–14460.

Wang, M., Shi, W., Jiang, L., and Voss, K. (2016c), NIR- and SWIR-based on-orbit vicarious calibrations for satellite ocean color sensors, *Opt. Express*, *24*, 20437–20453.

Wang, M. and Son, S. (2016), VIIRS-derived chlorophyll-a using the ocean color index method, *Remote Sens. Environ.*, *182*, 141–149.

Wang, M., Son, S., and L. W. Harding, J. (2009a), Retrieval of diffuse attenuation coefficient in the Chesapeake Bay and turbid ocean regions for satellite ocean color applications, *J. Geophys. Res.*, *114*, C10011, doi:10.1029/2009JC005286.

Wang, M., Son, S., and Shi, W. (2009b), Evaluation of MODIS SWIR and NIR-SWIR atmospheric correction algorithm using SeaBASS data, *Remote Sens. Environ.*, *113*, 635–644.

Wang, M., Tang, J., and Shi, W. (2007), MODIS-derived ocean color products along the China east coastal region, *Geophy. Res. Lett.*, *34*, L06611, doi:10.1029/2006GL028599.

Werdell, P. J. and Bailey, S. W. (2005), An improved in-situ bio-optical data set for ocean color algorithm development and satellite data product validation, *Remote Sens. Environ.*, *98*, 122–140.

Werdell, P. J., Franz, B. A., and Bailey, S. W. (2010), Evaluation of shortwave infrared atmospheric correction for ocean color remote sensing of Chesapeake Bay, *Remote Sens. Environ.*, *114*, 2238–2247.

Wu, Y., Tang, C., Sathyendranath, S., and Platt, T. (2007), The impact of bio-optical heating on the properties of the upper ocean: A sensitivity study using a 3-D circulation model for the Labrador Sea, *Deep-Sea Research Part II*, *54*, 2630–2642.

Yang, H. and Gordon, H. R. (1997), Remote sensing of ocean color: assessment of water-leaving radiance bidirectional effects on atmospheric diffuse transmittance, *Appl. Opt.*, *36*, 7887–7897.

Zhang, H. and Wang, M. (2010), Evaluation of sun glint models using MODIS measurements, *J. Quant. Spectrosc. Radiat. Transf.*, *111*, 492–506.

Zibordi, G., Holben, B. N., Slutsker, I., Giles, D., D'Alimonte, D., Melin, F., Berthon, J.-F., Vandemark, D., Feng, H., Schuster, G., Fabbri, B. E., Kaitala, S., and Seppala, J. (2009), AERONET-OC: a network for the validation of ocean color primary radiometric products, *J. Atmos. Ocean Technol.*, *26*, 1634–1651.

END OF DOCUMENT